Doctoral Dissertation (Censored)
博士論文（要約）

Transport dynamics in the spin-resolved quantum Hall edge states
（スピン分離した量子ホールエッジ状態における輸送ダイナミクス）

A Dissertation Submitted for the Degree of Doctor of Philosophy
December 2021
令和３年１２月博士（理学）申請

Department of Physics, Graduate School of Science,
The University of Tokyo
東京大学大学院理学系研究科
物理学専攻

Takase Shimizu
清水　貴勢

Abstract

In this thesis, we investigate the transport dynamics in the spin-resolved quantum Hall edge states, which form spin-resolved one-dimensional conduction channels at the edges of the two-dimensional electron system in the integer quantum Hall state [Quantum Hall edge channels (QHECs)]. In the spin-resolved QHECs, the spin and orbital degrees of freedom of electrons are strongly coupled. In other words, there is a one-by-one correspondence between the spin and orbital degree of electrons in spin-resolved QHECs. The primary interest of our studies here is whether it is possible to make quantum operations on one degree of freedom through manipulations of the other in such a strongly coupled system. More specifically, our question is what sort of quantum operations on electron spins are possible via the control of electron orbitals in the spin-resolved QHECs.

When we take the quantization axis of the spins along the magnetization axis, the zenith angle is determined by the partition rate of the spin-resolved QHECs, while the azimuth angle is defined as the phase difference between them. Thus, unitary operation on the spin is done by gate-controlled beam splitters, which partially transmit electrons between the spin-resolved QHECs, and phase shifters. Because of the preparation of the initial state with no entanglement, the first target should be to create a maximally entangled state if we set our goal to complete control of spin.

The previous studies found that the transmission between the spin-resolved QHECs occurs at the corner of the QHECs because effective magnetic fields arising from the spin-orbit interactions (SOI) change non-adiabatically. In addition, the phase difference, which corresponds to the azimuth angle, is shifted through the Aharonov-Bohm phase by changing the distance between the spin-resolved QHECs. However, independent control of the beam splitter and phase shifter was not established. In the present thesis (chapter 4), we show a concrete method for this independent control with a device consisting of multiple metallic gates. Notably, we find that the transmission probability at the corner of the QHECs is affected by the curvature.

In the experiment in chapter 4, the estimated transmission probability of the beam splitter was about 2%. However, a beam splitter with 50% of transmission probability, namely a half-mirror, is required to create a maximally entangled state, hence for the arbitrary unitary operations. Such a small transmission probability of the experiment in chapter 4 is attributable to the right-angled gate shape, limiting the rotation angle of the effective magnetic field of SOI. In chapter 5, we realize such a half-mirror by using an acute angle gate. We confirm coherent transmission at the BS by observing the Aharonov-Bohm interference with significantly high visibility of about 60%. The results indicate that we have realized a quantum state with a high degree of entanglement, probably the maximal entanglement.

We also show the results of transport simulation using the tight-binding model, indicating that the transmission probability of the beam splitter is affected by the angle of the gate corner and SOI strength, as well as the gradient of confining potential at the position of QHECs.

A remaining problem in getting our first target, a maximally entangled state, is the proof of quantum coherence. The interferometry guaranteed 60%, and we have tried a different approach henceforth. Although the coherence length of QHECs is significantly extended due to the chirality, it is still finite, which means that the decoherence does take place during the transport. Under highly-nonequilibrium conditions, e.g., finite voltages between the adjacent channels, inelastic inter-channel transmission is expected to be involved, leading to the enhancement of decoherence. Such an inelastic transmission should be measured as a reduction of shot noise in principle. However, the resolution of shot noise measurement required for this study is significantly high. In chapter 6, we show a novel high-resolution shot noise measurement system, which comprises homemade-HEMT-based cryogenic transimpedance amplifiers. In the subsequent chapter 7, we describe measurement of the shot noise generated by the transmission between the spin-resolved QHECs for the first time. The shot noise amplitude has asymmetric behavior for the sign of the bias voltage originating from the edge channel reconstruction. We have shown that the inter-channel transmission is elastic at the small source-drain bias condition, which supports the realization of the spin-orbit maximally entangled state.

Contents

List of Symbols and Abbreviations

e	electron charge
h	Planck's constant
c	velocity of light
m_{e}	free electron mass
m^*	effective electron mass in GaAs
k_{B}	Boltzmann's constant
μ_0	permeability constant
μ_{B}	Bohr magneton
$\phi_0 (= h/e)$	magnetic flux quantum
n	carrier density
E_{F}	Fermi energy
k_{F}	Fermi wave number
λ_{F}	Fermi wave length
μ	mobility
ν	filling factor of the Landau level
T	temperature
T_{e}	electron temperature
B	magnetic field
w_{c}	cyclotron frequency
ℓ_{B}	magnetic length
ρ	resistivity
σ	conductivity
I	current
V	voltage
G	conductance
C	capacitance
E	energy
ΔE	energy separation
E_{Z}	Zeeman energy
$D(E)$	(energy) density of states

$\boldsymbol{E}$	electric field
$\boldsymbol{v}_{\mathrm{d}}$	drift velocity
$\boldsymbol{r} = (x, y, z)$	spatial coordinate
$\boldsymbol{p}$	momentum operator
$\boldsymbol{A}$	vector potential
2DES	two-dimensional electron system
2DEG	two-dimensional electron gas
AC	alternating current
AB	Aharonov-Bohm
BS	beam splitter
DC	direct current
FQ	flying qubit
FSQ	flying spin qubit
HEMT	high-electron mobility transistor
MZI	Mach-Zehnder interferometer
QHEC	quantum Hall edge channel
QHES	quantum Hall edge state
QPC	quantum point contact
SEM	scanning electron microscope
SOI	spin-orbit interaction
SOMCS	spin-orbit maximally coupled system
SOMeS	spin-orbit maximally entangled system
TA	transimpedance amplifier

Chapter 1

Introduction

In this chapter, we briefly introduce a physical problem that we deal with throughout this thesis. Physics behind the problem is presented in the next chapter.

1.1 Preface

Quantum entanglement[1], which can be expressed as correlation between physical degrees of freedom, is one of the most critical consequences of quantum mechanics, having no counterpart in classical one. It is thus inherently important for quantum computation[2, 3].

The simplest form of the entanglement can be seen in the one on a pair of two-level systems. Let $\{|+\rangle_A, |-\rangle_A\}$ and $\{|+\rangle_B, |-\rangle_B\}$ be normalized bases of qubits A and B, respectively. Then one of the "maximally" entangled states of the pair is written as

$$|\Phi_+\rangle_{AB} = \frac{1}{\sqrt{2}}(|+\rangle_A |-\rangle_B + |-\rangle_A |+\rangle_B), \tag{1.1}$$

in which a deterministic measurement on one of the pair readily determines the other. To be quantitative, the entanglement entropy, which is defined as

$$S_{\rm A} = -{\rm Tr}[\rho_{\rm A} \ln \rho_{\rm A}] \tag{1.2}$$

for the partial system A is often adopted as the measure of entanglement. Here the reduced density matrix $\rho_{\rm A}$ (see Sec. 2.1) is obtained by tracing out the residual degrees of freedom in the total system. The state in (1.1), for example, gives the entanglement entropy as $S_{\rm A} = \ln 2$.

A representative two-level system in the real world is the spin 1/2 of fundamental particles like electrons, protons etc.[4, 5], and the total spin 1/2 of multiple particles can also be regarded as a two-level system. We can find an example of entanglement between the spin-1/2 systems in the historical experiment by Stern and Gerlach[6, 7, 8]. Figure 1.1 illustrates the experiment, in which 1/2-spin particles (in the experiment, Ag atoms) in the state $|\Phi_0\rangle = (1/\sqrt{2})\,|0\rangle\,(|\uparrow\rangle + |\downarrow\rangle)$ [orbit: $|0\rangle$, spin: $\{|\uparrow\rangle, |\downarrow\rangle\}$] were injected into an inhomogeneous magnetic field. After passing through the field, the wavefunction of a particle splits into two parts $\{|1\rangle, |2\rangle\}$, and the whole state can be written as

$$|\Phi\rangle = \frac{1}{\sqrt{2}}(|1\rangle\,|\uparrow\rangle + |2\rangle\,|\downarrow\rangle), \tag{1.3}$$

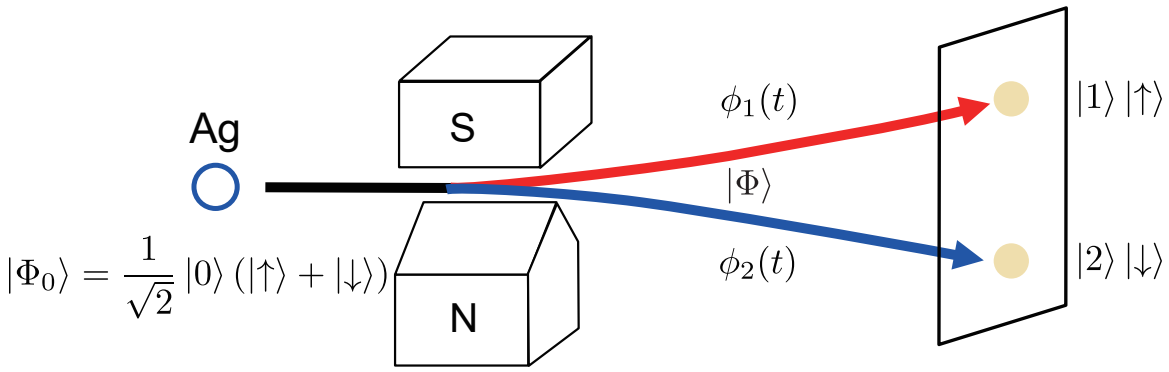

Figure 1.1: Schematic diagram of the Stern-Gerlach experiment.

which is nothing but a maximally entangled state between the spin and orbital degrees of freedom [cf. Eq. (1.1)]. In this state, the "which-path detection" is equivalent to the measurement of spins. This curious aspect of the Stern-Gerlach experiment has been mentioned in the context of quantum measurement [9], and various theoretical [10, 11, 12] and experimental[13, 14] studies have been conducted mainly in the field of neutron physics though in many textbooks on quantum mechanics (e.g., [15, 16]), the Stern-Gerlach experiment has been referred to as the discovery of quantized magnetic moment, i.e. spins.

Let us shift our perspective and consider the time evolution of the state described in the form of Eq. (1.3). When the wavefunctions of the orbits $|1\rangle$ and $|2\rangle$ develop with phase factors of $e^{i\phi_1}$ and $e^{i\phi_2}$ (the kinetic phases), the composite state becomes

$$|\Phi\rangle = \left(\frac{1}{\sqrt{2}}e^{i\phi_1}|1\rangle\right)|\uparrow\rangle + \left(\frac{1}{\sqrt{2}}e^{i\phi_2}|2\rangle\right)|\downarrow\rangle\,. \tag{1.4}$$

This phase evolution is naturally introduced from the kinetic motion but this state can be rewritten as

$$|\Phi\rangle = |1\rangle\left(\frac{1}{\sqrt{2}}e^{i\phi_1}|\uparrow\rangle\right) + |2\rangle\left(\frac{1}{\sqrt{2}}e^{i\phi_2}|\downarrow\rangle\right), \tag{1.5}$$

in which the phase factors also can be regarded as the ones of the spin degree of freedom such as a spin precession. This means that these two phenomena—the phase evolution and the spin precession—are quantum-mechanically indistinguishable in such orbital-spin maximally entangled states.

When the orbital degree of freedom of a spin-1/2 particle is quantized to two, the general state of the particle is expressed as a superposition of two-by-two state vectors $\{|1\rangle|\uparrow\rangle, |1\rangle|\downarrow\rangle, |2\rangle|\uparrow\rangle, |2\rangle|\downarrow\rangle\}$. There may be the case in which the system Hamiltonian effectively restricts the possible bases into two, say $\{|1\rangle|\uparrow\rangle, |2\rangle|\downarrow\rangle\}$, by pushing up the energies of the other two. In this case the particle state is written as

$$|\Psi\rangle = a|1\rangle|\uparrow\rangle + b|2\rangle|\downarrow\rangle \quad (a, b \in \mathbb{C}, \quad |a|^2+|b|^2= 1), \tag{1.6}$$

where the maximally entangled state with entanglement entropy of $\ln 2$ can only be achieved at $a = b = 1/\sqrt{2}$ as we will see shortly. However, there still exists a one-by-one corre-

spondence between the spin and orbital degree of freedom, keeping the validity of the above discussion on the phase evolution.

In this thesis, we call the system which only allows the state given in the form of (1.6) as **spin-orbit maximally coupled system (SOMCS)**. Hence, the complete set of SOMCS contains a spin-orbit maximally **entangled** state (SOMeS) in it. Since the SOMCS is a two-level system, it is more intuitive to express Eq. (1.6) in the Bloch-sphere representation:

$$|\Psi\rangle = \cos\frac{\theta}{2}|1\rangle|\uparrow\rangle + e^{i\phi}\sin\frac{\theta}{2}|2\rangle|\downarrow\rangle \quad (0 \leq \phi < 2\pi,\ 0 \leq \theta \leq \pi). \tag{1.7}$$

The SOMeSs correspond to the equator of the Bloch sphere. The unitary operations on SOMCS that changing θ change the entanglement between the spin and orbit. For example, spin $-\pi/2$ rotation in θ changes $|\Psi\rangle = (1/\sqrt{2})(|1\rangle|\uparrow\rangle + |2\rangle|\downarrow\rangle)$ ($a = b = 1/\sqrt{2}$ in (1.6)) to $|\Psi\rangle = |1\rangle|\uparrow\rangle$, in which the spin and the orbit are no longer entangled, i.e. the entanglement entropy is zero (see Sec. 2.1). In other words, some of the transport dynamics of SOMCS are described by the unitary matrix $U_{\rm SO}$, which contains interaction terms between spin and orbit. This is an essential difference from the unitary operations on spins in isolated systems.

SOMCS has a resemblance with composite systems of electrons and photons in the strongly coupled regime of so-called cavity QED[17], which is expected to be a key to handle quantum information both in electronic and photonic systems. Then in SOMCS, what sort of quantum operation on the spins via the orbitals, namely via the transport, is possible? The answer to this question is the primary target of our studies in this thesis. When we take the quantization axis of the spins along the magnetization axis, the zenith angle θ is determined by the partition rate between the orbits $\{|1\rangle, |2\rangle\}$ in the SOMCS, while the azimuth angle ϕ is defined as the phase difference between them. Thus, the unitary operation on the spin is done by gate-controlled beam splitters, which partially transmit electrons from one orbit $|1\rangle$ ($|2\rangle$) to the other orbit $|2\rangle$ ($|1\rangle$) with controllable transmission probability $\mathcal{T}$, and phase shifters (see Fig. 1.2). Because we prepare the initial state with no entanglement, the first target should be creating a maximally entangled state or a SOMeS if we set our goal to complete control of spin.

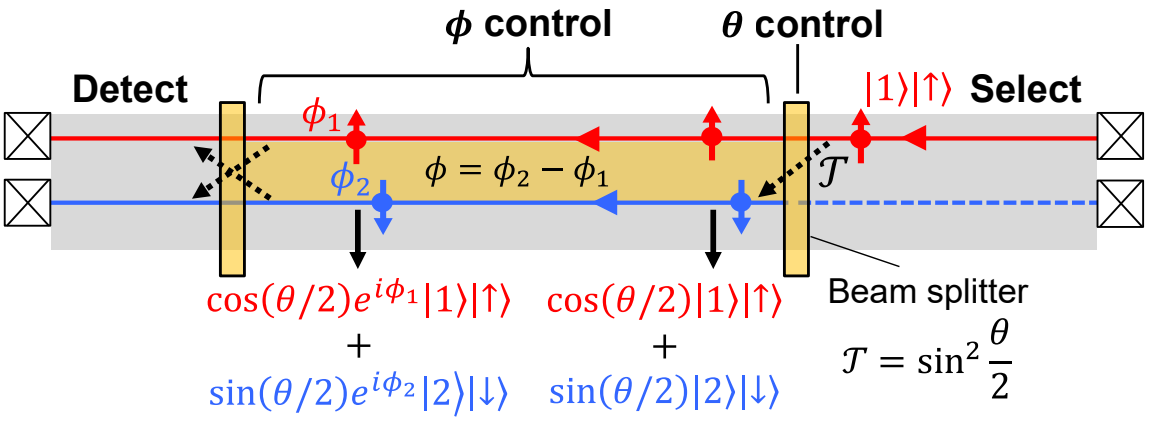

Figure 1.2: The procedure for quantum operations in SOMCS.

In order to carry out experimental studies on SOMCS, it is necessary to prepare a physical system that satisfies the following three requirements. First, the physical system should implement SOMCS. Second, the quantum coherence length of the system should be long enough to complete the quantum operation. Finally, we should be able to handle the orbital degree of freedom and to measure the quantum state of the system.

In order to prepare the SOMCS, we need to reduce the spin and orbital degrees of freedom effectively in addition to the coupling between the spin and orbital of a spin-1/2 particle. For the purpose we utilize the techniques in semiconductor nanotechnology. In the thesis we focus on the **spin-resolved quantum Hall edge states (QHESs)**, which form spin-resolved one-dimensional conduction channels at the edge of the two-dimensional electron system (2DES) in the integer quantum Hall state [Quantum Hall edge channels (QHECs)]. This system fulfills the above mentioned three requirements as follows. Firstly, adjacent copropagating QHECs are spin-polarized oppositely because of the Zeeman-split Landau levels and the electron correlation (quantum Hall ferromagnets); thus, the electron running in the QHEC can be treated as the SOMCS. Secondly, the longest coherence lengths in solids (> 0.25 mm [18]) have been reported for QHECs thanks to the chirality. Finally, spatial separation of spin-resolved channels can be easily electrically controlled by Schottky gates, which work as spin filters, and thus we can detect the electron spin through simple conductance measurements.

Although the coherence length of QHECs is significantly extended, it is still finite, which means that the decoherence does take place during the transport. The decoherence of the orbital degrees of freedom in QHECs has been intensively studied[19, 20, 21, 22], and it has been revealed that the thermal noise of the adjacent QHECs induces decoherence[21]. On the other hand, there is still some room for the study of the decoherence process in the spin degrees of freedom in QHECs. The two kinds of decoherence should be related through the entanglement. They are apparently equivalent in the case of the maximal entanglement. How the spin decoherence relates to the orbital decoherence when the state is not maximally entangled in SOMCS remains being a very interesting open question.

Under highly-nonequilibrium conditions, e.g. finite voltages between the adjacent channels, the frequency of the inter-channel transmission with spin flip generally increases, leading to the enhancement of decoherence in QHECs. The rate of such transmissions under a finite bias voltage should depend on the sign of voltage because of the difference in the electrostatic reconstruction of edge channels[23, 24, 25]. There have been discussions whether such transmissions are elastic or inelastic, which problem has a close relation to that of quantum coherence[24] though no experiment has been reported so far to the author's knowledge.

In the present study we have applied the shot-noise measurement to the above problem. The shot-noise measurement is a powerful tool to explore the nature of charge transmissions[26]. That is, the amplitude of the shot noise reflects the rate of inelastic transition in the transmission. The shot-noise measurement, on the other hand, requires complicated experimental techniques for picking up the noise signals, which are usually much smaller than the ordinary conductance signals, easily buried in the extrinsic noises. The Zeeman energy, which affects the reconstruction of spin-resolved QHECs, is usually on the order of several hundreds of μV. As we will discuss in the next chapter, the resolution of the shot-noise measurement required for the study of transmission between such edge states is signifi-

cantly high being the order of 10^{-29} A^2/Hz. Hence the development of a novel system for high-resolution shot-noise measurement is required.

The principal achievements of the present study are summarized as follows:

1. We have realized gate-controlled beam splitter and phase shifter for electrons traveling spin-resolved QHECs, which demonstrates the possibility of arbitrary unitary operations on the SOMCS [Chs. 4 and 5].

2. We also have shown a concrete method of varying the parameters of the above unitary transformation. Namely, in the Bloch-sphere representation, the azimuth angle is controlled by the distance between the adjacent QHECs. In contrast, the zenith angle is controlled by the angle of the edge corner and the SOI strength, and the distance [Chs. 4 and 5].

3. By applying the above method we have realized a beam splitter with transmission probability up to 50%, which means that we have made a candidate of SOMeS. A high ($\sim 60\%$) visibility obtained in a Mach-Zehder interferometer has supported the inference.

4. We have developed a system for novel high-resolution shot-noise measurement, which comprises homemade-HEMT-based cryogenic transimpedance amplifiers with a low input-referred noise and a wide frequency range. We have examined the resolution of the system by measuring the shot noise generated at a quantum point contact in a quantum Hall system, obtaining 6.9×10^{-31} A^2/Hz over the data-averaging time of 100 s, which is much better than those reported so far [Ch. 6].

5. We have measured the shot noise generated by the transmission between the spin-resolved QHECs for the first time. The amplitude of the shot noise, which reflects the rate of inelastic processes in the transmission, has shown asymmetric behavior against the bias voltage, originating from the edge channel reconstruction [Ch. 7]. We have shown that the inter-channel transmission is elastic for small bias voltage, which supports the realization of SOMeS.

1.2 Structure of this thesis

The structure of this thesis is as follows.

Chapter 2 Background

In Ch. 2, we introduce the theoretical and experimental backgrounds behind the physical problems presented above.

Chapter 3 Experimental technique

In Ch. 3, we describe the experimental methods used in this study. They include nanofabrication, low-temperature measurements, and electrical circuits for measurements.

Chapter 4 Gate-controlled unitary operation on flying spin qubits in quantum Hall edge states

In Ch. 4, we present the experimental results on the unitary operation of electron spins in QHECs through orbital control by the electric voltages on the metallic gates. The transport dynamics which affects the spin degree of freedom is systematically studied.

Chapter 5 Half-mirror on spin-resolved QHECs

In Ch. 5, we report the realization of the beam splitter on copropagating QHECs, using a metallic gate with an acute angle corner.

Chapter 6 Homemade-HEMT-based transimpedance amplifier for high-resolution shot-noise measurements

In Ch. 6, we explain the development of a cryogenic transimpedance amplifier suitable for mesoscopic current-noise measurements.

Chapter 7 Coherency of inter-channel transmission probed by shot noise

In Ch. 7, we present the result of shot-noise measurements of the BS on copropagating QHECs, with the TAs introduced in Ch. 6.

Chapter 8 Conclusion

Finally, we summarize this study and discuss future prospects.

Chapter 2

Physical background

In this chapter, we introduce the theoretical and experimental backgrounds behind the physical problems presented in the preface.

2.1 Quantum entanglement

As mentioned in the preface, quantum entanglement is a concept unique to quantum mechanics, and is being studied as a fundamental element in all fields of physics. The very basics are summarized below. We consider a quantum state described by $|\psi\rangle$ which is a vector in a Hilbert space. Such a state is called a pure state. A state that describes a whole isolated system is a pure state. For simplicity we put the norm of $|\psi\rangle$ is unity. Then the density operator for this state is given as

$$\rho = |\psi\rangle \langle\psi| . \tag{2.1}$$

Let $\mathcal{Q}$ be a physical quantity represented by an Hermite operator (i.e., $\mathcal{Q}^\dagger = \mathcal{Q}$). The expectation value of $\mathcal{Q}$ for $|\psi\rangle$ is given by

$$\langle\psi| \mathcal{Q} |\psi\rangle = \sum_q \langle\psi|q\rangle \langle q| \mathcal{Q} |\psi\rangle = \sum_q \langle q| \mathcal{Q} |\psi\rangle \langle\psi|q\rangle = \mathrm{Tr}[\mathcal{Q}\rho], \tag{2.2}$$

where $\{|q\rangle\}$ is an arbitrary complete basis set. It is also easy to see

$$\mathrm{Tr}[\rho] = 1, \quad \rho^\dagger = \rho. \tag{2.3}$$

Let us consider a bipartite system consisting of subsystems A and B. The reduced density operator for A is obtained by tracing out the degrees of freedom of B as

$$\rho_{\mathrm{A}} = \langle\rho\rangle_{\mathrm{B}} , \tag{2.4}$$

where ρ is the density operator for the total system and $\langle\cdots\rangle_{\mathrm{B}}$ expresses the averaging with respect to the degrees of freedom in B. The expectation value of a quantity $\mathcal{Q}$ is still given by $\mathrm{Tr}[\mathcal{Q}\rho_{\mathrm{A}}]$ and ρ_{A} fulfills the condition (2.3) though ρ_{A} is not always given in the form of (2.1). We write, then, ρ_{A} in a more general form:

$$\rho_{\mathrm{A}} = \sum_q p_q |q\rangle \langle q| = \sum_q p_q \rho_q, \tag{2.5}$$

where $|q\rangle$ represents a state of the subsystem A and p_q is the probability of its realization, hence $\sum_q p_q = 1$. The entanglement entropy (1.2) for the density operator in (2.5) is written as

$$S_{\mathrm{A}} = -\sum_q p_q \ln p_q. \tag{2.6}$$

When ρ_{A} is in the form of (2.1), $S_{\mathrm{A}} = 0$ because $\{p_q\} = \{1, 0, 0, \cdots\}$. The states represented by the density operator in (2.5) with multiple sub-density operators are called mixed states, representing a statistical mixture of quantum states. When the reduced density operator (2.4) is a mixed state, the states of subsystems A and B are **entangled**. In other words, the two states are unseparable when they are entangled. When ρ_{A} represents a pure state, the state of the whole system can be written as the direct product of those of the subsystems and the state is separable.

More specifically, let us consider the dimensions of A and B, N_{A} and N_{B} respectively. In the following discussion, we assume $N_{\mathrm{A}} \leq N_{\mathrm{B}}$ without loss of generality. Then the Schmidt decomposition of the pure state $|\Psi\rangle_{\mathrm{AB}}$ reads

$$|\Psi\rangle_{\mathrm{AB}} = \sum_{n=1}^{N_{\mathrm{A}}} \sqrt{p_n}\, |u_n\rangle_{\mathrm{A}}\, |v_n\rangle_{\mathrm{B}}\,, \tag{2.7}$$

where p_n is the probability distribution fullfilling $\sum_n p_n = 1$. If the coefficient $\sqrt{p_n}$ is 1 for an n and 0 for the others, Eq. (2.7) becomes a product $|\Psi\rangle_{\mathrm{AB}} = |u_n\rangle_{\mathrm{A}}\, |v_n\rangle_{\mathrm{B}}$, which is not an entangled state. In the other cases, $|\Psi\rangle_{\mathrm{AB}}$ describes entangled states.

When there is a one-to-one correspondence between the states in A and those in B, the system is in a **maximally entangled state**. For example, in the case of a pair of two-level systems A and B, the state

$$|\Phi_+\rangle_{AB} = \frac{1}{\sqrt{2}}(|+\rangle_A\, |-\rangle_B + |-\rangle_A\, |+\rangle_B) \tag{2.8}$$

is a maximally entangled state. In addition to Eq. (2.8), the states obtained by any local unitary operations $\hat{U}_{AB} = \hat{U}_A \otimes \hat{U}_B$ on $|\Phi_+\rangle_{AB}$ are also maximally entangled.

2.2 Quantum Hall edge channels (QHECs)

Let us introduce the spin-resolved quantum Hall edge states as an ideal platform of SOMCS. A magnetic field B perpendicular to a two-dimensional electron system (2DES) causes the quantum Hall effect as shown in Fig. 2.1(a) [27]. In this regime, the Hall resistance forms plateaus, on which the Hall resistance is quantized to

$$R_{xy} = \frac{h}{e^2}\frac{1}{\nu} \quad \nu \in \mathbb{Z}. \tag{2.9}$$

In addition, the longitudinal resistance R_{xx} in the plateau region becomes zero.

This phenomenon can be explained by the formation of edge states flowing along the 2DES edges as follows. Under the magnetic field B perpendicular to the 2DES, the

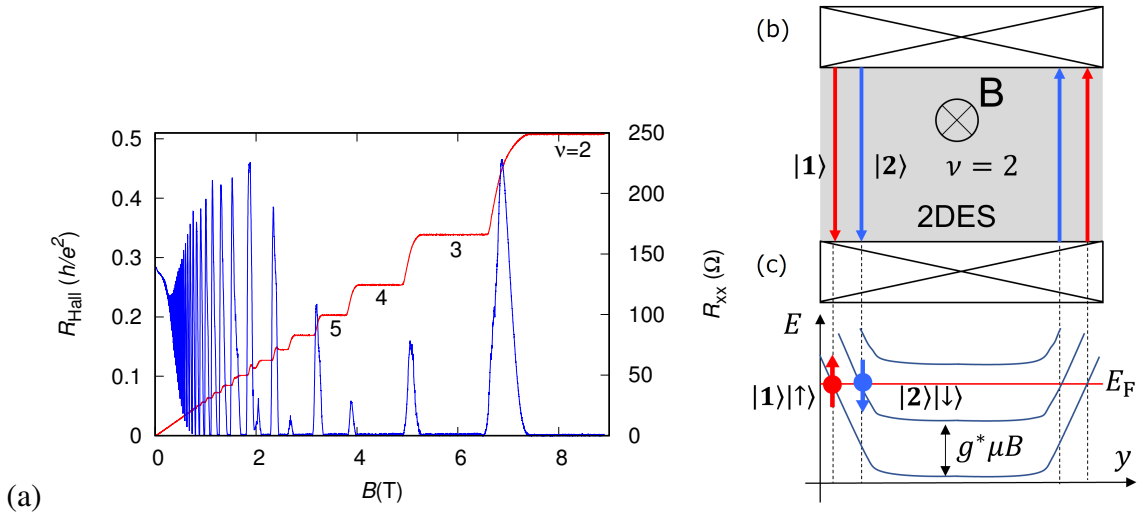

Figure 2.1: (a) Hall resistance $R_{\rm Hall}$ (red line) and longitudinal resistance $R_{\rm xx}$ (blue line) as a function of the magnetic field B applied perpendicular to the 2DES. The filling factor ν corresponding to each plateau is indicated. (b) Schematic diagram showing the formation of quantum Hall edge states. (c) Schematic of the Landau levels along the edges of the sample in the quantum Hall regime. The confinement potential near the edge of the sample bends the Landau levels upward. The edge state is formed at the intersection of $E_{\rm F}$ and the Landau levels.

eigenenergies of electrons are quantized to the Landau levels

$$E_n = \left(n + \frac{1}{2}\right)\hbar\omega_{\rm c} \quad (n = 0, 1, 2, \cdots), \tag{2.10}$$

the derivation of which is shown in Appendix B.1. Here, $\omega_{\rm c} = eB/m_{\rm e}^*$ is the cyclotron frequency and $m_{\rm e}^*$ is the effective mass of the electron. The confinement potential near the edge of the sample shifts these Landau levels upward as shown in Fig. 2.1(c). When the Fermi energy $E_{\rm F}$ is located between two Landau levels, $E_{\rm F}$ intersects the lower Landau level in such an up-bending region, and an edge state is formed at the intersection as shown in Fig. 2.1(b). Two-dimensional bulk Landau levels form flat bands i.e., bands with no dispersion $dE_n/dk = 0$ for wavenumber k as in Appendix B.1. Therefore, the mobility is zero, and the Landau-quantized electrons in the bulk cannot move.

In the up-bending region near the edge, however, the situation changes because the eigenenergies depend on the spatial position. The bulk Landau levels are heavily degenerated and the eigenstates can take various spatial forms. Around the edge, the two-dimensional symmetry is broken by the edge potential and the forms in Eq. (B.11) are appropriate since they extend in one dimension [y in the case of Eq. (B.11)] as plane waves and localized in the other dimension. In Eq. (B.11), the wavenumber k depends on the positions of the center of localization. On the other hand, the eigenenergies shift with the spatial position on the dimension perpendicular to the edge. As a result, the energy dispersions gain finite values $dE_n/dk \neq 0$, letting the electron propagation along the edge possible. The sample edge breaks the spatial inversion symmetry along the direction perpendicular to the edge, simultaneously breaking the inversion symmetry of electron propagation along the edge. That is, the electron can propagate only in one direction along the edge. This

property of the edge states is called the **chirality**. In the classical picure, the edge states correspond to the skipping orbit of the cyclotron motion (see Appendix B.2).

Due to the chirality the electrons propagating on one edge have their counter-propagating state on the other edge. Hence the backscattering of an edge electron is almost prohibited in macroscopic non-structured samples by the requirement of the edge-to-edge electron transfer. The electrons travel through the edge states without scattering, resulting in zero R_{xx} when the voltage drop is measured along the edge (four-terminal resistance). The voltage between the two edge states i.e., the Hall voltage appears as voltage drops at so-called hot spots in the current terminals. The two terminal resistance is then finite and equals to the Hall resistance. The Landauer formula[28, 29] for a perfect one-dimensional conductor tells that the two-terminal conductance should be an integer times e^2/h. The integer here is the number of quantum states along the conductor. This explains the quantization of the Hall resistance in Eq. (2.9) and the integer ν is the number of Landau levles below $E_{\rm F}$, called the filling factor.

In general, the influence of the electron-electron interaction is large in one-dimensional systems, and it is necessary to take this into account in addition to the one-electron picture described above. According to Ref. [30], the electron-electron interaction screens the edge potential, so that the dispersion of the edge states is again close to flat, and the effective mass becomes very large, depending on the edge potential. This point will be considered again in the following subsection, as it is essential in considering our experiments.

This quantum-Hall edge state is known to have a very long coherence length. This property has been clarified and applied using Mach-Zhender interferometry[31, 20] and other techniques [32].

At high magnetic fields, each Landau level is split with respect to spin due to the Zeeman effect and the effect of the electron-electron correlation[33]. The two effects are represented by the effective Zeeman energy $-g^*\mu B$, where g^* is the effective g-factor, which can grow very large with the magnetic field and the ferromagnetic interaction between the spins[34, 35]. This leads to the spin-splitting of the Landau levels at relatively low magnetic fields. In Fig. 2.1(a), which shows our experimental data, the spin-splitting is observed above the field for filling factor $\nu = 7$. In the spin-splitted states, the spins belonging to the adjacent edge states are polarized in the opposite directions. Quantum mechanical superposition of the two adjacent spin-polarized edge states is expressed as

$$|\Psi\rangle = a\,|1\rangle\,|\uparrow\rangle + b\,|2\rangle\,|\downarrow\rangle \quad (a, b \in \mathbb{C}), \tag{2.11}$$

where (1, 2) and ($\uparrow$, $\downarrow$) are the indices of edge states and spins, respectively. This is nothing but an SOMCS in the same form as (1.6). However, Eq. (2.11) is still just an attempt to write down the state in this way, and it is not clear at all whether such a quantum-mechanical superposition can be realized in practice. One of the main arguments of this paper is that the states written as Eq. (2.11) are realizable up to the maximal entanglement $|a| = |b| = 1/\sqrt{2}$ (i.e., SOMeS), and as a result it is possible to control the spin by controlling the orbital, though as will be discussed in detail later, there remains the problem of quantum coherence. In this sense, the finding of SOMeS is the holy grail in the present study. This corresponds to the control of one quantum-mechanical degree of freedom with the other one through strong coupling just as the field of cavity-QED is aiming at.

2.3 Previous studies on spin-resolved QHECs

This section reviews the studies related to the unitary operation on spins in spin-resolved QHECs. In macroscopic, non-structured samples, the tunnelings between counter-propagating edge states at the opposite edges are negligible. On the other hand, the distance between spin-resolved copropagating QHECs is determined by the potential gradient and the spin-splitting energy. Under ordinary experimental conditions of heterostructure 2DES, the distances are on the order of several nm. Therefore, it is possible to realize quantum-mechanical tunneling between the spin-resolved copropagating QHECs if some coherent spin-flip mechanism can be introduced.

2.3.1 Inter-channel scattering in QHECs

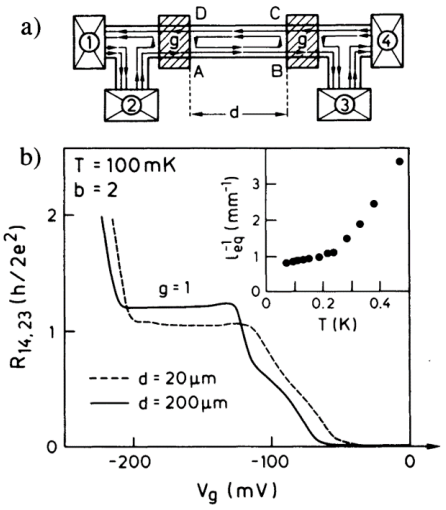

Figure 2.2: (a) Schematic diagram of the device. The edge states are drawn for the condition that the filling factor in the non-gated region b is 2 and that below the gate g is 1. (b) The four-terminal resistance $R_{14,23}$ (i.e., the current terminals are 1 and 4, the voltage terminals are 2 and 3) is plotted against the left and right gate voltages. A plateau is observed around $V_g = -160$ mV, where $g = 1$. The increment in d (the distance between the two gate electrodes) enhances the probability for the transitions between the edge states, causing deviation of the resistance from the quantized value (Müller *et al.* [36]).

Preliminary studies on spin-flip inter-channel transmission in QHECs were conducted by Müller et al. [36, 37, 38]. They observed inter-channel transmissions caused by impurity scatterings, and claimed that the SOI was the mechanism for the spin-flip. Figure 2.2(a) is a schematic diagram of the device, showing the QHECs when the filling factor in the non-gated region was 2 (perpendicular magnetic field: $B = 3.9$ T) and the filling factor below the gates was 1. When there was no inter-channel transmission, the four-terminal resistance $R_{14,23} = V_{23}/I_{14}$ was expected to be $h/2e^2$, where I_{14} was the current flowing between contacts 1 and 4 and V_{23} was the voltage difference between contacts 2 and 3. On the other hand, the inter-channel transmissions with spin-flip in the sample edge A-B or

C-D lead to the backscattering from one edge A-B (C-D) to the other edge C-D (A-B) by way of the circulating edge state at the center in Fig. 2.2(a), leading to the higher resistance $R_{14,23}$ than $h/2e^2$.

Figure 2.2(b) shows measured $R_{14,23}$ as a function of the left and right gate voltages $V_{\rm g}$ for the two samples, one with the distance between AB of $d = 20$ μm (dashed line) and the other with $d = 200$ μm (solid line). In both cases $R_{14,23}$ showed a plateau at around $V_{\rm g} = -150$ mV, indicating that the filling factors under the gates were 1 in these plateau regions. An apparent deviation from the quantized resistance of $R_{14,23}$ is observed for the sample with $d = 200$ μm, while the deviation was significantly smaller for the one with $d = 20$ μm. Assuming a constant number of scattering events between the outer and inner edge channel per unit length $l_{\rm eq}^{-1}$, the authors of Ref. [36] obtained the expression of the resistance as

$$R_{14,23} = \frac{h}{e^2}\left[1 + \exp\left(-\frac{2d}{l_{\rm eq}}\right)\right]^{-1}, \tag{2.12}$$

where $l_{\rm eq}$ is the equilibration length, which corresponds to the distance an electron travels between two scattering events. From the experiment and Eq. (2.12), they obtained $l_{\rm eq} = 940$ μm for $d = 200$ μm.

The authors raised three possible physical processes responsible for the spin-flip scattering: the magnetic impurity scattering, the SOI, and the hyperfine interaction with nulear spins. It is unlikely that magnetic impurity is mixed in during the MBE growth of GaAs heterostructure, and hence they ruled out this possibility. For the hyperfine interaction, the electronic spin flip is accompanied by a nuclear spin-flip, and therefore the total spin is conserved. The Rashba and Dresselhaus SOI are caused by the lack of inversion symmetry at the heterojunction interface and in the zinc-blende crystal structure of GaAs, respectively. In the case of SOI, the spin-flip of an electron is accompanied by a change in the electronic momentum.

They assumed that the SOI is more relevant for spin relaxation than the hyperfine interaction, and then the spin-flip equilibration length $l_{\rm eq}$ at 160 μm theoretically, which is the same order of the measured $l_{\rm eq} = 940$ μm.

Here we briefly review their theoretical treatment. Details of this calculation are shown in Ref. [37]. The starting point is the Hamiltonian $H = H_0 + H_1$, where

$$H_0 = \frac{p^2}{2m} + V(y). \tag{2.13}$$

The Hamiltonian H_0 describes the motion of a 2DES electron in a confining potential in the y direction and in the presence of a perpendicular magnetic field B with $\boldsymbol{p} = -i\hbar\nabla - e\boldsymbol{A}$, where $\boldsymbol{A}$ is the vector potential. The perturbative part is given by

$$H_1 = \alpha \boldsymbol{n}\cdot(\boldsymbol{p}\times\boldsymbol{\sigma}) + \beta\boldsymbol{\sigma}\cdot\boldsymbol{\kappa} + \frac{1}{2}g\mu_B B\sigma_z, \tag{2.14}$$

where $\boldsymbol{n}$ is the unit vector perpendicular to the 2DES plane, $\boldsymbol{p}$ the momentum operator, $\boldsymbol{\sigma}$ the vector of the Pauli matrices, $\boldsymbol{\kappa}$ a vector that depends on the crystal direction, the momentum, α and β are constants. The first and second terms of Eq. (2.14) describe the

Rashba and Dresselhaus SOIs, respectively. The third term is the Zeeman energy. For the 2DES on (001) $\boldsymbol{n} \cdot (\boldsymbol{p} \times \boldsymbol{\sigma}) = (p_x\sigma_y - p_y\sigma_x)$ and $\boldsymbol{\kappa} = (-p_x, p_y, 0)$.

Using the spin-degenerate eigenstates $\exp(ikx)\phi_k(y)$ of H_0 (see Appendix B.1) to treat H_1 perturbatively, we find the energy splitting at any value of k to be

$$2\Delta = \sqrt{(g\mu_B B)^2 + (2mv_x)^2(\alpha^2 + \beta^2)}, \tag{2.15}$$

with v_x the group velocity of an edge channel electron (The details of this derivation is also found in Ref. [39]). They neglect α for the numerical calculation of the effective magnetic field $2mv_x\sqrt{\alpha^2 + \beta^2}/(g\mu_B)$ arising from the SOI, assuming that α is smaller than β. In the single particle picture, the group velocity of an edge channel electron is given by $v_x = F_{\rm edge}/B$, where $F_{\rm edge}$ is the linear edge electric field at the position of an edge channel (see Eq. (B.12)). With $F_{\rm edge} = \hbar\omega_c/(e780\ \text{Å})$, where 780 Å is the spatial seperation between two adjacent (spin-degenerate) edge channels for a Landau gap of 3.2 meV reported by their other experiment, they obtained $v_x = 1 \times 10^4$ m/s and a value of about 0.9 T for the effective magnetic field. We note that their estimation of v_x is of the same order as the one obtained by the time-of-flight measurement reported recently[40], but it is, of course, strongly sample dependent. The presence of the SOI terms in the Hamiltonian allows transmissions between spin-split edge channels in the presence of any scattering mechanism which changes the wave vector along the boundary. Elastic transmissions between the edge channels not only change $k = -y/l_c^2$ [with the center coordinate y (see Appendix B.1)] but also the group velocity. In the Born approximation, they obtained for the equilibration length, with i indicating the initial and f the final state,

$$l_{\rm eq} = l_0/|\chi_+^\dagger(k_i)\chi_-(k_f)|^2. \tag{2.16}$$

Hence the equilibration length is inversely proportional to the spinor overlap, and the parameter l_0 corresponds to the scattering length of the spin-free problem. Assuming $\delta v_x = |v_{x,i} - v_{x,f}| \ll v_x$, we write the spinor product as

$$\chi_+^\dagger(k_i)\chi_-(k_f) = \frac{\delta v_x}{v_x}[g\mu_B B m v_x\sqrt{\alpha^2 + \beta^2}/(4\Delta^2)]. \tag{2.17}$$

The scattering caused by a long-range potential of the remote ionized donors gives $l_0 \sim 4$ Å. The large value of the equilibration length observed must therefore be due to a small spinor overlap in Eq. (2.16). To estimate δv_x, they took a parabolic confinement potential with a confinement frequency of $\Omega_0 = 7.8 \times 10^{11}\ \text{s}^{-1}$, which directly follows from their estimated group velocity of the edge channel. Using $\delta v_x/v_x = (l_c^2 m\Omega_0^2\delta y)/(\hbar v_x)$, they obtained the equilibration length of $l_{\rm eq} = 160\ \mu\text{m}$.

In the above experiment, the spin-flip inter-channel transmissions were caused by the potential inhomogeneity due to the *random* donor impurities. Thus it was difficult to clarify the details of the relation between the potential profile and transmissions.

2.3.2 Gate-Control of Spin Precession in Quantum Hall Edge States

Nakajima *et al.* [41, 42] found that the inter-channel transitions are triggered at the corner of the edge channels and demonstrated the way to observe and control the spin-precession.

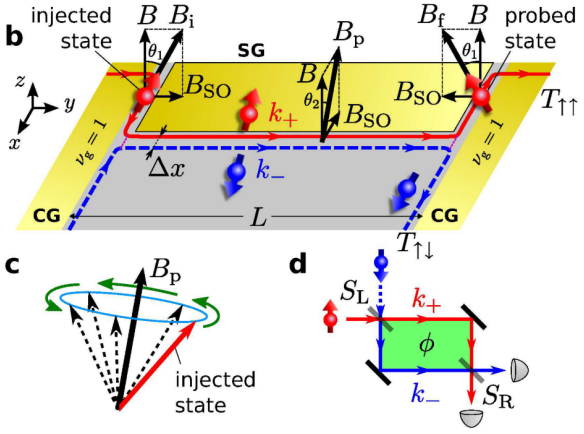

Figure 2.3: (b) Schematic of the sample for observing spin precession in a spin-resolved QHECs in Ref. [41]. (c) illustrates spin precession around the effective magentic field during the electron propagation on a QHEC. (d) Schematic diagram of the edge-state interferometer.

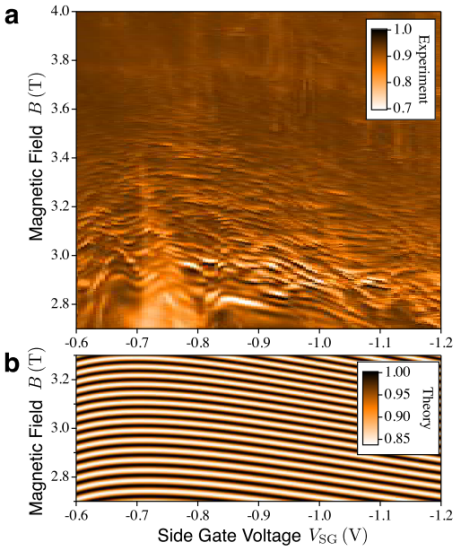

Figure 2.4: (a) Color plot of the transmission probability $T_{\uparrow\uparrow}$ as a function of the magnetic field and the SG gate voltage [41]. (b) Color plot of the transmission probability obtained from a model calculation.

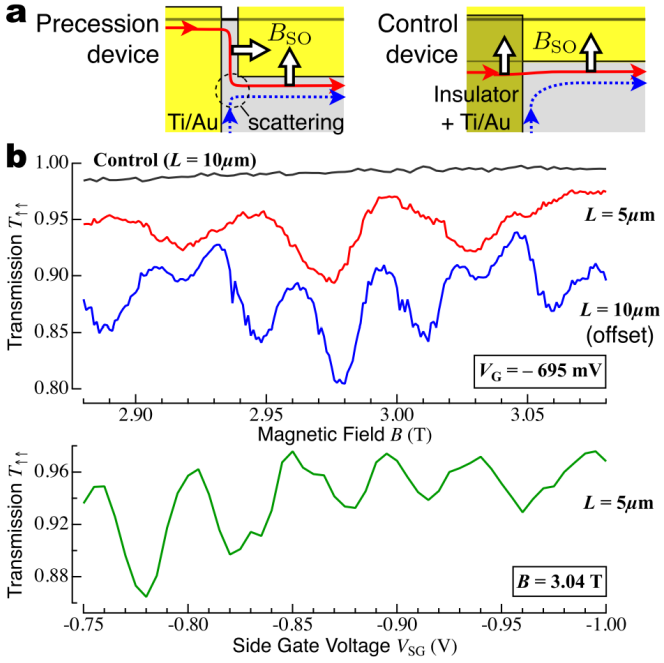

Figure 2.5: (a) Schematics of the device in Fig. 2.3 (left) and the control device (right), focusing on the region where two edge states encounter with each other. (b) $T_{\uparrow\uparrow}$ against B (upper panel) and $V_{\rm SG}$ (lower panel) [41].

Figure 2.3 is a schematic diagram of the sample they used. After the 2DES is brought into the quantum Hall state by applying a magnetic field $\boldsymbol{B}$ perpendicular to the surface, the filling factor under the gates CG is set to $\nu_{\rm g} = 1$ and that under the gate SG is set to 0 by applying the negative voltages to the gates. When the filling factor of the non-gated region is $\nu = 2$, the edge channel configureation is arranged as denoted by red ($\uparrow$ spins) and blue ($\downarrow$ spins) lines in the figure. Spin-polarized edge states are quantized in the effective magnetic field $\boldsymbol{B}_{\rm eff} = \boldsymbol{B}_{\rm SO} + \boldsymbol{B}$, where $\boldsymbol{B}_{\rm SO}$ is the SOI-induced effective magnetic field. Electrons running along the left side of gate SG are spin-polarized in the direction of $\boldsymbol{B}_{\rm i}(= \boldsymbol{B}+\boldsymbol{B}_{\rm SO})$. When an electron on an edge state goes around the left corner of gate SG, $\boldsymbol{B}_{\rm i}$ changes to $\boldsymbol{B}_{\rm p}$ nonadiabatically, and the spin starts precession around the axis of $\boldsymbol{B}_{\rm p}$ as in Fig. 2.5(c). The projection of the state at the right corner onto the up-spin eigenstate for $\boldsymbol{B}_{\rm eff} = \boldsymbol{B}_{\rm f}$ is read out by the Hall voltage. The phase of precession is determined by the Larmor frequency and the group velocity, which can be experimentally controlled by $\boldsymbol{B}$ and the gate SG bias voltage, respectively.

The electronic state running in the y direction along the gate SG is

$$a_0 e^{ik_+ y} \left|+\right\rangle + b_0 e^{ik_- y} \left|-\right\rangle . \tag{2.18}$$

Here, $\left|+\right\rangle$ and $\left|-\right\rangle$ are the wavefunctions of the electrons in the $\uparrow$ and $\downarrow$ edge states, respectively, and $a_0,\ b_0$ are determined by the magnitude of the change in $\boldsymbol{B}$. The factors $e^{ik_+ y}$ and $e^{ik_- y}$ are the kinetic phases acquired during the propagation along the gate SG. In the spin picture, this is the spin precession with the direction of $\boldsymbol{B}_{\rm p}$ as the axis, as shown in Fig. 2.3(c) and as we discussed in sec. 2.2. When the electron reaches the right CG gate, another non-adiabatic transition occurs, and only the $\uparrow$ spin passes through the right CG gate. The transmission probability $T_{\uparrow\uparrow}$ of the electron entering through the left CG gate and exiting the right CG gate is expressed by

$$\begin{aligned} T_{\uparrow\uparrow} &= \left| \left\langle\uparrow\right| S_{\rm R} \begin{pmatrix} e^{ik_+ y} & 0 \\ 0 & e^{ik_- y} \end{pmatrix} S_{\rm L} \left|\uparrow\right\rangle \right|^2 \\ &= C_0 + C_1 \cos(\phi(L) + \phi_0), \end{aligned} \tag{2.19}$$

where $\phi(L) = (k_+ - k_-)L$. The difference in the wavenumber between the edge states, $k_+ - k_-$, is given by $\Delta x / l_B^2$. Since the distance between edge states Δx is strongly influenced by the confining potential created by the gate SG, $T_{\uparrow\uparrow}$ should vary with the SG gate voltage. Figure 2.4 shows the results of $T_{\uparrow\uparrow}$ obtained experimentally and the results of numerical calculation of $T_{\uparrow\uparrow}$ based on the above model as a function of $\boldsymbol{B}$ and the SG gate voltage. Because of the qualitative agreement between the two, they claimed to have observed the spin precession and were able to control the phase with the SG gate voltage.

2.4 Open issues for the present study

As mentioned in Ch. 1, a spin-1/2 system is a two-level system, which is often referred to as a "qubit" in the field of quantum information. In particular, spatially moving particles with spin 1/2 are considered as the carriers of quantum information, and in that sense called flying spin qubit (FSQ)[43]. The electrons propagating through QHECs can also be viewed

as FSQs. From this point of view, the creation of quantum superposition in Eq. (2.11) corresponds to the split of particle beam to strongly entangled states. Hence the subject raised in Sec. 2.2, the realization of maximally entangled states or SOMeS, is rephrased as the realization of a *coherent* half-mirror-type beam splitter (BS).

From the viewpoint of FSQ operation, the study in Sec. 2.3.2 paved the way to make BSs and phase shifters. In addition, their method is the manifestation of the quantum operation on SOMCS state with orbital control, without using a *local* magnetic field, e.g., ferromagnets or microwave. Their study raises the following interesting questions.

First, what factors affect the transmission at the corner of the edge channels? In the experiment in Sec. 2.3.2, the visibility of the oscillation is up to 8 %, and thus we can estimate the minimum transmission probability of the BSs as 2 %, assuming no decoherence at the interferometer. They claim that the obtained transmission probability is smaller than but on the same order of the predicted value in the non-adiabatic limit because the adiabaticity and the finite distance between the QHECs at the corner reduced the transmission probability. However, these are not well established, leaving rooms for study.

Second, is it possible to control the transmission probability (zenith angle θ of FSQ) and phase (azimuth angle ϕ of FSQ) independently? They used the SG gate to adjust the phase differences. However, if the above hypothesis is correct, the voltage on the SG gate changes the potential profile at the corner of the SG gate, which should affect the transmission probability. It is shown that the oscillation amplitude decreases with a negative SG gate voltage (see Fig. 2.5), indicating the decrease in the transmission probability. Thus, the SG gate voltage may change not only ϕ but also the non-adiabatic transition matrices $S_{\rm L}$ and $S_{\rm R}$, and θ may change simultaneously. For a well-defined unitary operation and clear knowlege on quantum state of FSQs, we need to control the transmission probability and the phase shift independently.

Finally, how about the coherence of the operation? Quantum operation on FSQs should be done coherently, and thus it is significant to evaluate the coherence itself. In Mach-Zehnder interferometers (MZIs), we can estimate a lower bound of coherence from the oscillation visibility when the transmission probability of each BS is given. However, the visibility just gives a lower bound[31], and it is difficult to estimate the coherence directly from the experiments in MZIs. Thus, we need a method of measuring a single BS's transmission probability directly. The decoherence may occur both at the BSs and inside the interferometer, and it is essential to distinguish the origin of decoherence to reveal the transport dynamics of spin-resolved QHECs. The decoherence is brought about from various origins, e.g., inter-channel scatterings and capacitive couplings inside the interferometer and inelastic scatterings.

2.5 Shot-noise measurements

In Ch. 6, we present the study on a shot-noise measurement system. Then, the study of elastic/inelastic transmission between the spin-resolved QHECs with the shot-noise measurement is given in Ch. 7. Here we briefly review the basics of shot-noise measurements [44, 26, 45] and theory of shot noise caused by the elastic/inelastic transmission between the QHECs.

2.5.1 Basics of shot noise

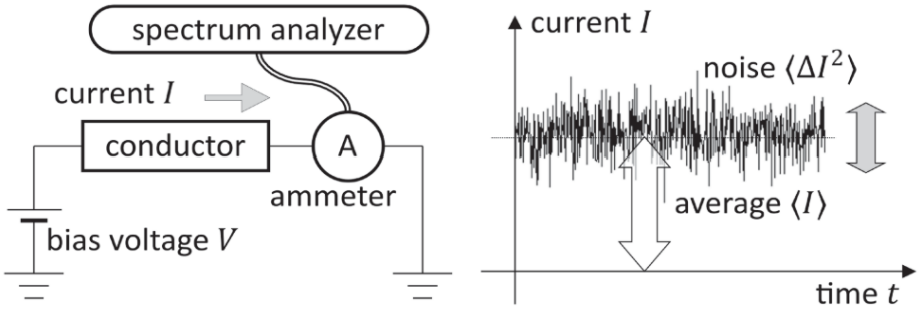

Figure 2.6: Left: Setup for current and noise measurement. Right: Illustration of the definitions of noise (Kobayashi *et al.* [26]).

Figure 2.6 shows a schematic diagram of current noise measurement. We apply a bias voltage V on a conductor and measure the current I with an ampere meter. The measured current I fluctuates around its time average $\langle I \rangle$ as a function of time t, and the current noise S is defined as

$$S \equiv \left\langle \Delta I^2 \right\rangle = (I - \langle I \rangle)^2. \tag{2.20}$$

The noise S consists of a variety of noise sources, e.g., the 1/f noise, the thermal (Johnson-Nyquist) noise, and the shot noise. Thus, S is generally frequency dependent, the power-spectral density of the current noise is usually defined as

$$S(f) = 2 \left\langle \Delta I(t)^2 \right\rangle_f (\Delta f)^{-1}, \tag{2.21}$$

where $\langle \Delta I(t)^2 \rangle_f$ is the avaraged current fluctuation with the center frequency f in the range of Δf.

The time-averaged current $\langle I \rangle$ is expressed by the avaraged number of electrons $\langle N \rangle$ propagating through the samples as

$$\langle I \rangle = e \langle N \rangle \tau^{-1}, \tag{2.22}$$

where τ is the time for counting electrons. The current noise is given by the averaged variance $\langle \Delta N^2 \rangle$ as

$$S(f) = 2e^2 \left\langle \Delta N^2 \right\rangle \tau^{-1}. \tag{2.23}$$

The shot noise is a consequence of a stochastic partition process of electrons at a barrier (see Fig. 2.7). Let us consider the case of N' particles hitting a barrier, and each particle is either independently transmitted with a probability of $\mathcal{T}$ or reflected with $1-\mathcal{T}$. The detector counts the number of transmitted particles. The probability distribution of transmission is given as the Bernoulli (binomial) distribution as

$$P_{N'}(N) = \frac{N'!}{N!\,(N'-N)!} \mathcal{T}^N (1-\mathcal{T})^{N'-N}, \tag{2.24}$$

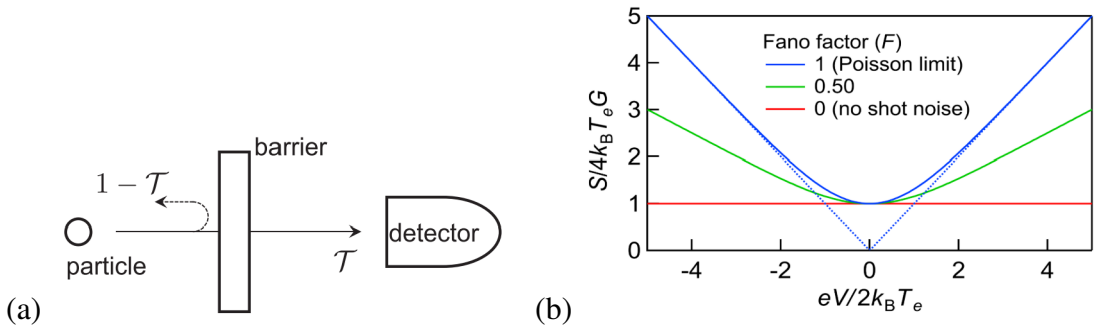

Figure 2.7: (a) Illustration that schematically shows scattering of a particle by a barrier. $\mathcal{T}$ and $1-\mathcal{T}$ are the transmission probability and reflection probability, respectively. (b) Dimensionless quantity $S/(4k_{\mathrm{B}}T_{\mathrm{e}}G)$ is shown as a function of the voltage normalized to the temperature $eV/2k_{\mathrm{B}}T_{\mathrm{e}}$ for three Fano factors (Kobayashi *et al.* [26]).

where N is the number of the transmitted particles. From the distribution, $\langle N\rangle$ and $\langle\Delta N^2\rangle$ are calculated as

$$\langle N\rangle = N'\mathcal{T}, \tag{2.25}$$

$$\left\langle \Delta N^2\right\rangle (\equiv \left\langle (N-\langle N\rangle)^2\right\rangle) = N'\mathcal{T}(1-\mathcal{T}) = \langle N\rangle\,(1-\mathcal{T}). \tag{2.26}$$

Substituting Eq. (2.26) into Eq. (2.23) and using Eq. (2.22), we obtain the shot-noise formula as

$$S_{\mathrm{shot}} = 2e\,\langle I\rangle\,(1-\mathcal{T}). \tag{2.27}$$

Equation (2.27) is also called a partition noise. In the limit where $\mathcal{T}$ is small ($\mathcal{T} \ll 1$), Eq. (2.27) becomes

$$S_{\mathrm{p}} = 2e\,\langle I\rangle\,. \tag{2.28}$$

Equation (2.28) is the well-known expression of the shot noise given by Schottky in 1918[46]. When $\mathcal{T} \ll 1$, $\langle N\rangle = \langle\Delta N^2\rangle = N'\mathcal{T}$ holds and this is nothing but the signature of the Poisson distribution. Therefore, Eq. (2.28) is also referred to as the Poisson limit of the shot noise.

In deriving Eq. (2.28), we assumed that the tunneling process of each electron is independent of each other, and the process is Poissonian ($\mathcal{T} \ll 1$). However, S_{p} can deviate from Eq. (2.28) for some mechanisms such as the Pauli exclusion principle or the Coulomb interaction, and thus the deviation itself has significant information of electron dynamics. Thus, it is useful to introduce the Fano factor F, which is the ratio of the measured shot noise $S_{\mathrm{shot}}^{\mathrm{meas}}$ to the Poisson limit as

$$F \equiv \frac{S_{\mathrm{shot}}^{\mathrm{meas}}}{S_{\mathrm{p}}} = \frac{S_{\mathrm{shot}}^{\mathrm{meas}}}{2e\,|\langle I\rangle|}. \tag{2.29}$$

The general formula for the current noise is written as

$$S = \frac{e^2}{\pi\hbar}\int d\epsilon \sum_{\alpha,\beta} A_L^{\alpha\beta}(\epsilon,\epsilon)A_L^{\beta\alpha}(\epsilon,\epsilon)f_\alpha(\epsilon)[1-f_\beta(\epsilon)]. \tag{2.30}$$

The derivation of Eq. (2.30) is described in Ref. [45]. Here, $f(\epsilon)$ is the Fermi distribution function, and the matrices A are related to the on-shell S matrix: $A_{\rm L}^{\alpha\beta} = \delta_{{\rm L}\alpha}\delta_{{\rm L}\beta} - s_{{\rm L}\alpha}^{\dagger} s_{{\rm L}\beta}$, where s are the components of the S matrix of the conductor under consideration. When we consider the scattering process between the incoming ($a_{\alpha,k}$) and outgoing ($b_{\alpha,k}$) electrons in lead α ($\alpha =$ L or R), the S matrix $\mathcal{S}_{\rm cond}$ of the conductor is defined as

$$\begin{pmatrix} b_{{\rm L},k} \\ b_{{\rm R},k} \end{pmatrix} = \mathcal{S}_{\rm cond} \begin{pmatrix} a_{{\rm L},k} \\ a_{{\rm R},k} \end{pmatrix}, \tag{2.31}$$

where

$$\mathcal{S}_{\rm cond} = \begin{pmatrix} s_{\rm LL}(k) & s_{\rm LR}(k) \\ s_{\rm RL}(k) & s_{\rm RR}(k) \end{pmatrix} = \begin{pmatrix} r & t' \\ t & r' \end{pmatrix}. \tag{2.32}$$

The S matrix relates the incoming amplitudes to the outgoing amplitudes: the element $s_{\alpha\beta}(E)$ gives the amplitude of the current probability in channel α if a carrier is injected in channel β with amplitude 1. For the conservation of probability density, the S matrices must be unitary.

Let us introduce generalized formula for a two-terminal conductor with multiple independent conductance channels. Let $\mathcal{T}_j$ ($j = 1, 2, 3\cdots$) be the transmission coefficient of jth channel. Then the Landauer formula provides the averaged current $\langle I \rangle$ and the conductance G as

$$\langle I \rangle = GV, \quad G = \frac{e^2}{h} \sum_j \mathcal{T}_j. \tag{2.33}$$

The low-frequency noise S is described as

$$S = \frac{e^3 |V|}{\pi\hbar} \sum_j \mathcal{T}_j (1 - \mathcal{T}_j) \tag{2.34a}$$

$$= 2e \frac{e^2}{h} |V| \sum_j \mathcal{T}_j \frac{\sum_j \mathcal{T}_j (1 - \mathcal{T}_j)}{\sum_j \mathcal{T}_j} \tag{2.34b}$$

$$= 2e \left| \langle I \rangle \right| F, \tag{2.34c}$$

where F is the Fano factor defined in Eq. (2.29). In the present case, F is given by

$$F = \frac{\sum_j \mathcal{T}_j (1 - \mathcal{T}_j)}{\sum_j \mathcal{T}_j}. \tag{2.35}$$

Equations (2.34) and (2.35) explain that the current noise is given by the sum of the noise contributions from the parallel channels, similarly to the case of $\langle I \rangle$.

The current noise at a finite temperature $T_{\rm e}$ is obtained from Eq. (2.30) as

$$S = 4k_{\rm B}T_{\rm e}G + 2e \left| \langle I \rangle \right| F \left[\coth\left(\frac{eV}{2k_{\rm B}T_{\rm e}} \right) - \frac{2k_{\rm B}T_{\rm e}}{eV} \right]. \tag{2.36}$$

The first and the second terms in the right-hand side are the thermal and shot noises, respectively.

2.5.2 Effect of incoherent scattering on shot noise correlations in the quantum Hall regime

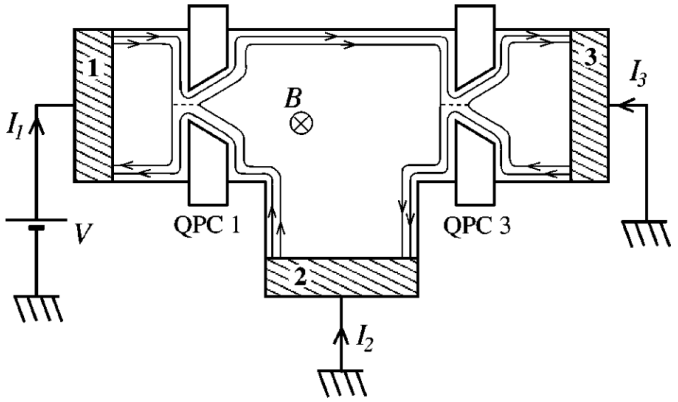

Figure 2.8: (a) Schematic diagram of setup for measuring the shot noise generated by inter-channel transmission in the region between QPC1 and QPC2 [47]. We assume the bulk filling factor $\nu = 2$, where two copropagating QHECs are formed at one edge of the 2DES. Texier and Bütikker obtained a shot-noise formula in the case that the outer channel is perfectly transmitted at both QPCs, and the inter-channel transmission between the inner channels occurs with probabilities $\mathcal{T}_1$ and $\mathcal{T}_3$ at QPC1 and QPC3, respectively.

Here we review a theory of the shot noise caused by the elastic/inelastic transmission between QHECs, which may affect the coherence of transport in QHECs. The shot noise generated by the inter-channel transmission in QHECs was theoretically studied by Texier and Bütikker[47]. Figure 2.8 shows a schematic of theoretical setup to explore the shot noise generated by inter-channel transmission. The device under consideration has three Ohmic contacts and two QPCs (QPC1 and QPC3). The bulk filling factor is set to $\nu = 2$. The electrostatic potentials of the contacts 1, 2 and 3 are set to V, 0 and 0 , respectively. The resultant currents going out through the contact 2 and 3 are I_2 and I_3, respectively. The quantity of interest is the cross-correlation of the current fluctuation $S_{23} = \langle \Delta I_2 \Delta I_3 \rangle$. They derived a shot-noise formula in the case that the outer channel is perfectly transmitted at both QPCs, and the inter-channel is partially transmitted with the transmission probability $\mathcal{T}_1$ and $\mathcal{T}_3$ at QPC1 and QPC3, respectively.

The current-current correlation function for the currents in the contact α and β is defined as

$$S_{\alpha\beta}(t-t') \equiv (1/2)\left\langle \Delta\hat{I}_\alpha(t)\Delta\hat{I}_\beta(t') + \Delta\hat{I}_\beta(t')\Delta\hat{I}_\alpha(t)\right\rangle, \tag{2.37}$$

where the current operator $\hat{I}_q(t)$ for the contact q is given as[44]

$$\hat{I}_q(t) = \frac{e}{2\pi\hbar}\sum_j \int dE dE' e^{i(E-E')t/\hbar}\left[\hat{a}^\dagger_{qj}(E)\hat{a}_{qj}(E') - \hat{b}^\dagger_{qj}(E)\hat{b}_{qj}(E')\right]. \tag{2.38}$$

Here, $\hat{a}^\dagger_{qj}$, $\hat{b}^\dagger_{qj}$ are the creation operators of electrons in incoming and outgoing waves defined by second quantization of Eq. (2.32) (definition of S matrix) for the contact q and the

channel j. Then the noise spectrum is obtained by Fourier transforming Eq. (2.37) as

$$S_{\alpha\beta}(\omega)2\pi\delta(\omega+\omega') = \left\langle \Delta\hat{I}_\alpha(\omega)\Delta\hat{I}_\beta(\omega') + \Delta\hat{I}_\beta(\omega')\Delta\hat{I}_\alpha(\omega) \right\rangle \tag{2.39}$$

with $\Delta\hat{I}_\alpha(\omega) = \hat{I}_\alpha(\omega) - \left\langle \hat{I}_\alpha(\omega) \right\rangle$. The noise is then given by

$$S_{\alpha\beta} = \frac{2e^2}{h}\int dE \sum_{\gamma,\lambda} \mathrm{Tr}\left\{ A_\alpha^{\gamma\lambda} A_\beta^{\lambda\gamma} \right\} f_\gamma(1-f_\lambda). \tag{2.40}$$

The only difference between Eqs. (2.30) and (2.40) is that the lower indices of A are different in Eq. (2.40) reflecting the cross-correlation measurement.

Let us first discuss the situation when only elastic (coherent) scattering is present in the system, which is at absolute zero. To describe coherent scattering between edge states, we introduce ϵ, which is the probability for an electron to be scattered from one edge state to the other in between the two QPCs. We need to write down the S matrix to reach from Eq. (2.40) to the correlations:

$$S_{23}^{\mathrm{c}} = -\frac{2e^2}{h}\left|eV\right| \mathcal{R}_3 \left[(1-\epsilon)^2 \mathcal{T}_3 \mathcal{T}_1^2 + \epsilon^2 \mathcal{T}_3 + \epsilon(1-\epsilon)(1-2\mathcal{R}_3\mathcal{T}_1 + \mathcal{T}_1^2) \right]. \tag{2.41}$$

In the case $\mathcal{T}_1 = \mathcal{T}_3 = 0$ ($\mathcal{R}_1 = \mathcal{R}_3 = 1$), corresponding to the setup in Sec. 2.3.2, we obtain

$$S_{23}^{\mathrm{c}} = -(2e^2/h)\left|eV\right| \epsilon(1-\epsilon). \tag{2.42}$$

This is nothing but the shot noise given by Eq. (2.34a), with $\mathcal{T} = \epsilon$ in Eq. (2.35). Thus, elastic scattering between copropagating QHECs generates the full shot noise, regardless of scattering details, such as the number of scatterers.

Next, we consider the case of inelastic (incoherent) scatterings involving phase breaking. Incoherent scattering consists of quasi-elastic and inelastic scattering, which is commonly treated by addition of a fictitious contact to the edge, where incoherent scatterings take place (see Fig. 2.9).

Here we consider the averaged Büttiker-type current, which is obtained by integrating the product of energy distribution function and the conductance as

$$\langle I_\alpha \rangle = \frac{1}{e}\int dE \sum_\beta G_{\alpha\beta}(E)\bar{f}_\beta(E), \tag{2.43}$$

where $\bar{f}_\beta$ is the averaged distribution function at contact β as we see later. The conductance part is given by

$$G_{\alpha\beta} = \frac{e^2}{h}(n_\alpha^{\mathrm{ch}}\delta_{\alpha\beta} - \mathrm{Tr}\{s_{\alpha\beta}^\dagger s_{\alpha\beta}^\dagger\}), \tag{2.44}$$

where n_α^{ch} is the number of available conductance channels at contact α. The above is the second-quantized expression of a generalized Landauer-Büttiker formula[29, 44]. The averaged current through the fictitious contact should be zero, i.e., $\langle I_4 \rangle = 0$.

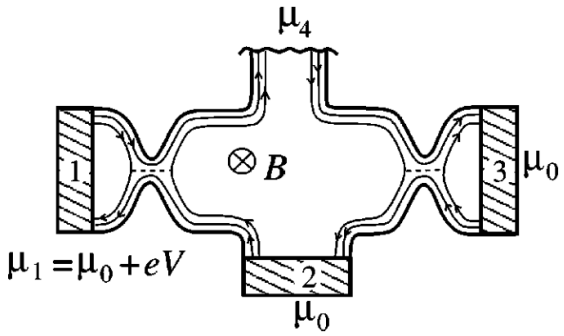

Figure 2.9: Modelization of phase breaking processes along the upper edge, to which an inelastic fictitious contact (contact 4) is attached. From Ref. [47].

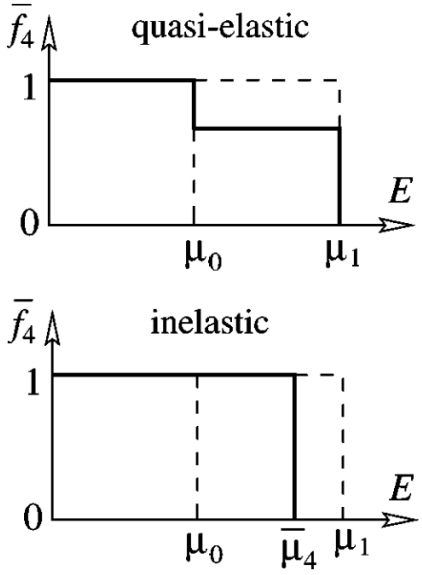

Figure 2.10: Distribution functions at the fictitious contact 4. From Ref. [47].

When the transport through the contact 4 is dominated by inelastic scatterings, the averaged distribution function at the contact 4 is in equilibrium because the electrons immediately relax at the contact 4 (the lower figure in Fig. 2.10). As in Fig. 2.9, to the contact 4, the edge states with chemical potentials $\mu_0 + eV$, $\mu_0 + eV\mathcal{T}_1$ are flowing in. Hence the averaged chemical potential at the contact 4 should be

$$\bar{\mu}_4 = \frac{1}{2}[\mu_0 + eV + \mu_0 + eV\mathcal{T}_1] = \mu_0 + \frac{1+\mathcal{T}_1}{2}eV. \tag{2.45}$$

The current at the contact α should be the sum of the Landauer-Büttiker part, which includes the fluctuations due to the intrinsic fluctuations in the contacts other than α, and the part of intrinsic fluctuation at α, δI_α, as in $I_\alpha = (1/e)\int dE \sum_\beta G_{\alpha\beta} f_\beta + \delta I_\alpha$. The current fluctuation in contact 4 is represented by the fluctuation in the chemical potential around the average (2.45). Thus $\delta I_4 = -(1/e)G_{44}(\mu_4 - \bar{\mu}_4)$. From the characteristics of the contact 4, we find that the time average of the fluctuating part $\langle \delta I_4 \rangle$ also should be zero. Then the expression of the fluctuating part of the current at contact α is obtained as

$$\Delta I_\alpha = \delta I_\alpha - \frac{G_{\alpha 4}}{G_{44}}\delta I_4. \tag{2.46}$$

The first term in the right-hand side is the intrinsic fluctuation at α and the second represents the effect of the contact 4 through the Landauer-Büttiker connection. The second term contains only the effect of the contact 4, which represents the inelastic scattering.

In the case that the scatterings at the contact 4 are quasi-elastic (the upper panel in Fig. 2.10), the situation is rather complicated. However, it is simple if we can assume that

the average of each energy-slighced element of current at the contact 4 $\langle i_4(E)\rangle = 0$, where $i_4(E)$ gives the total current as $I_4 = \int dE i_4(E)$. This means that the energy distributions flowing into the contact 4 on the edge states are simply summed up to give the distribution at the contact 4. Hence the averaged distribution function at the contact 4 is given by

$$\bar{f}_4(E) = \frac{1}{2}[(1+\mathcal{T}_1)f_1(E) + (1-\mathcal{T}_1)f_2(E)]. \tag{2.47}$$

The two distribution functions illustrated in Fig. 2.10 give the same results when they are integrated over energy. This means, on the basis of Eq. (2.43), that the two edge currents are equilibrated equally at the contact 4.

From the above discussion, we can derive the expressions of correlations (2.40) for various cases as in Ref. [47]. However, for the analysis of the experiments in this thesis, only those for $\mathcal{T}_1 = \mathcal{T}_3 = 0$ are important and here we just present them as follows. For quasi-elastic case and when $\mathcal{T}_1 = \mathcal{T}_3 = 0$, we obtain

$$S_{23}^{\rm qe} = -(e^2/h)\,|eV|\,/4, \tag{2.48}$$

which is a half of that in the case of elastic scattering in Eq. (2.42) with $\epsilon = 0.5$; that is, the Fano factor in this case is a half of the full shot noise. For the inelastic-scattering case and when $\mathcal{T}_1 = \mathcal{T}_3 = 0$, we obtain

$$S_{23}^{\rm in} = 0. \tag{2.49}$$

This means that no shot noise is generated by inelastic scattering. Equations (2.42), (2.48), and (2.49) tell us that we can distinguish the three scattering mechanism; elastic, quasielastic, and inelastic, by shot-noise measurements.

Here we note that the positive noise correlation is theoretically expected for the inelastic-scattering case with certain sets of $\mathcal{T}_1$ and $\mathcal{T}_3$, and experimentally confirmed[48]. However, normal shot noise which generates negative noise correlation as Eq. (2.42) has not been reported yet. One of the reasons is probably the technical difficulty in resolving small shot noise. It is obvious that we need to apply a finite bias V to generate the shot noise. However, when V becomes comparable to the Zeeman energy, the reconstruction of spin-resolved QHECs occurs[23, 24, 25], which may reduce shot noise. Let us estimate the required resolution for this shot-noise measurements from Eq. (2.42). The Zeeman energy is usually on the order of several hundreds of μV[23], thus we here assume that the required resolution for bias voltage is $\Delta V = 10\ \mu$V. In the case of the maximal shot-noise intensity $\epsilon = 50\ \%$, we obtain the required resolution of $\Delta S_{23}^{\rm c} = -(2e^2/h)\,|e\Delta V|\,\epsilon(1-\epsilon) \cong 1.5\times 10^{-29}\ {\rm A}^2/{\rm Hz}$. If we use the setup of the typical shot-noise measurement in Ref. [49], we need an integration time of about 35 s, which is much longer than the ordinary current measurements.

Chapter 3

Experimental

3.1 Sample fabrication

3.1.1 GaAs/AlGaAs 2DEG

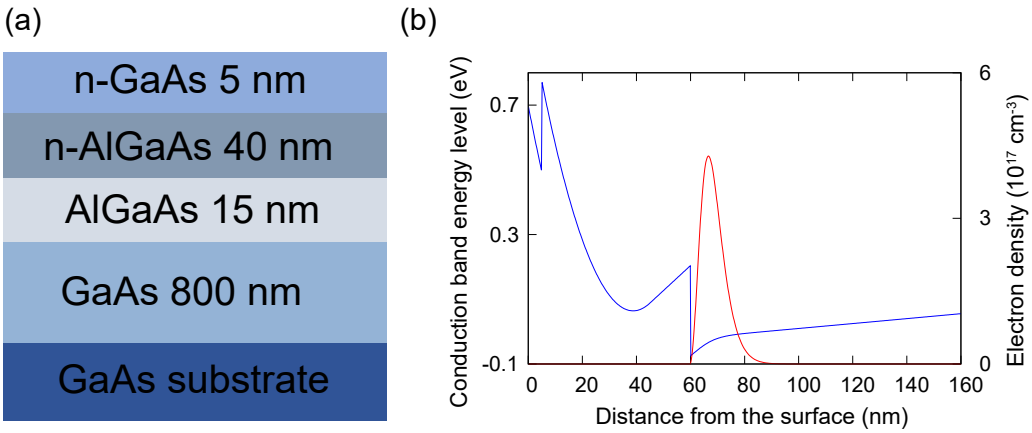

Figure 3.1: (a) Layered structure of the GaAs/AlGaAs heterostructure wafer. (b) Electron density (red line, right axis) and conduction band edge (blue line, left axis) along the direction vertical to the growth plane obtained from the self-consistent one-dimensional Schrödinger-Poisson equation.

We used the GaAs/AlGaAs heterostructures grown by depositing GaAs and AlGaAs on a GaAs(001) substrate with the molecular beam epitaxy technique in Sumitomo Electric Industries, Ltd. For the three experiments presented in Chs. 4, 5, and 7, we used three different substrates with the same layered structure and doping profile. Figure 3.1(a) shows a schematic cross section of the heterostructure. The structure of the substrate is (from the front surface) a $5\ \mathrm{nm}$ Si-doped GaAs cap layer, a $40\ \mathrm{nm}$ Si-doped ($N_{\mathrm{Si}} = 2 \times 10^{18}\ \mathrm{cm}^{-3}$) $\mathrm{Al}_x\mathrm{Ga}_{1-x}\mathrm{As}$ ($x = 0.265$) carrier-supply layer, a $15\ \mathrm{nm}$ undoped $\mathrm{Al}_x\mathrm{Ga}_{1-x}\mathrm{As}$ spacer layer, and an $800\ \mathrm{nm}$ GaAs active layer with a 2DES residing near the interface to the upper layer. We characterized the GaAs/AlGaAs substrates used in this study at the dilution refrigerator temperature (about $30\ \mathrm{mK}$). The two-dimensional electron concentration n and the mobility μ were dependent on which substrate was used, as well as on cooling

processes, but they were typically $n \cong 4 \times 10^{15}\ \mathrm{m}^{-2}$ and $\mu \cong 90\ \mathrm{m}^2/\mathrm{Vs}$, respectively.

The electrons emitted from the donors in the carrier-supply layer migrate to the GaAs active layer, so that the electrochemical potential E_{F} is spatially constant, resulting in the band bending and charge accumulation in the potential well formed near the interface. This potential well quantizes the kinetic energy along the z-direction (perpendicular to the growth surface). When the electron concentraion n is sufficiently small, and only the lowest energy level is occupied, the kinetic degree of freedom in the z-direction can be ignored. This is the formation process of a two-dimensional electron system (2DES), which we have already discussed above.

Figure 3.1(b) shows the electron density and the energy level in the conduction band in the vertical direction calculated using the self-consistent one-dimensional Schrödinger-Poisson equations (see Appendix A.1) for the present layered structure. The result shows that the peak of the electron density is located $66\ \mathrm{nm}$ below the surface.

3.1.2 Electron beam lithography

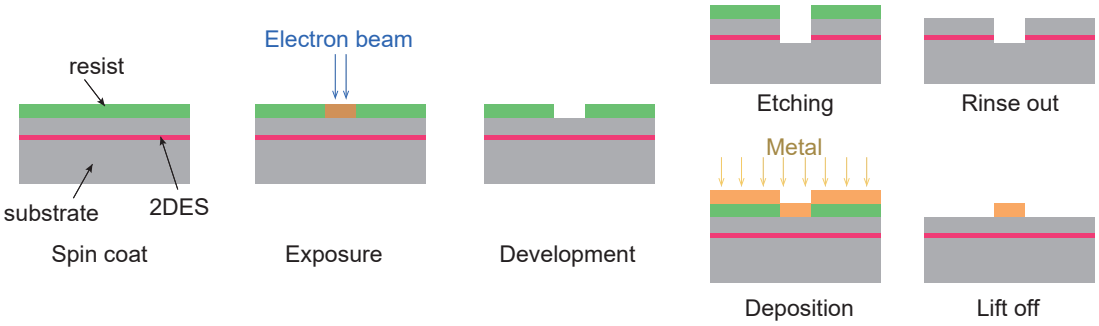

Figure 3.2: Procedure of Electron-beam lithography. After development, the process can be divided into two types; namely etching and deposition.

We used nanofabrication techniques with an electron beam (EB) lithography for the sample fabrication. We note that the samples used in Chs. 4 and 5 were fabricated by the author, using the fabrication facilities in the Institute for Solid State Physics (ISSP), the University of Tokyo. On the other hand, samples used in Chs. 6 and 7 were fabricated by technical staffs at NTT basic research laboratories (NTT brl), NTT corporation, with their facilities. Here we briefly explain the main steps of EB lithography performed by the author (see Fig. 3.2).

1. Resist coating
   After cleaning the substrate with Trichloroethylene(99.5%), acetone(99.5%), and methanol(99.8%) in an ultrasonic cleaner for 3 minutes each, we coated the chemicals called "Resists" on the substrate. Resists are photosensitive or charge sensitive polymers dissolved in solvent, and work as a mask during etching and deposition. The resist used in this study is 950 PMMA A8 (Micro Chem) diluted 50% by anisole.

PMMA (polymethyl methacrylate) is a high molecular weight polymer with quaternary carbons in its main chain, which can be easily broken, and electron beam irradiation breaks them, lowers their molecular weight and makes it more soluble in the developing solution, thus a positive type resist. The resist was coated by spin coater at $5000\ \mathrm{rpm}$ for 70 seconds. The resist was then baked at 150 °C for 30 minutes in a thermostatic oven.

2. Exposure
   An EB lithography system was used to expose the resist according to a pattern prepared in advance. The system used in our research is ELS-7700 (ELIONIX INC.), where the maximum acceleration voltage is 75 kV. In our EB lithography process, a high acceleration voltage of 75 kV was used for fine patterns, such as gates, and a low acceleration voltage of 25 kV was used for wider patterns, such as contacts and pads.

3. Development
   The exposed resist is immersed in a developing solution, called developer, to remove the areas where EB was irradiated. The developer solution is a mixture of MIBK (methyl isobutyl ketone) and IPA (Isopropanol) in a 1:3 volume ratio. After development for 60 seconds, the pattern was rinsed by IPA for 10 seconds and then by another IPA for another 20 seconds.

4. Etching
   The GaAs is dissolved in etchant. In the area where the resist remains, GaAs is not etched because the resist prevents dissolution to the etchant, and only the area without the resist is etched.

5. Deposition
   A thin metal film is deposited to coat the entire sample. In the area where the resist remains, the metal adheres to the resist surface, but in the area where there is no resist, the metal adheres to the GaAs substrate surface.

6. Lift-off/Removal of resist
   The unnecessary resist and the metal film on the resist are removed. Lift-off was performed by immersing the sample in acetone and leaving it for 30 minutes, followed by ultrasonic cleaning.

The acetone, methanol, MIBK, and IPA used in the above process were reagents of special grade from Wako Pure Chemical Industries, Ltd.

fabrication process

The actual preparation of the samples involved thin film formation and etching using the EB lithography technique described above, as well as annealing and other processes. Here we review the entire process of the actual sample preparation by the author.

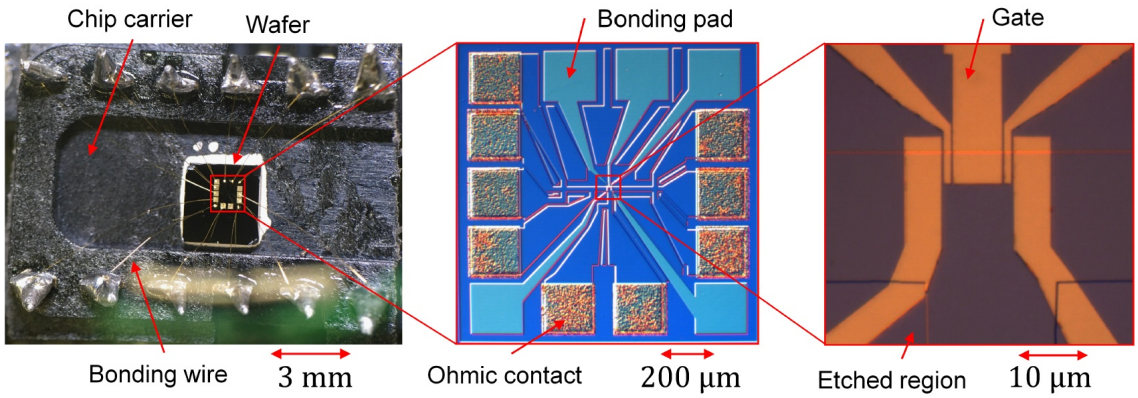

Figure 3.3: Optical micrographs of the fabricated samples. From left to right, a photo of the sample after it was mounted on a chip carrier and bonded, a general view of the sample, and a photo of the center of the sample.

1. Depletion of 2DES using wet-etching
   The wet-etching was carried out by use of the EB lithography technique. The etchant scrapes the surface of the substrate and depletes the two-dimensional electron gas underneath. The etchant was a mixture of $H_3PO_4 : H_2O_2 : H_2O = 1 : 1 : 48$. After soaking in this solution for 50 seconds, rinsing was performed by soaking in H_2O for 5 seconds and in another H_2O for 20 seconds. The etching depth was measured using a laser microscope, and it was found that the etching depth was 60 nm to 90 nm, confirming that 2DEG was removed from the etched area.

2. Making an Ohmic contact to 2DES
   With the same lithography technique, an AuGe/Ni bilayer film was deposited on the 2DES substrate using the ion beam sputtering system. A 70 nm of AuGe film was deposited, and then 7 nm of Ni was deposited on top of the substrates. The samples were annealed for alloying to get Ohmic contact to the 2DES layer. The annealing was at 430 °C for 5 minutes in a mixture of 3% H_2 and 97% N_2 atmosphere using an infrared gold image furnace MILA-3000 (Advance Science and Engineering Co., Ltd.).

3. Fabrication of gate electrodes
   The gate electrodes were fabricated by depositing an Au/Ti bilayer film using the EB lithography technique. For the sample used in Ch. 4, a 7 nm of Ti was deposited, and then 50 nm of Au (purity 99.99%) was deposited on top of the Ti using the ion beam sputtering system. The Ti layer improves the adhesion between the GaAs substrate and Au. For the sample used in Ch. 5, a 5 nm of Ti and 15 nm of Au was deposited using a electron-beam evapolation system and a resistive thermal evaporation system, respectively, for more ease of lift-off process.

4. Mounting sample to the chip carrier
   We mounted the assembled sample on a plastic chip carrier with silver paste and

bonded the electrodes using $25\ \mu\mathrm{m}\phi$ Au wire.

Photographs of a sample used in Ch. 4 are shown in Fig. 3.3 as an example.

3.2 Dilution refrigerator

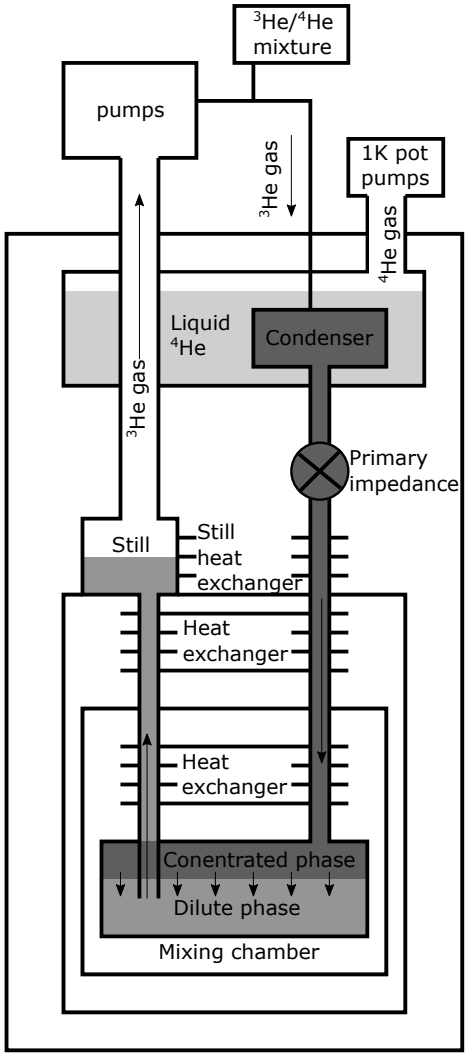

Figure 3.4: Schematic diagram of a dilution refrigerator.

The characteristic energies of quantum effects are often very small, and cryogenic temperatures are required to observe them in order to suppress thermal fluctuations. In this study, we used dilution refrigerators for all measurements. Figure 3.4 is a schematic diagram of gas and liquid He flows in a dilution refrigerator. The cooling process is briefly described below. $^3\mathrm{He}/^4\mathrm{He}$ mixed gas taken from a tank is liquefied in a 1 K pot or a Joule-Thomson valve-injection-type cooler. The mixture is once condensed in a still, where it is further cooled by the distillation of ^{3}He and sent to the mixing chamber through several

heat exchangers with the flow rate limited by the primary impedance. In the mixing chamber, the mixture separates into a dilute phase (d phase) dominated by $^4\mathrm{He}$ (about 7% $^3\mathrm{He}$) and a concentrated phase (c phase) dominated by $^3\mathrm{He}$ (almost 100% $^3\mathrm{He}$ below 0.1K). Cooling occurs during the dilution of $^3\mathrm{He}$ from the c phase to the d phase. The diluted $^3\mathrm{He}$ is then fractionated at the still and the evaporated gas is sent back to the condensation process again through several pumps. As the gas mixture is repeatedly circulated, the ratio of $^4\mathrm{He}$ gas decreases and only $^3\mathrm{He}$ gas circulates. After the system reaches a steady state, a following continuous operation with keeping the sample at a constant temperature is possible.

In this study, we used two different dilution refrigerators. For the measurements in Chs. 4 and 5, we used a top-loading-type dilution refrigerator (Kelvinox, Oxford Instruments) at ISSP, which allows the sample to be directly inserted into the $^3\mathrm{He}$ and $^4\mathrm{He}$ mixtures without stopping the circulation of the gas. The lowest attainable temperature of this dilution refrigerator was about 20 mK. A 15 T superconducting magnet is equipped to apply the magnetic field, but since the quench occurred at around 10 T we applied only up to 9 T in this study. For the measurements in Chs. 6 and 7, we used a cryo-free dilution refrigerator (Triton 200, Oxford Instruments) at NTT brl, which does not consume $^4\mathrm{He}$ for cooling and has larger experimental space. The lowest attainable temperature of this dilution refrigerator was about 40 mK. A 8 T superconducting magnet is equipped, but since the quench occurred at around 4.3 T we applied only up to 4 T in this study.

3.3 Electrical measurement

3.3.1 Lock-in measurement

In measuring the current distribution ratio as in Ch. 4, it is necessary to measure the current flowing through the two drain electrodes separately. The circuit for the measurements is shown schematically in Fig. 3.5. By using a transformer (at ISSP), or using an AC-DC mixer (at NTT brl), an AC voltage V_{AC} was superimposed on a DC voltage V_{DC}, and a voltage was applied to the sample to measure the current or local and non-local voltages. A current to a voltage transimpedance amplifier at room temperature was connected to each of the two drain electrodes of the sample, and the current flowing through each drain electrode was measured as a voltage. While the resistance of the sample is around $25\ \mathrm{k}\Omega$ in the quantum Hall region, the sum of the contact resistance, lead resistance, and the input impedance of the transimpedance amplifier was sufficiently small at around $500\ \Omega$ in the measurements in this thesis. Therefore, since most of the applied voltage is applied to the 2DES, the two drain electrodes are considered grounded during the measurement. The AC component of the voltage was measured using a lock-in amplifier synchronized with V_{AC}, and the DC component was measured using a digital multimeter. A DC voltage source was used for the gate electrode. The intruments we used are shown in table 3.1.

3.3.2 Shot-noise measurement

The techniques for the shot-noise measurement we used is described in Ch. 6.

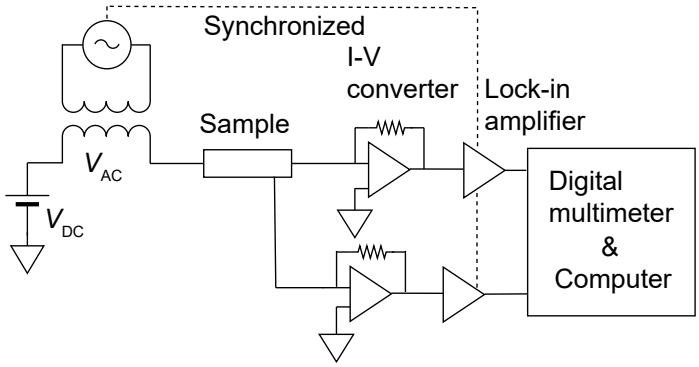

Figure 3.5: Schematic diagram of the electronic circuit used for the measurement at ISSP.

Classification	Instruments used at ISSP	Instruments used at NTT brl
Transformer	Homemade	Not used
AC-DC mixer	Not used	Homemade
Transimpedance amplifier	LI-76, NF corporation	Homemade
Lock-in amplifier	LI-575, NF corporation	SR830, Stanford Research Systems
AC voltage source	LI-575, NF corporation	WF1967, NF corporation
DC voltage source	GS200, Yokogawa Electric	Homemade
Digital multimeter	34401A, Agilent	34401A, Agilent

Table 3.1: Instruments used in this study.

Chapter 4

Gate-controlled unitary operation on flying spin qubits in quantum Hall edge states

Main contents of this chapter have been published as

- "Gate-controlled unitary operation on flying spin qubits in quantum Hall edge states" by T. Shimizu, T. Nakamura, Y. Hashimoto, A. Endo, and S. Katsumoto, Physical Review B **102**, 235302 (2020). (Editors' Suggestion)

Author contributions: T.S. designed and fabricated the sample with assistance from T.N. and Y.H.. T.S. performed measurements, analysis, and wrote the paper with assistance from S.K., T.N., and A.E.. S.K. provided supervision.

Note: A preliminal level of the study in this chapter is written in the master thesis of the author (T.S.), but the author conducted further experiments and analysis in the doctoral course.

In this chapter, we present experimental results regarding the unitary operations of FSQs in spin-polarized QHECs with only orbital control via electrostatic gate voltages. A rotation in the zenith angle of spin corresponds to inter-channel transmission between the QHECs, and the azimuth angle corresponds to the phase difference between them. Nakajima *et al.* [41, 42] preliminarily found that the transmission is triggered at the corner of QHECs, and the phase diffrence can be controled by gate voltages (see. 2.3.2). Here we present a systematic study on inter-channel transmission with spin-flip, which can be regarded as quantum-mechanical unitary operations under control.

Our findings presented in this chapter are as follows:

1. The transmission probability is affected by the curvature at the position of QHECs' corner, and can be controlled via gate voltages. The origin of the change in transmission probability by the gate voltage can be explained by the Landau-Zener-type tunneling.

2. It is possible to control the zenith and azimuth angles of spin **independently** by utilizing three independent gate electrodes.

4.1 Experimental Methods

In this section, we present experimental methods specific in the study presented in this chapter.

4.1.1 Principle

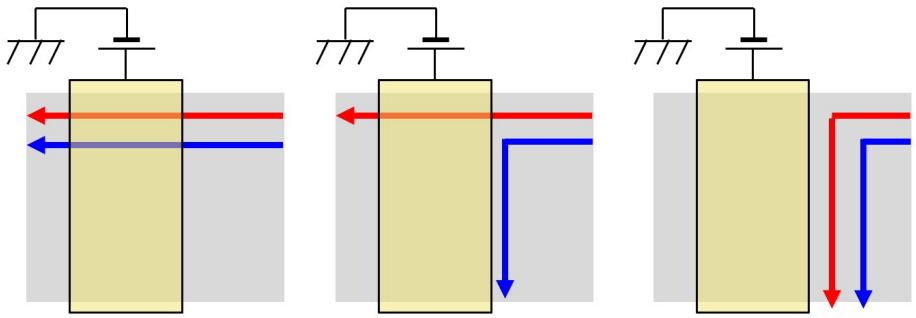

Figure 4.1: Schematic diagram of the channel manipulation by metallic Schottky gates.

First we briefly describe how to detect the coefficients a and b in Eq. (2.11) in experiment using nano-fabricated metallic gates and control of gate voltages. In our system of spin-resolved QHECs, the "spin manipulation" takes place as a transmission between two parallel edge states. However, in non-structured bulk sample, such a transmission gives no change in the eventual electrical conduction even if a and b change in Eq. (2.11). A gate electrode is thus used to discriminate between the parallel edge states and force one of them to scatter to the opposite edge, which is reflected in the electrical conduction [29, 50, 51] (also see Figs. 4.1). This is a kind of spin filter in spin space without using any magnetic material.

This technique was applied to the present study as follows. Figures 4.2(a)-(c) describe the experimental setup in three different ways. For simplicity, in the figure the filling factor ν is chosen to be 2 in the figure, although the region of $\nu = 4$ was mostly used in the present experiment. Higher filling factor adds two extra QHECs. We will go back to the effect of these two in the end of this chapter but their effect is limited.

Figure 4.2(a) is a schematic of wave-propagation paths, (b) shows the gate-electrode configuration, and (c) illustrates an enlargement of the down edges of side-gates (SL, SR) and center gate (C) along with the propagation paths in (a). The sample edges have two QHECs for $\nu = 2$, which we here denote the channels 1 and 2, in which spins are locked at $\uparrow$ and $\downarrow$, respectively. We can write their wave packets as $|1\rangle\,|\uparrow\rangle$ and $|2\rangle\,|\downarrow\rangle$, respectively, where $|1\rangle$ and $|2\rangle$ are the normalized wavefunctions of the orbital part.

We consider a wave packet emitted from the right electrode. Beneath the gates L and R, the filling factors $\nu_{\rm L}$ and $\nu_{\rm R}$ are tuned to 1[52, 53]. The incident wave packet can be written as $|1\rangle\,|\uparrow\rangle$. Channels 1 and 2 meet at the lower right corner edge of the gate SR, where a partial transmission occurs through the SOI and the angular momentum created by

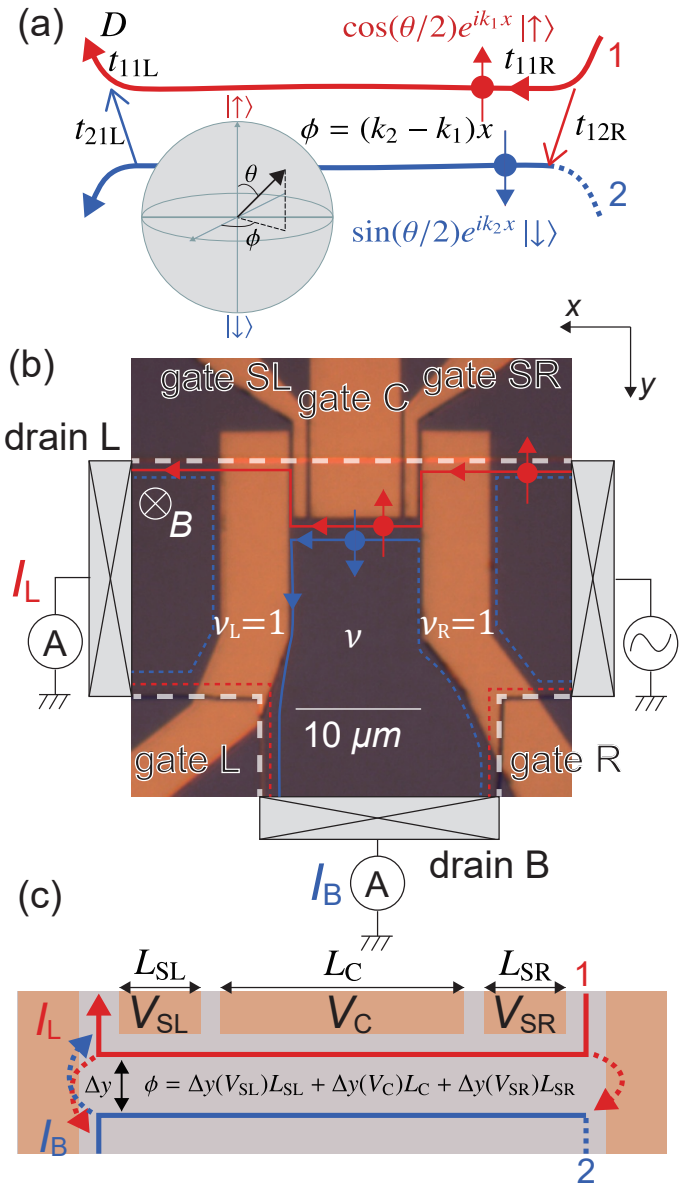

Figure 4.2: (a) Diagram of the electron spin interferometer (red and blue circles with arrows indicate spin), with an illustration of the Bloch-sphere description of an FSQ. (b) Optical micrograph of the sample with external circuits. The orange regions are metallic gates, three of which are annotated. The 2DES substrate is trimmed by etching at the white dashed lines. (c) A hybridization of (a) and (b) around the lower ends of the gate SL, C, and SR.

the QHECs running around the corner. We write the transmission process:

$$|1\rangle|\uparrow\rangle \to |\Phi\rangle_{\rm SR} = t_{11\rm R}|1\rangle|\uparrow\rangle + t_{12\rm R}|2\rangle|\downarrow\rangle\,, \tag{4.1}$$

where $t_{ij\rm R}$ are the complex transmission coefficients or the elements of S matrix defined in Eq. (2.32) and extended to the case of two channels. Naturally they satisfy the unitary condition $|t_{11\rm R}|^2+|t_{12\rm R}|^2= 1$, where we ignore the reflection coefficient because of the perfect chirality of the QHEC. The condition leads to another expression of the coefficients $t_{11\rm R} = \cos\theta/2$ and $t_{12\rm R} = e^{i\phi_0}\sin\theta/2$, where θ reflects the amplitude ratio of the partial waves and ϕ_0 is the phase difference between $t_{11\rm R}$ and $t_{12\rm R}$. Thus, $|\Phi\rangle_{\rm SR}$ is expressed as a point on the Bloch sphere as in Eq. (1.7).

In Ch. 1, we have considered that the phase of the wavefunction cannot be separated to two degrees of freedom when they are in strongly coupled regime (Eq. (1.4), (1.5)). We

now turn our attention to the phase evolution in the present case. In QHEC, the orbital part of the wave function in the single-electron picture is written as a quasi-one-dimensional plane wave in the real-space representation[54],

$$\psi_j(\boldsymbol{r}) \propto \exp(ik_j x) \exp\left[-\frac{(y-y_j)^2}{2l^2}\right], \tag{4.2a}$$

$$y_j = -l^2 k_j, \tag{4.2b}$$

where $l(=\sqrt{\hbar/eB}$ with B the magnetic field) is the magnetic length, j is the channel index counted from outer (lower energy in bulk) to inner, the x-axis is taken as along the one-dimensional channel, and y_j is the guiding center position. The wave packet $|j\rangle$ propagates on this channel of ψ_j along the down edges of the gates SR, C, and SL. At the end of the travel over the total length L, the difference in the acquired kinetic phase is

$$\phi = (k_1 - k_2)L, \tag{4.3a}$$

$$= \frac{(y_2 - y_1)L}{l^2} = 2\pi \frac{\Delta y L B}{h/e}. \tag{4.3b}$$

In the spin space, this corresponds to the azimuth-angle rotation of the spin. Here $\Delta y L B/(h/e)$ is the magnetic flux penetrating the area between the two paths measured in units of flux quantum (h/e), and thus the difference in the kinetic phase is naturally equal to the Aharonov-Bohm (AB) phase. We can thus vary ϕ using the magnetic field or the voltage applied to the gate C, which varies the distance Δy between the edge states. This single-electron picture requires correction from the screening effect, as will be discussed in the analysis sections, although the above results can still be applied to experiments with some modifications, e.g., B-dependence of Δy as given in Eq. (4.6).

At the left corner of the gate SL, the channel 1 with $\uparrow$ goes up to go beneath the region of $\nu_{\rm L} = 1$, while the channel 2 with $\downarrow$ goes down to turn around the region. Because both channels change their directions abruptly, the transmission between the two QHECs again takes place as illustrated in Figs. 4.2(a), (c). The event of transmission is considered as a short-period precession of electron spins around the effective magnetic field. Therefore the zenith angle $\theta_{\rm f}$ of the final state depends not only on the zenith angle of the traversing electron θ but also on the azimuth angle ϕ:

$$\theta_{\rm f} = \theta_{\rm f}(\theta, \phi). \tag{4.4}$$

The partition ratio is obtained as the ratio of the current through L ($I_{\rm L}$) to the total current ($I_{\rm L} + I_{\rm B}$), i.e., current distribution ratio $D \equiv I_{\rm L}/(I_{\rm L} + I_{\rm B}) = \cos^2(\theta_{\rm f}/2)$. In a simple model of the 2×2 S matrix (4×4 is reduced to 2×2 because of the chirality) described in Sec.4.3, D is written as,

$$D = C_0 + C_1 \sin\theta \cos(\phi + \Delta\varphi), \tag{4.5}$$

where $\Delta\varphi$ is the phase shift associated with inter-edge scattering at the two corners, including $-\phi_0$. Equation (4.5) is similar to the simplest Young's double-slit approximation of an AB interferometer because of the chirality or broken time-reversal symmetry of the channels and multi-terminal configuration[55]. The partition ratio of the input affects the visibility, giving the θ-dependence.

4.1.2 Quantum Hall characteristics

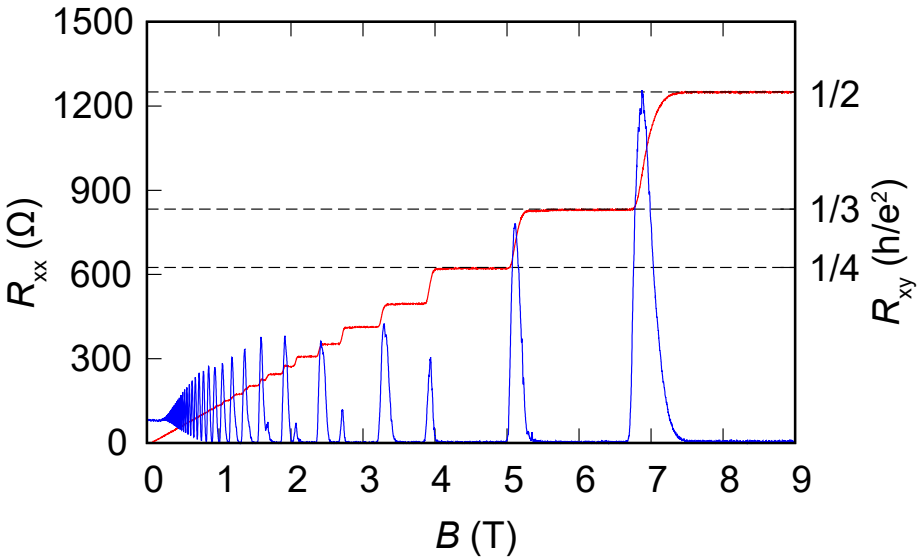

Figure 4.3: Magnetic-field dependence of R_{xx} (blue line, left axis) and R_{xy} (red line, right axis).

In this experiment, we used a GaAs/AlGaAs heterostructure presented in Sec. 3.1.1. We cooled the sample down to $20\ \mathrm{mK}$ and applied a perpendicular magnetic field B up to 9 T, at which the 2DES is in the quantum Hall state with a filling factor of $\nu = 2$. Figure 4.3 shows the Hall resistance R_{xy} and the longitudinal resistance R_{xx}. Well-developed integer QH plateaus are observed in R_{xy}, and spin separation is observed above $B \approx 2\ \mathrm{T}$ in R_{xx}.

4.1.3 Conductance versus the spin-filter gate voltages and the external magnetic fields

Figure 4.4(a) shows the color plot of the two-wire conductance plotted versus the plane of the left spin filter gate voltage (Gate L) and the magnetic field. The e^2/h plateau develops above $B = 3.3\ \mathrm{T}$ at the lower magnetic-field end of $\nu = 5$ plateau in Fig. 4.3. Figure 4.4(b) shows the pinch-off traces for Gate L at several values of B within the $\nu = 4$ plateau. We set $V_{\mathrm{L}} = -0.4\ \mathrm{V}$ for Fig. 4.8, which is within the e^2/h plateau from $B = 4.4\ \mathrm{T}$ to $5\ \mathrm{T}$. Almost the same pinch-off traces were obtained for Gate R with a small shift of $+0.01\ \mathrm{V}$, and hence we set $V_{\mathrm{R}} = -0.39\ \mathrm{V}$.

4.1.4 Measurement method

An AC voltage of typically $33\ \mu$V-rms (except for the measurements in Fig. 4.9) at $170\mathrm{Hz}$ was applied to the right-side contact, and the current was measured at drain L and drain B with a transimpedance amplifier by standard lock-in measurement (see Sec. 3.3.1). The difference of contact and cable resistance between drains L and B was less than approxi-

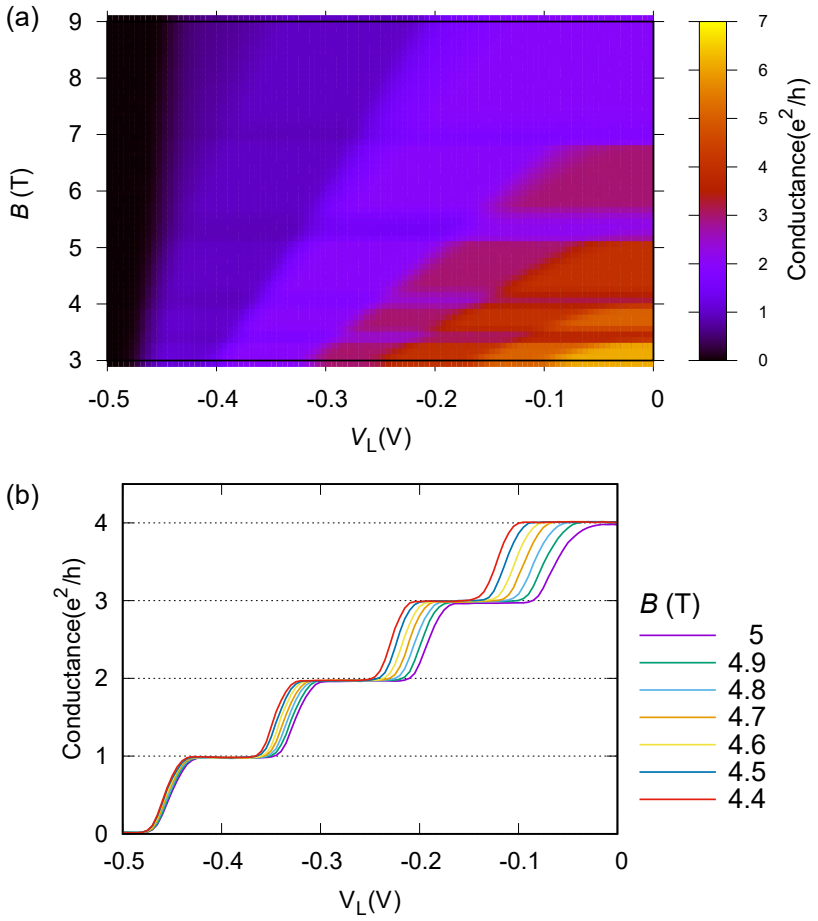

Figure 4.4: (a) 2D color plot of the two-wire conductance on the plane of the left spin filter gate voltages and the magnetic fields. Contact and lead resistance of 850 Ω is subtracted. (b) Cross sections of (a) for several values of the magnetic field. Clear conductance quantization is observed from the filling factor $\nu_{\mathrm{L}} = 1$ to $\nu_{\mathrm{L}} = 4$,

mately 2%. Therefore, D represents the transmission probability from source to drain L to a good approximation.

The voltage on gate C (V_{C}) modifies the potential gradient in the y-direction along gate C and thus the distance between neighboring edge states Δy, which leads to the modulation of ϕ[41, 42] (see Sec. 2.3.2).

4.2 Rotation in azimuth angle

Figure 4.5(a) shows the V_{C} dependence of D measured at $B = 4.75$ T, which corresponds to $\nu = 4$ in the non-gated region. The filling factors underneath gate L and gate R were kept at 1 (pinch-off conductance traces for gate L in Sec. 4.1.3). In this situation, there were two extra edge states in the interior of the 2DEG in addition to those illustrated in Fig. 4.2. In the following experiments, we assume the tunneling rate from the edge states 1 and 2 to

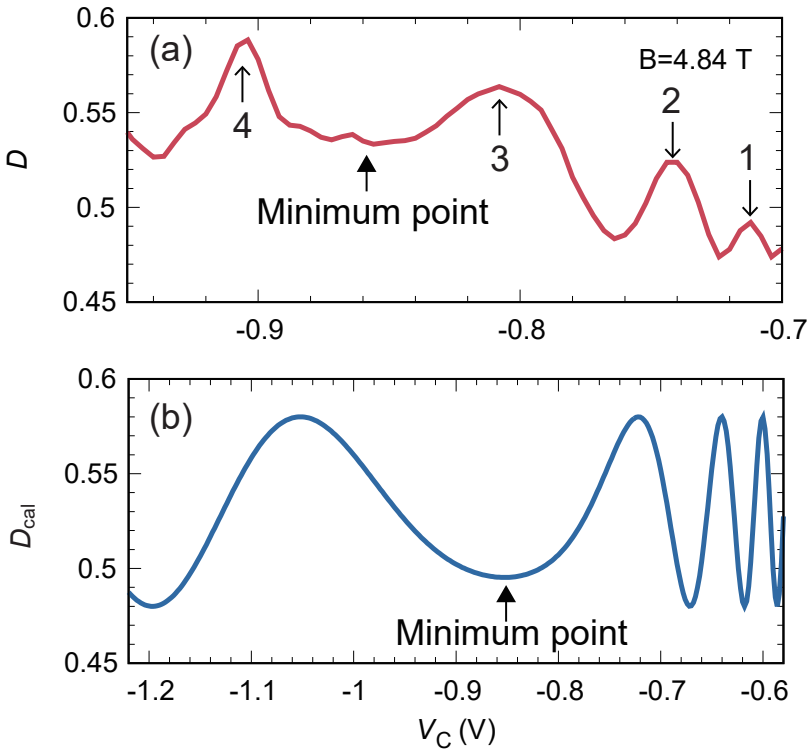

Figure 4.5: (a) $V_{\rm C}$ dependence of the current distribution ratio D at $B = 4.84$ T. Side-gate voltages were set to $V_{\rm SR} = V_{\rm SL} = -0.6$ V, where the 2DES under the gates was completely depleted. (b) Example of calculated D as a function of $V_{\rm C}$ based on the model of Eq. (4.6). We have d=66 nm from the one-dimensional Poisson-Schrödinger calculation on the layered structure of the sample [see Fig. 3.1 (b)]. Other parameters are as follows: $g = -0.6$[35]; ϵ=12.35[56]; $C_1 \sin(\theta)$=0.05, C_0=0.53, $\Delta\phi = 0$, $L_{\rm C} = 7.5$ μm; $L_{\rm SL} = L_{\rm SR} = 1.25$ μm; the offset in the gate voltage $V_{\rm C}$, $V_{\rm SL}$, and $V_{\rm SR}$ resulting from the contact built-in potential is $V_{\rm offset} = -0.05$ V. See the text for $n(y)$.

these extra states is small so that we can neglect them altogether at the precision level of the present experiment. The detailed discussion is given in Sec. 4.4. Side gate voltages were set to $V_{\rm SR} = V_{\rm SL} = -0.6$ V, where the 2DES under the gates was completely depleted. The measured D shows an oscillation with the variation of $V_{\rm C}$ in the range from -0.7 V to -0.98 V, where four peaks are observable, as indicated by arrows. The oscillation period increased for more negative $V_{\rm C}$. The region between the peaks 3 and 4 is especially wide, and the line shape shows the rewinding of oscillation. We tested several other samples having essentially the same gate configuration, and similar behavior was commonly observed.

To verify the above phase modulation scenario (or equivalent rotation in ϕ), we need to know how Δy in Eq. (4.3b) depends on $V_{\rm C}$ taking the electric screening effect into account. In the single-electron picture of Eq. (4.2), the one-dimensional channels are formed on the lines where the Landau levels cross the Fermi level. In more practical treatments in Refs. [30, 57], the QHECs are described as compressible stripes separated by incompressible insulating regions. In the compressible stripes, the electrochemical potential is kept constant by the screening effect, while the group velocity $\partial E_i/\hbar\partial k_i$ is finite. There-

fore, Eq. (4.2b) does not hold inside the stripes and the wavenumber k_j should also be kept constant. In other words, Eq. (4.2b) only holds inside the incompressible regions. As the value of Δy, we should thus take the width of the incompressible stripes, which is generally much narrower than that of the compressible ones. In Refs. [30, 57], such Δy is explicitly given for a simple classical electrostatic model of the QHEC as

$$\Delta y \approx \sqrt{\frac{8|\Delta E|\epsilon\epsilon_0}{\pi e^2 (dn/dy)|_{y=y'_i}}}\,, \tag{4.6}$$

where y'_i is the position of the ith incompressible liquid strip, $\epsilon\epsilon_0$ is the dielectric permittivity of the matrix semiconductor, $n(y)$ is the electron sheet density profile, and ΔE is the energy difference between the levels of channels i and $i+1$. The model has been used in analyzing many experimental works[58, 59, 60]. The energy difference ΔE in the present case ($i = 1$) of exchange-aided Zeeman splitting can be written as $g\mu_{\rm B}B$, where g is the exchange-enhanced Landé g-factor, and $\mu_{\rm B}$ is the Bohr magneton.

Figure 4.5(b) shows an example of the $V_{\rm C}$ dependence of D, calculated from Eq. (4.6) with the parameters noted in the caption. These parameters are chosen to preserve semi-quantitative consistency with the analysis of the magnetic response described later. To calculate $n(y)$ as a function of $V_{\rm C}$, we employ the "frozen surface" model and the self-consistent Thomas-Fermi approximation given in Ref. [57] (see Appendix B.3.2). Then, $(dn/dy)|_{y=y'_1}$ can be obtained numerically from $n(y)$. The characteristic behavior of the oscillation in Fig. 4.5(a) is qualitatively reproduced, in that the oscillation phase advances more rapidly with the decrease of $V_{\rm C}$ at lower $|V_{\rm C}|$. The progress in the phase slows down, and the rewinding of the oscillation with increasing $|V_{\rm C}|$ begins at the point indicated in the figure as "Minimum point." This behavior is qualitatively explained as follows. (see Fig. 4.6). At low $V_{\rm C}$, the edge of the 2DES lies near the end of the center gate, and the electrostatic confinement potential at the edge is soft, leading to small $(dn/dy)|_{y=y'_1}$ and large Δy. With more negative $V_{\rm C}$, the potential becomes steeper, lowering Δy. A further increase in the negative $V_{\rm C}$ causes softening of the potential and an increase in Δy again. Because Δy must be smooth as a function of $V_{\rm C}$, $|d(\Delta y)/dV_{\rm C}|$ decreases with decreasing $V_{\rm C}$, letting the oscillation period become slower, until reaching "Minimum point", roughly corresponding to the steepest edge-confinement potential (maximum in $(dn/dy)|_{y=y'_1}$), and again increases with negative $V_{\rm C}$, resulting in the rewinding of the oscillation in D.

In spite of the apparent resemblance between Figs. 4.5(a) and (b), quantitative fitting that is consistent with a response to the magnetic field is difficult. We also investigated the "Fermi-level pinning" model for the surface states, and found that it did not improve the quantitative agreement. The discrepancy suggests the necessity to take into account the effects not considered so far, e.g., the geometrical effect of the gate electrode, that cannot be characterized by microscopes. As illustrated in Fig. 4.6, the gate C is working in a critical region and some fluctuation in the metal-to-semiconductor contact condition may result in large windings in the edge line. We believe, however, that the close resemblance between Figs. 4.5(a) and (b) indicates the essential correctness of the scenario.

As in Eq. (4.3b), the azimuth angle rotation is locked to the AB phase acquired from the magnetic flux piercing the incompressible regions. This can be readily confirmed by the oscillatory behavior of D versus B, as shown in Fig. 4.7(a) with $V_{\rm C}$ as a parameter.

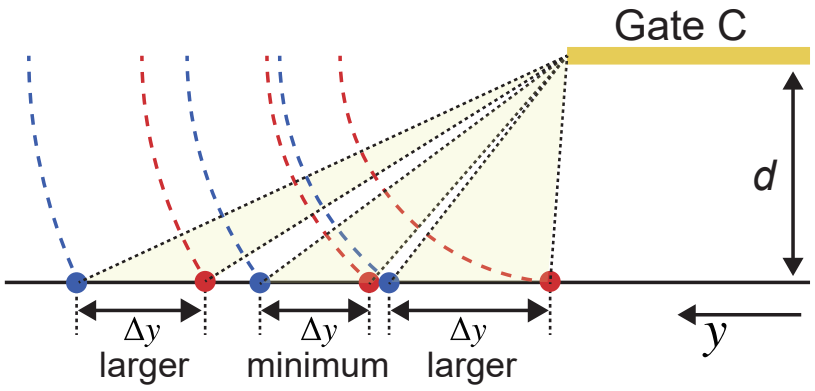

Figure 4.6: Variation of the equipotential lines for different $V_{\rm C}$. For simplicity, we consider only the electrostatic potential generated by Gate C. Red and blue broken lines represent the electrostatic equipotential line of the channels 1 and 2, respectively.

Because a single period ΔB of the oscillation corresponds to 2π rotation in ϕ, Δy is given as $\Delta y = (2/3)(h/e)/L\Delta B$ from Eq. (4.3b) in the local linear approximation of the B-dependence of Δy in (4.6), where $\Delta E = g\mu_{\rm B}B$. The derivation of this equation is as follows. For the variation of ΔB in B, the relation

$$\frac{2\pi L}{h/e}\{\Delta y(B+\Delta B)(B+\Delta B) - \Delta y(B)\} = 2\pi \tag{4.7}$$

holds. Let us write Eq. (4.6) as $\Delta y(B) \approx A\sqrt{B}$, where $A = \sqrt{(8|g\mu_B|\epsilon\epsilon_0)/(\pi e^2 (dn/dy)|_{y=y_i})}$. The B-dependence of $(dn/dy)|_{y=y_i}$ is negligibly small within the span of ΔB, and thus we can treat A as a constant independent of B. The Eq. (4.7) becomes

$$A\sqrt{B+\Delta B}(B+\Delta B) - A\sqrt{B}B = \frac{h/e}{L}, \tag{4.8}$$

$$\frac{h/e}{LA} = (B+\Delta B)^{\frac{3}{2}} - B^{\frac{3}{2}} \approx \frac{3}{2}\sqrt{B}\Delta B \tag{4.9}$$

Then we reach, to the lowest order in $\Delta B/B$ ($\ll 1$),

$$\Delta y \approx \frac{2}{3}\frac{h/e}{L\Delta B}. \tag{4.10}$$

This gives Δy as a function of B, as shown in Fig. 4.7(b) for $V_{\rm C}$=−0.86 V. The obtained values of Δy (1 to 3 nm) are much shorter than the magnetic length l=11 nm at B=5 T, which is consistent with the view of compressible/incompressible stripes, while the predicted B-dependence of Δy for constant g and (dn/dy), calculated with

$$\Delta y \approx \sqrt{\frac{8|g\mu_B B|\epsilon\epsilon_0}{\pi e^2 (dn/dy)|_{y=y_i'}}} \tag{4.11}$$

deviates from the experiment, as indicated by Fig. 4.7(b).

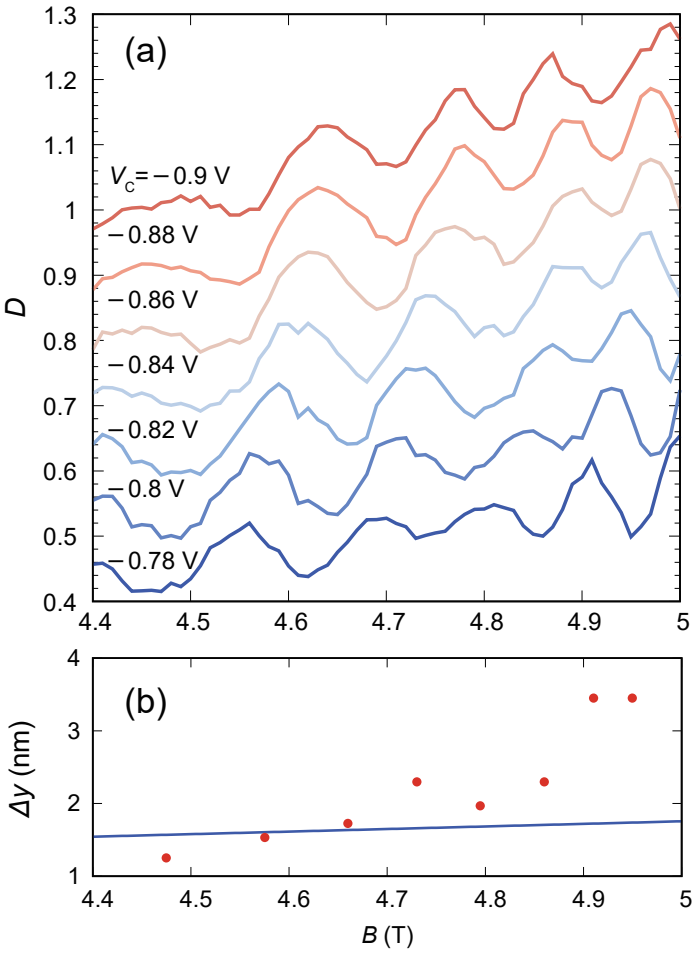

Figure 4.7: (a) Current distribution ratio D as a function of B within the plateau regime encompassing the filling factor $\nu = 4$ for several values of gate C voltage $V_{\rm C}$ (Traces are offset for clarity). $V_{\rm ac} = 32.8\ \mu{\rm V}_{\rm rms}$. (b) Δy calculated from the equation $\Delta y = (2/3)(h/e)/L\Delta B$ for $V_{\rm C}$=−0.86 V. ΔB is given by twice the distance between the adjacent oscillation peak and dip. The blue line indicates $\Delta y_{\rm average} = (\Delta y(V_{\rm SL})L_{\rm SL} + \Delta y(V_{\rm C})L_{\rm C} + \Delta y(V_{\rm SR})L_{\rm SR})/(L_{\rm SL} + L_{\rm C} + L_{\rm SR})$ from Eq. (4.11) with the parameters used in Fig. 4.5(b).

To visualize the overall trend, the measured and calculated values of D are color plotted on B-$V_{\rm C}$ in Figs.4.8(a) and (b), respectively. The oscillation patterns appear as curved stripes in these plots. Such curving behavior is consistent with the interpretation of Fig. 4.5 as follows. With the decrease of $V_{\rm C}$ from -0.7 V to approximately -0.8 V for a fixed B, $(dn/dy)|_{y=y_1'}$ increases and therefore ϕ decreases, resulting in the upward shifts of the ridges. After reaching the maximum at $V_{\rm C} \approx -0.86$ V, $(dn/dy)|_{y=y_1'}$ declines with further decrease in $V_{\rm C}$.

The observation of arc-like curving strongly supports the legitimacy of the analysis so far. Similar arch-like curves were also observed at the filling factors $\nu = 2$ and 3, albeit with smaller visibility. At smaller filling factors, B and hence Δy are larger, making θ, the zenith angle, smaller, as will be discussed later. Regarding the visibility in Fig. 4.5, the oscillation is visible in the range of $V_{\rm C}$ from -0.7 to -1 V, and the visibility is highest

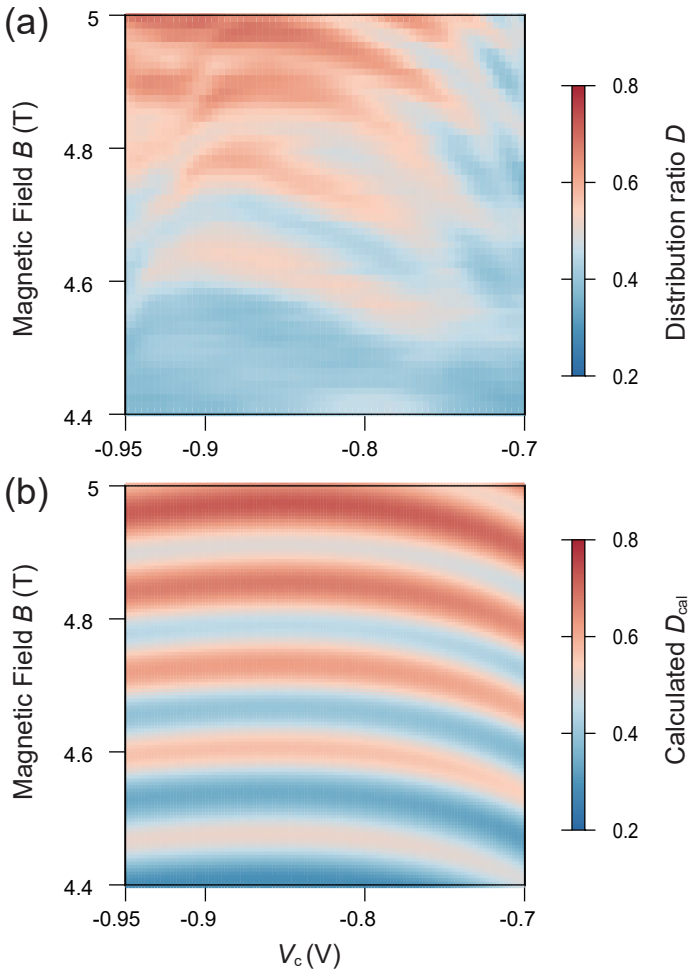

Figure 4.8: (a) Color plot of the measured D as a function of B and V_{C}. $V_{\mathrm{SR}} = V_{\mathrm{SL}} = -0.6\,\mathrm{V}$. (b) Color plot of the theoretically calculated D as a function of B and V_{C}. $C_0 = 0.42B - 1.45$ and $C_1 \sin(\theta) = 0.1$ are used. The other parameters are the same as those in Fig. 4.5 (b).

around the "Minimum point." This trend is common in the magnetic-field range shown in Fig. 4.8, and the visibility does not vary much with B. The role of the increase in B here is simply to enhance the rotation of ϕ, without causing dephasing. A possible explanation for the variation of the visibility with V_{C} is as follows: we speculate that the simple model in Fig. 4.2(c) is approximately realized only around the steepest edge-potential condition. When the edge potential is soft, the QHECs have more chances to experience the effect of local potential disorder. As a result, the effective edge line fluctuates spatially, creating local orbital angular momentum, which causes inter-edge state scattering[61]. Therefore, we obtain the highest visibility when the edge confining potential is steepest, and the visibility degrades away from this condition.

From the above results and analysis, we can safely say that the current partition ratio D reflects the azimuth-angle rotation of FSQ traveling along the edges of the gates. The rotation angle can be tuned by the center gate voltage electrostatically.

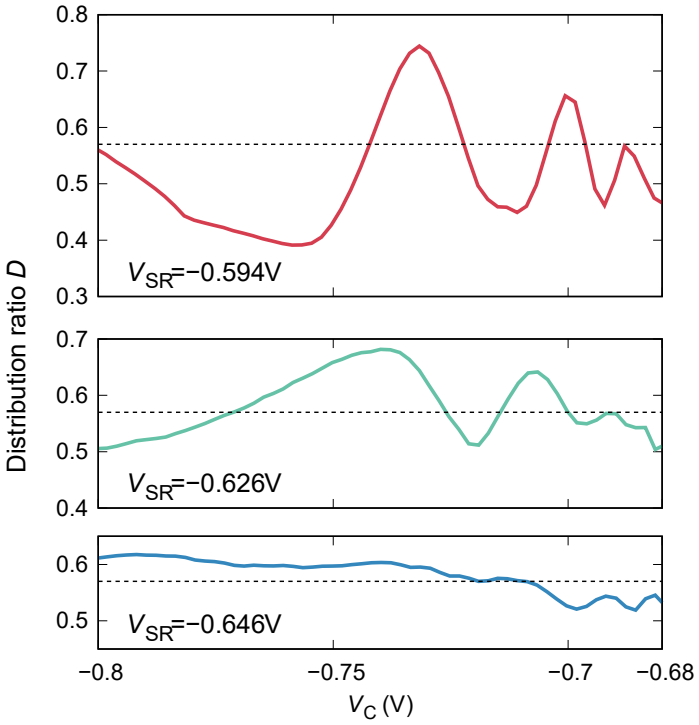

Figure 4.9: Three oscillation patterns corresponding to three different values of $V_{\rm SR}$. $B = 4.5$ T and $V_{\rm SL} = -0.605$ V. $V_{\rm ac} = 23.8$ μV. The line for $D = 0.57$ is indicated by broken lines to show that the oscillation baseline basically remains unaltered by changing $V_{\rm SL}$.

4.3 Rotation in zenith angle

In Fig. 4.9, we compare the oscillation patterns for three representative values of $V_{\rm SR}$, which strongly affects the oscillation amplitude. From $V_{\rm SR} = -0.594$ V the amplitude gradually decreases with the decrease in $V_{\rm SR}$. The characteristic features of the oscillation versus $V_{\rm C}$ observed so far do not change with $V_{\rm SR}$, other than a phase shift, which is probably caused by a change in ϕ_0. In the region $V_{\rm SR} > -0.594$ V (not shown), by contrast, the oscillation pattern varied drastically following the slight change in $V_{\rm SR}$. This is probably because the channel 2 starts to intrude into the spatial gap between the gates SR and R [see Fig. 4.2 (b)]. Hence, this region is excluded from the present discussion.

We discuss the origin of the variations in the amplitude represented by the zenith angle θ. The angle θ is determined when the wave packet turns the down-right corner of the gate SR. At the turning point, the time-dependent local Hamiltonian should contain SOI terms: one from the in-plane potential gradient[62], the other from the Rashba and Dresselhaus effects commonly observed in 2DES[39]. In the present case of spin-polarized QHEC, the former affects the effective Zeeman energy by the spin-orbit effective field, while the latter kinematically rotates the spin. Figure 4.10(a) illustrates the time evolution of quasieigenenergies for spin down and up wavepackets, *i.e.*, $E_\uparrow = \langle\uparrow| \langle 1| H_{\rm loc}(t) |1\rangle |\uparrow\rangle$ and $E_\downarrow = \langle\downarrow| \langle 1| H_{\rm loc}(t) |1\rangle |\downarrow\rangle$, while the wave packet is turning at the corner. Around the center of the corner region, $E = E_\downarrow - E_\uparrow$ takes the minimum value $E_{\rm min}$.

The transition in Eq. (4.1) can then be taken as partially non-adiabatic tunneling. By

summarizing these effective time-localized SOIs as $H_{\mathrm{SOI}}(t)$, we obtain the probability P of the inter-edge-channel transition by slightly modifying a Landau-Zener-type formula[63] as

$$P \propto |\langle\uparrow|\langle 1|\, H_{\mathrm{SOI}}\, |2\rangle\, |\downarrow\rangle\, |^2 \exp\left[-2\pi \frac{(E_{\mathrm{min}}/2)^2}{\hbar(dE/dt)}\right], \tag{4.12}$$

where dE/dt is the slew rate of E. As indicated by the arrows in Fig. 4.10(b), the total process from $|1\rangle\,|\uparrow\rangle$ to $|2\rangle\,|\downarrow\rangle$ consists of a non-adiabatic transition from $|1\rangle\,|\uparrow\rangle$ to $|1\rangle\,|\downarrow\rangle$ and an adiabatic transition from $|1\rangle\,|\downarrow\rangle$ to $|2\rangle\,|\downarrow\rangle$. The expression in (4.12) indicates that the slew rate and the minimum energy difference strongly affect the transition probability.

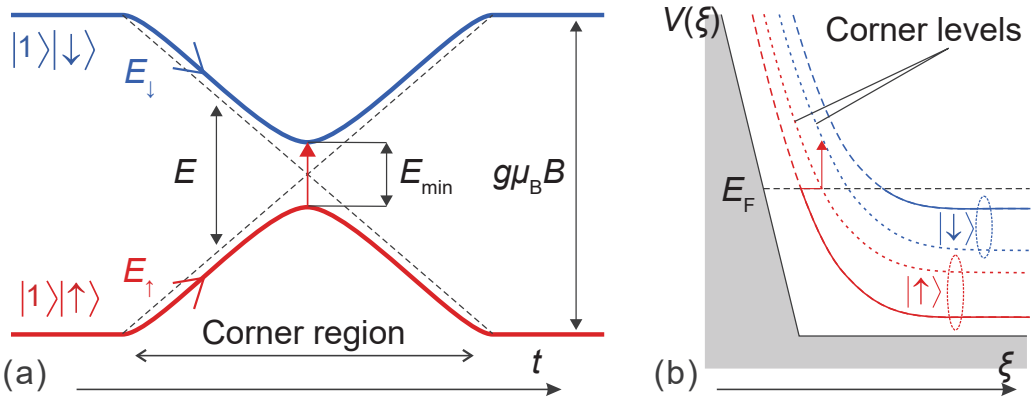

Figure 4.10: (a) Schematic time evolution of quasi-eigenenergies $E_\uparrow = \langle\uparrow|\langle 1|\, H_{\mathrm{loc}}(t)\, |1\rangle\, |\uparrow\rangle$ and $E_\downarrow = \langle\downarrow|\langle 1|\, H_{\mathrm{loc}}(t)\, |1\rangle\, |\downarrow\rangle$. (b) Illustration of spin-polarized edge states for a straight edge (solid and broken lines) and a corner (dotted lines). Here, ξ represents the distance from an edge of infinite potential ($V(0) = \infty$). For simplicity, the Landau levels are drawn in the single-electron picture.

A simple explanation for the suppression of oscillation amplitude shown in Fig. 4.9 follows from Eq. (4.12) and the electrostatic model in Refs. [30, 57]. With more negative V_{SR}, QHECs move away from the "steepest potential" point, where the distance between the outer and the inner edges is the minimum and the curvature radius r_{t} also is the shortest. As r_{t} decreases, dE/dt increases because of the shorter interaction time, and the potential gradient is larger; thus, E_{min} is smaller. From Eq. (4.12), we find that the transition probability P is the maximum for the steepest edge potential condition. As in Fig. 4.9, this scenario tells us that the steepest-potential condition should correspond to $V_{\mathrm{SR}} > -0.594$ V, which is considerably smaller than -0.8 V for V_{C}. This difference may come from the geometrical complexity in the real gate configuration which change the equipotential lines around the corner intricately, and the maximum of P may appear at smaller V_{SR} than the value at the steepest potential.

For the qualitative discussion on the change of the edge channel shape for the side gate voltages, we carried out a numerical calculation using the semiconductor module of commercial program COMSOL Multiphysics [64]. The detail of this calculation is shown in Appendix A.2. Figure 4.11 shows the electron density at a depth of 64 nm (the peak position of the calculated electron density by COMSOL) from the surface in gray scale. Channel 1 is expelled from Gate SR as the negative voltage is applied, and the radius of

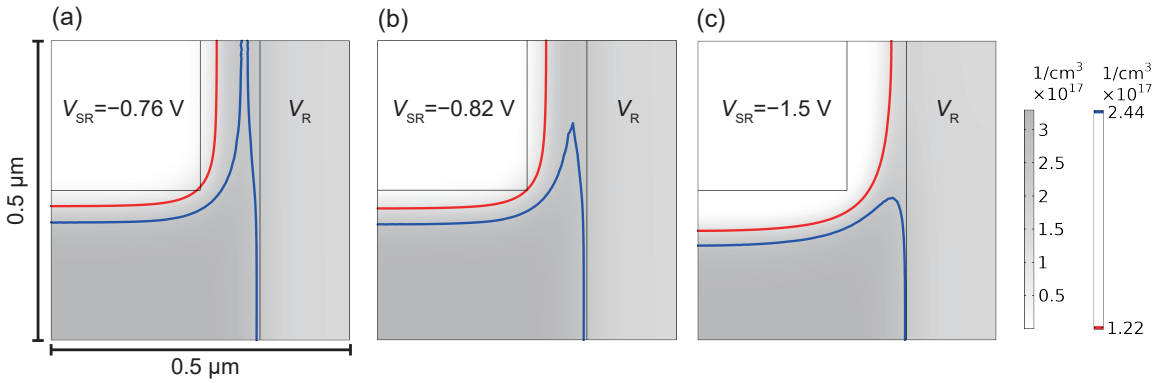

Figure 4.11: Grayscale plots of the calculated electron density at a depth of 64 nm from the surface, obtained by the finite-element method, density-gradient theory for various gate voltages $V_{\rm SR}$. The equipotential lines corresponding to the first and second compressible strips from the edge of the 2DES at the bulk filling factor $\nu = 2.5$ are plotted as red and blue lines, indicating the position of the channels 1 and 2, respectively. We set $V_{\rm R} = -0.2$ V in this simulation. (a) The plot for $V_{\rm SR} = -0.76$ V. (b) The plot for $V_{\rm SR} = -0.82$ V. (c) The plot for $V_{\rm SR} = -1.5$ V.

gyration r_t becomes large. At the same time, the channel 2 is driven out from the gapped region between Gate SR and Gate R. This leads to the drastic change of the closest point between the outer and the inner edge channel, where the transition takes place. This may also affect the non-adiabatic transition probability.

From the oscillation data in Fig. 4.9, we can estimate the zenith angle θ as follows, assuming that the dephasing is ignorable at the largest amplitude region in $V_{\rm C}$. The analysis yields the lower limit of θ in the case with non-negligible dephasing. Let $t_{ij{\rm L}}$ be the complex transmission coefficients of the processes $|i\rangle \to |j\rangle$ at the bottom left corner of the gate SL; then, from Eq. (4.1), the wave packet state that turns the corner, enters channel 1, and go to drain L is written as

$$|\Phi\rangle_{\rm L} = \left(t_{11{\rm R}} e^{ik_1 L} t_{11{\rm L}} + t_{12{\rm R}} e^{ik_2 L} t_{21{\rm L}}\right) |1\rangle\, |\uparrow\rangle\,.$$

For simplicity, we write the complex transmission coefficients in the modulus-argument form as $t_{11{\rm R}} t_{11{\rm L}} = t_1 \cos(\theta/2) e^{i\varphi_1}$ and $t_{12{\rm R}} t_{21{\rm L}} = t_2 \sin(\theta/2) e^{i\varphi_2}$. This leads to the simple Young's double-slit result of the transmission coefficient $T_{\rm L} = \langle\Phi|\Phi\rangle_{\rm L}$ as

$$T_{\rm L} = t_1^2 \cos^2(\theta/2) + t_2^2 \sin^2(\theta/2) + t_1 t_2 \sin\theta \cos(\phi + \Delta\varphi). \tag{4.13}$$

From the comparison with Eq. (4.5),

$$C_0 = t_1^2 + (t_2^2 - t_1^2)\sin^2(\theta/2), \quad C_1 = t_1 t_2. \tag{4.14}$$

In Fig. 4.9, the baseline of oscillation C_0 remains almost unchanged, while $C_1 \sin\theta$ varies widely. This can be explained based on Eq. (4.14), assuming that t_1 and t_2 happen to be close to each other: $t_1 \approx t_2$, in the present condition (the best visibility condition). Then, $C_0 \approx t_1^2 \approx C_1 \approx 0.57$. In Fig. 4.9, the largest amplitude gives $C_1 \sin\theta$ as 0.17,

which corresponds to $\theta \approx 17.4°$. This represents the lower bound of θ. Considering the inevitable dephasing, the value of θ is expected to be larger. To estimate θ more precisely, the oscillation of $C_1 \sin\theta$ should be observed. Unfortunately, the maximum value of θ obtained in the present study is less than 90°, making further analysis difficult. For more precise control of FSQ in the present scheme, the corner gates should be designed to create a sharper corner potential. Furthermore, the dephasing should be reduced, *e.g.*, by soft separation of the edges with an extra gate.

4.4 Effects of inner edge channels in $\nu = 4$ quantum Hall state

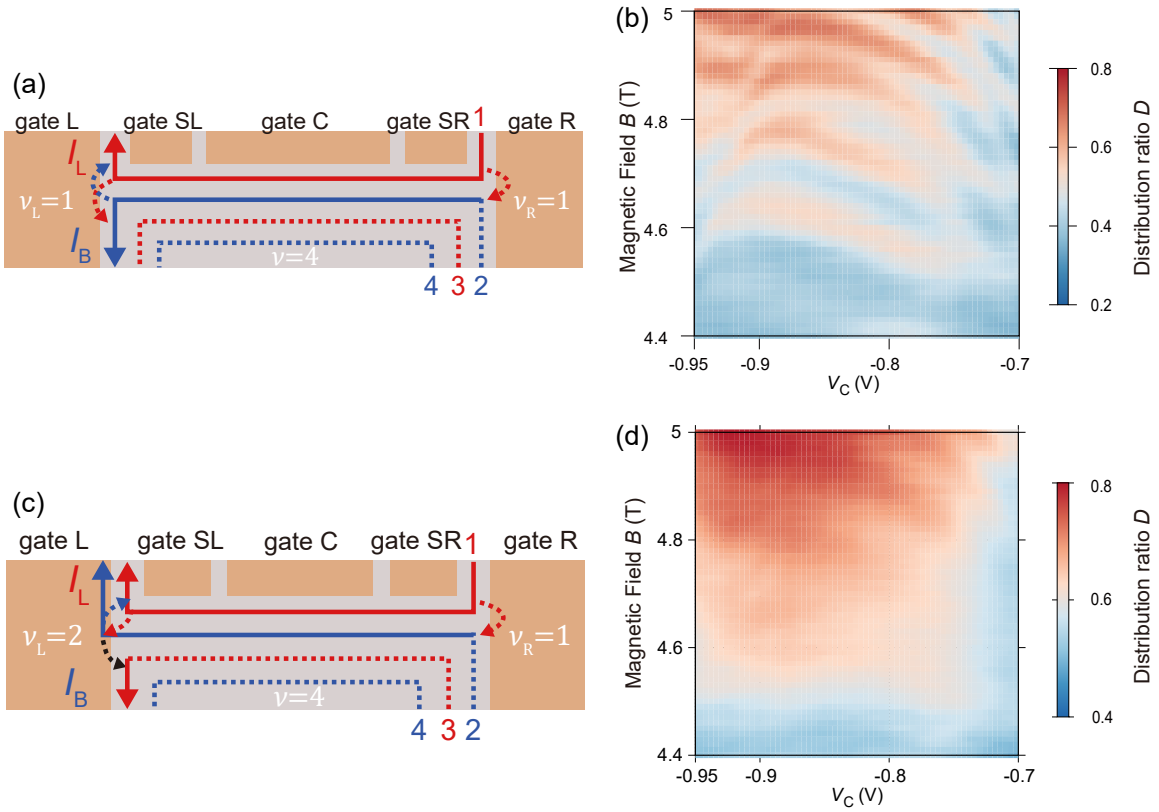

Figure 4.12: (a) Schematic of the QHECs configuration in $\nu = 4$ quantum Hall state with $\nu_R = 1$ and $\nu_L = 1$. (b) Color plot of the measured D as a function of B and V_C with $\nu_R = 1$ and $\nu_L = 1$. The same as Fig. 4.8 (a). (c) Schematic of the QHECs configuration in $\nu = 4$ quantum Hall state with $\nu_R = 1$ and $\nu_L = 2$. (d) Color plot of the measured D as a function of B and V_C with $\nu_R = 1$ and $\nu_L = 2$. $V_L = -0.28$ V, $V_R = -0.39$ V, and $V_{SR} = V_{SL} = -0.6$ V.

In the description of unitary operations in Sec. 4.1.1, the filling factor ν is chosen to 2, but $\nu = 4$ was mostly chosen in the experiments. Hence in the actual situation, the edge

states with the channel indices i=3, 4 are running in the interior of the 2DES as illustrated in Fig. 4.12(a). The condition $\nu = 4$ was chosen for the visibility of the oscillation in the current distribution to be maximized. We observed similar oscillations at $\nu = 2$ with smaller visibilities, which means that the zenith angle θ large enough for the observation was not attainable even for the steepest-potential condition for $\nu = 2$. This indicates that the tunneling between the edge channels depends delicately on quantities, such as the potential shape, the distance between the channels, etc. The other samples made from the same 2DEG substrate showed basically the same tendency.

Now we discuss the situation of $\nu = 4$. The channels with $i = 3, 4$ may affect the unitary operations through the tunneling from the channel 1 to the channel 3 and channel 4 at the right corner in Figure 4.12(a) because the input state is initialized 100% to the channel 1. However, we infer that this probability is small. The spatial distance between the channel 1 and 3 is large because: a) the distance is the sum of that from the channel 1 to 2 and that from 2 to 3; b) the distance from 2 to 3 (let us write d_{23}) is larger than that from 1 to 2 (d_{12}). b) is easily guessed from Eq. (4.6). First, ΔE is the Landau-level separation for d_{23} while ΔE is the Zeeman splitting for d_{12}. In the present case, the former is larger. In Eq. (4.6), dn/dy in the denominator is also smaller for d_{23}. Figure 4.7 (b) shows that the values of d_{12} ranges from 1 to 3 nm while Eq. (4.6) with $\Delta E \approx \hbar\omega_c$ gives 18 nm for d_{23} (with the parameters of $B = 4.7$ T, $V_{\rm C} = -0.86$ V), confirming the relation $d_{12} \ll d_{23}$. Therefore the tunneling from the channels 1 to 3 at the right corner is negligible at the precision level of the present experiment.

This has also been confirmed in the experiment shown in Fig. 4.12 (c), (d), in which channel 2 was allocated to the path going upward at the left corner. As in Fig. 4.12 (d), the interference pattern observed in Fig. 4.12 (b) disappeared. If some portion of electron wavepacket on channel 1 tunnels into channel 3 at the right corner, the re-partitioning at the left corner should be affected by the interference, and we should see some interference pattern. Therefore this result also confirms that the tunneling from the channels 1 to 3 at the right corner is negligible in the present experimental condition. At the same time, this result also tells that a significant amount of the wave packet is allocated downward at the left corner due to the difference in the potential landscape (the black arrow in the figure). If a similar phenomenon occurs in the situation of Fig. 4.12(a), this would add an artificial constant to the experimentally estimated θ. This possibility can be eliminated, if we were able to observe the oscillation of the visibility with the gate voltage $V_{\rm SR}$ as mentioned above.

The observation is through the current distribution ratio D. At present the experiment cannot give precise functional form of $\theta_{\rm f}$ in Eq. (4.4). We have not reached the complete final answer though the progresses will be given in the following chapters.

4.5 Conclusion

We have studied the unitary operation of FSQs in QHECs with electric voltages on metallic gates. This operation utilized the strong coupling between spin and edge channel orbitals. The spin rotation in the azimuth angle with voltage and with a magnetic field was systematically studied. A characteristic feature for spin appeared in the rotation in the zenith angle,

for which a new type of SOI at a corner of the edge channel was introduced and controlled with the gate voltage. With the combination of these two techniques, all-electrical control of electron spin at spin-resolved quantum Hall edge states was achieved though we still have several open questions.

Chapter 5

Half-mirror on spin-resolved QHECs

本章については、５年以内に雑誌等で刊行予定のため、非公開。

Chapter 6

Homemade-HEMT-based transimpedance amplifier for high-resolution shot-noise measurements

Main contents of this chapter have been published as

- "Homemade-HEMT-based transimpedance amplifier for high-resolution shot noise measurements" by T. Shimizu, M. Hashisaka, H. Bohuslavkyi, T. Akiho, N. Kumada, S. Katsumoto, and K. Muraki" Review of Scientific Instruments **92**, 124712 (2021). (Editor's Pick)

Author contributions: T.S. and H.B. repeated the development cycle of fabrication and evaluation of homemade transimpedance amplifiers (TAs). M.H. and T.S. and H.B. designed the circuit of the TAs. T.S. performed shot-noise measurements and analysis with assistance from M.H.. M.H. designed the measurement setup of dilution refrigerator, and T.S. and H.B. prepared wiring and placing of the TAs. T.A. fabricated AlGaAs/GaAs heterostructure for HEMTs. T.S. wrote the paper with assistance from M.H.. The QPC device was fabricated by H. Murofushi and S. Sasaki at NTT Basic Research Laboratories, NTT corporation. K.M. and S.K. provided supervision.

It is known that the shot-noise measurement is a powerful technique to reveal decoherence processes during transport, especially those caused by inelastic transmission, which reduces shot noise [47]. However, shot-noise measurement is technically more difficult than the standard conductance measurement because the noise signal is usually too small and buried by extrinsic noise from the measurement system. In particular, the Zeeman energy which affects the asymmetric reconstruction of spin-resolved QHECs is of the order of several hundreds of μV. Thus, to investigate the transmission process of nonequilibrium spin-resolved QHECs, we need to measure the shot noise with significantly high resolution, at least the order of 10^{-29} A^2/Hz. Therefore, an invention of a high-resolution shot-noise measurement system is required.

Experimentally, the auto-correlation $S_{\rm A} \equiv \langle \Delta I_{\rm A}^2 \rangle$ is usually measured to estimate the current-noise intensity in an output terminal. On the other hand, the cross-correlation $S_{\rm x} \equiv \langle \Delta I_{\rm A} \Delta I_{\rm B} \rangle$ is sometimes measured to evaluate not only the noise intensity but also the sign of the correlation between two distinct current noises $\Delta I_{\rm A}$ and $\Delta I_{\rm B}$. The cross-correlation measurement can improve the measurement resolution by a factor of $\sqrt{2}$. In addition, it can reveal the correlation between charge carriers in a conductor, e.g., electron correlation due to the two-particle interference[65] or the Pauli exclusion principle[66, 67] and quasiparticle correlation reflecting their anyonic statistics[68].

Despite the high potential of cross-correlation measurement, it is less common than auto-correlation measurement because the former has technical difficulties not found in the latter. One of the essential requirements is to suppress unwanted crosstalk among multiple measurement leads. In conventional setups using voltage amplifiers[49, 69, 70, 71], the crosstalk is often caused by the parasitic capacitance between the leads. A straightforward way to suppress the capacitively induced crosstalk is to decrease the parasitic capacitance by carefully designing the wiring and the device structure of a sample, though this approach is sometimes technically difficult. Another method is to reduce the input impedance of the voltage amplifiers by, for instance, installing resistors that shunt the leads to the ground. Albeit simple and technically easy, this method has a drawback of decreasing the noise intensity and thus degrades the measurement resolution. Replacing a voltage amplifier with a transimpedance amplifier (TA), which converts the input current to the output voltage with a high transimpedance, is another possible solution because the input impedance of a TA can be minimized[26]. The TA-based system has been successfully employed for some shot-noise measurements[72, 73]; however, the measurement resolution is worse than that in recent experiments using conventional voltage-amplifier-based setups (e.g., Ref. [68]).

For better resolution, it is necessary to lower the noise floor and/or widen the frequency bandwidth of a TA. Thus, we developed a cryogenic TA comprising homemade GaAs HEMTs with high transconductance and low-noise characteristics, suitable for current-noise measurements at low frequencies (the white-noise limit of the thermal and shot noise)[44, 74, 26]. The heterostructure and characteristics of the HEMT (gate length $L = 4\ \mu\mathrm{m}$; channel width $W = 3\ \mathrm{mm}$) are reported in detail in Ref. [71] . Thanks to the homemade HEMTs and the optimized circuit design, the noise floor of the TA is lowered to about $6 \times 10^{-27}\ \mathrm{A^2/Hz}$—more than one order of magnitude lower than that of our previous TA[75]—over a wide frequency band (from $200\ \mathrm{kHz}$ to $1\ \mathrm{MHz}$). The TA has a low input impedance of about $100\ \Omega$, which is small enough for suppressing crosstalk in cross-correlation measurements. We examined the resolution of the TA-based system by measuring the shot noise generated at a quantum point contact (QPC) in a quantum Hall (QH) system. The resolution is $0.69 \times 10^{-30}\ \mathrm{A^2/Hz}$ for a cross-correlation measurement with a data-integration time $\tau_{\rm int}$ of $100\ \mathrm{s}$, which is better than the typical resolution of conventional voltage-amplifier-based setups[49, 69, 70, 71].

This chapter is organized as follows. Section 6.1 overviews the TA-based noise-measurement system and discusses its general properties. Section 6.2 presents the circuit design of our TA and its performance. Section 6.3 demonstrates a shot-noise measurement using our TA. Section 6.4 summarizes this chapter.

6.1 Basics of current-noise measurement using transimpedance amplifier

6.1.1 Overview of the system

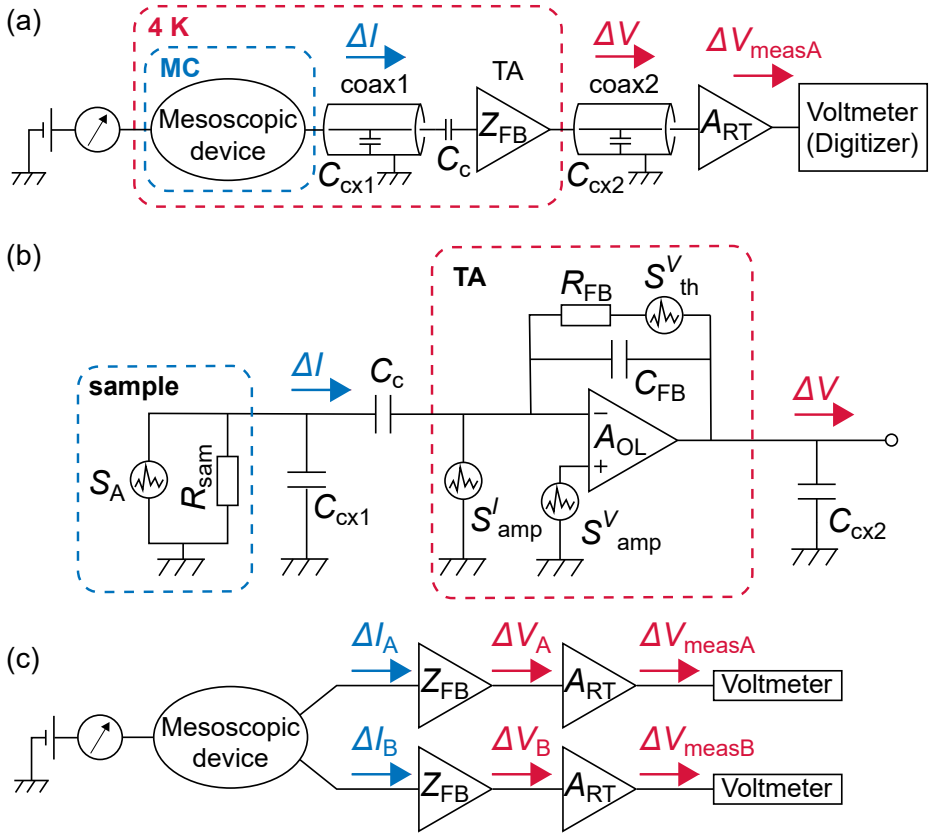

Figure 6.1: (a) Schematic of a setup for auto-correlation measurement using a TA. The current noise ΔI flowing from a mesoscopic device is converted to ΔV by the TA, amplified to $\Delta V_{\rm meas}$ by a commercial room-temperature amplifier, and then measured by a high-speed voltmeter. (b) Electric circuit model of the cryogenic assembly. (c) Simplified schematic of a setup for cross-correlation measurement using two TAs. Two distinct current noises, $\Delta I_{\rm A}$ and $\Delta I_{\rm B}$, are measured through different measurement lines.

Figure 6.1 (a) shows an overview of a setup for auto-correlation measurement for a mesoscopic device cooled down in a dilution refrigerator. Here, we consider applying a voltage bias to the device (resistance $R_{\rm sam}$) at the mixing-chamber (MC) temperature and measuring a current noise ΔI at an output terminal. The signal ΔI flows through a $50\ \Omega$ coaxial cable (coax1) with stray capacitance $C_{\rm cx1}$ and a coupling capacitor $C_{\rm c}$ to reach a TA placed at the 4-K stage. The TA converts ΔI to a voltage noise $\Delta V = Z_{\rm FB} \times \Delta I$, where $Z_{\rm FB}$ is the transimpedance. Then, ΔV is taken out of the refrigerator through another coaxial cable (coax2) with $C_{\rm cx2}$ and is amplified to $\Delta V_{\rm meas}$ by a commercial voltage amplifier. A high-speed voltmeter records the time domain $\Delta V_{\rm meas}$ data. We calculate the current-noise power spectrum density $P_{\rm A}^{\rm meas}(f) = \langle \Delta V_{\rm meas}^2 \rangle / (A_{\rm RT}|Z_{\rm FB}|)^2$ and eval-

uate the current-noise intensity $S_{\rm A}^{\rm meas}$ as the mean value of $P_{\rm A}^{\rm meas}(f)$ in the measurement frequency band[26, 75].

Figure 6.1(b) shows an equivalent circuit diagram of our cryogenic assembly, in which the operational-amplifier circuit models the TA (for details, see [75]). The transimpedance is given by $Z_{\rm FB}(\omega) = R_{\rm FB}/(i\omega C_{\rm FB}R_{\rm FB} + 1)$, where $R_{\rm FB}$ is the feedback resistance, $C_{\rm FB}$ is the phase-compensation capacitance, and ω is the angular frequency. The TA has the input impedance $Z_{\rm in} = Z_{\rm FB}/(A_{\rm OL} - 1)$ ($\cong R_{\rm FB}/A_{\rm OL}$ at low frequencies), where $A_{\rm OL}$ is the open-loop gain of the operational amplifier.

Experimentally, extrinsic noise as well as the intrinsic current noise $S_{\rm A} = \langle \Delta I^2 \rangle$ of interest, contributes to $S_{\rm A}^{\rm meas}$. When $Z_{\rm FB}$ is high, and the extrinsic noises generated at the room-temperature amplifier and the digitizer are small, the input-referred current noise $S_{\rm TA}^I$ of the TA dominates the extrinsic noise in the measurement system (ref. [26]): in this case, $S_{\rm A}^{\rm meas}$ is expressed as $S_{\rm A}^{\rm meas} = S_{\rm A} + S_{\rm TA}^I$. In general, $S_{\rm TA}^I$ consists of three components: the input current and voltage noise ($S_{\rm amp}^I$ and $S_{\rm amp}^V$, respectively) of the operational amplifier and the thermal noise $S_{\rm th}^V = 4k_{\rm B}T_{\rm FB}R_{\rm FB}$ of the feedback resistance (k_B, Boltzimann constant; $T_{\rm FB}$, the temperature of the feedback resistance).

In a cross-correlation measurement, one measures noise of the currents flowing out from separate parts of a multi-terminal device. More specifically, for two distinct current noises $\Delta I_{\rm A}$ and $\Delta I_{\rm B}$, we measure two sets of time-domain data ($\Delta V_{\rm measA}$ and $\Delta V_{\rm measB}$) through separate measurement lines connected to different parts of the device [see Fig. 6.1(c)]. Here, we assume that both lines have the same values of $Z_{\rm FB}$ and $A_{\rm RT}$. The measured cross-correlation $S_{\rm X}^{\rm meas}$ corresponds to the mean value of the cross power spectral density $P_{\rm X}^{\rm meas} = \langle \Delta V_{\rm measA} \Delta V_{\rm measB} \rangle / (A_{\rm RT}|Z_{\rm FB}|)^2$ in the measurement frequency band. In contrast to the auto-correlation measurement, extrinsic noise does not add to the measured noise $S_{\rm X}^{\rm meas}$ and we have $S_{\rm X}^{\rm meas} = S_{\rm X} \equiv \langle \Delta I_{\rm A} \Delta I_{\rm B} \rangle$ at long $\tau_{\rm int}$, since the extrinsic noises in the two measurement lines are uncorrelated.

6.1.2 Resolution

The resolution of a current-noise measurement is evaluated as the standard deviation σ of data points of repeated measurements (see Sec 6.3.4)[26, 49, 71]. When $S_{\rm TA}^I$ is much greater than $S_{\rm A}$, which is often the case, the standard deviation $\sigma_{\rm A}$ of the auto-correlation measurement is described as

$$\sigma_{\rm A} \cong S_{\rm TA}^I / \sqrt{N_{\rm data}}, \tag{6.1}$$

where $N_{\rm data} = f_{\rm BW}/\Delta f$ is the number of data points, $f_{\rm BW}$ is the frequency bandwidth used for the noise analysis, and $\Delta f = 1/\tau_{\rm int}$ is the frequency resolution. Equation (6.1) tells us that the lower $S_{\rm TA}^I$ and the wider $f_{\rm BW}$, the better the current-noise resolution. The standard deviation $\sigma_{\rm X}$ of the cross-correlation measurement is given by

$$\sigma_{\rm X} \cong \sigma_{\rm A}/\sqrt{2}, \tag{6.2}$$

manifesting that the resolution is better than that of the auto-correlation measurement. Here, we assume $S_{\rm TA}^I \equiv S_{\rm TA1}^I = S_{\rm TA2}^I$, where $S_{\rm TA1}^I$ and $S_{\rm TA2}^I$ are the input-referred noise of the two TAs.

6.1.3 Input-referred current noise

Using the extrinsic-noise components $S^I_{\rm amp}$, $S^V_{\rm amp}$, and $S^V_{\rm th}$, we describe $S^I_{\rm TA}$ as

$$S^I_{\rm TA}(\omega) = \frac{S^V_{\rm th} + G^2_{\rm N}(\omega) S^V_{\rm amp}(\omega)}{Z^2_{\rm FB}} + S^I_{\rm amp}(\omega). \tag{6.3}$$

Here, $G_{\rm N}(\omega)$ is the noise gain given by

$$G_{\rm N}(\omega) \equiv 1 + Z_{\rm FB}(\omega)/Z_{\rm sam}(\omega) \tag{6.4}$$

$$= 1 + \frac{R_{\rm FB}}{R_{\rm sam}} \frac{i\omega C_{\rm cx1} R_{\rm sam} + 1}{i\omega C_{\rm FB} R_{\rm FB} + 1}, \tag{6.5}$$

where $Z_{\rm sam}(\omega) \equiv R_{\rm sam}/(i\omega C_{\rm cx1} R_{\rm sam} + 1)$ denotes the parallel impedance of the sample and the input capacitance $C_{\rm cx1}$. The first and the second terms of Eq. (6.3) are obtained by converting $S^V_{\rm th}$ and $S^V_{\rm amp}$ to the equivalent current noise at the input of the TA, while the third term directly reflects $S^I_{\rm amp}$. In this study, we developed a TA of low $S^V_{\rm amp}$ and $S^I_{\rm amp}$ using homemade GaAs HEMTs. In addition, we further suppressed $S^I_{\rm TA}$ by employing high $R_{\rm FB}$ ($= 100\ {\rm k}\Omega$): the absolute value of the first term of Eq. (6.3) decreases with increasing $R_{\rm FB}$ at the cost of frequency bandwidth (see discussion in Sec. 6.1.4).

6.1.4 Frequency band

We choose the region where $|Z_{\rm FB}|$ is flat and $S^I_{\rm TA}$ is low to be the measurement frequency band. In the measurement setup in Fig. 6.1(b), $Z_{\rm FB}$ is independent of the frequency down to the frequency at which $C_{\rm c}$ becomes transparent and up to the -3 dB cutoff frequency $f_{-3\ {\rm dB}}[\cong (2\pi R_{\rm FB} C_{\rm FB})^{-1}$ when $Z_{\rm in} \cong 0]$. The low $S^I_{\rm TA}$ band, which is from the TA's $1/f$ corner frequency to the characteristic frequency $f_{\rm c} = (2\pi R_{\rm sam} C_{\rm cx1})^{-1}$ of $G_{\rm N}(\omega)$, is generally narrower than the flat $|Z_{\rm FB}|$ band. Equation (6.4) tells us that $G_{\rm N}(\omega) \cong 1 + R_{\rm FB}/R_{\rm sam}$ at low frequencies, while $G_{\rm N}(\omega) \cong 1 + C_{\rm cx1}/C_{\rm FB}$ at high frequencies. Because $R_{\rm FB}/R_{\rm sam} < C_{\rm cx1}/C_{\rm FB}$ under a standard condition, $G_{\rm N}(\omega)$ increases with frequency above the characteristic frequency $f_{\rm c}$.

In this study, we enhanced the upper-frequency limit by placing the TA as close to a sample as possible to shorten coax1, reduce $C_{\rm cx1}$, and hence increase $f_{\rm c}$. Note that $C_{\rm cx2}$ does not appear in the above discussion because we suppressed the influence of $C_{\rm cx2}$ by installing a source follower at the output of the TA (see Sec. 6.2 A).

6.2 Homemade-HEMT-based transimpedance amplifier

6.2.1 Circuit design

Figure 6.2 shows the circuit design of our TA, which is composed of the main part and the output buffer coupled in series via a coupling capacitor $C_{\rm MB} = 100$ nF. The main part (red dotted line) comprises four HEMTs. The first three (H1-H3) form three-step self-biased common-source circuits with the load resistance $R_{\rm L} = 510\ \Omega$, and the last (H4)

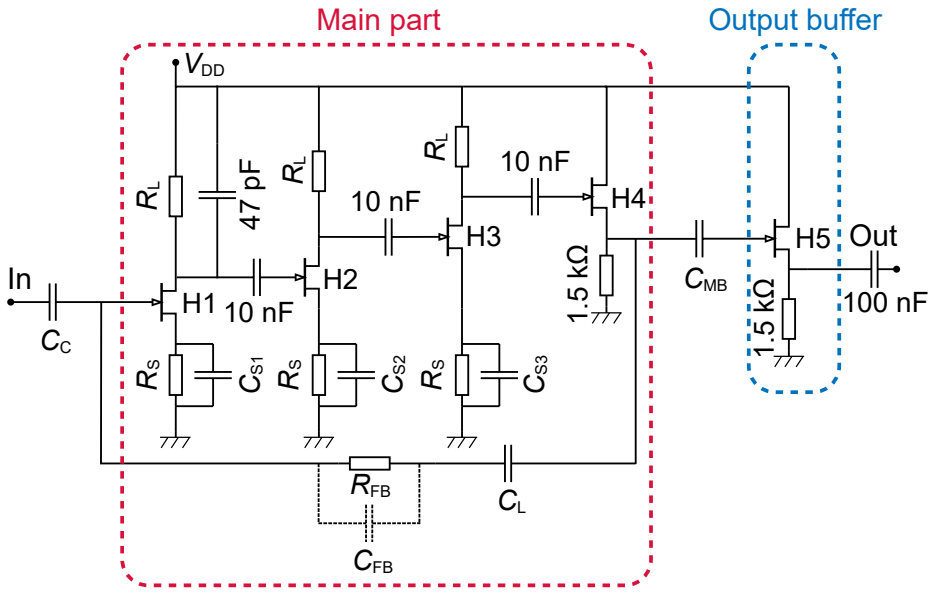

Figure 6.2: Circuit diagram of the homemade-HEMT-based TA. The circuit parameters are $R_S = 510\ \Omega$, $R_L = 510\ \Omega$, $C_{S1} = 47$ nF, $C_{S2} = 200$ nF, $C_{S3} = 800$ nF, $C_C = C_L = C_{MB} = 100$ nF, and $R_{FB} = 100\ \mathrm{k}\Omega$. The TA operates at $V_{DD} \cong 1$ V, showing low-noise characteristics.

serves as a source follower that reduces the output impedance. The common-source circuits and the source follower are connected in series through coupling capacitors of 10 nF that decouple the dc biases applied to the four HEMTs. The high transconductance and low-noise characteristics of the HEMT lead to a high voltage gain and low S^I_{amp} and S^V_{amp} of the common-source circuits[71]. The source resistance $R_S = 510\ \Omega$ and the parallel capacitance form the self-biasing circuit: we chose different source capacitance values for the three common-source circuits ($C_{S1} = 47$ nF, $C_{S2} = 200$ nF, or $C_{S3} = 800$ nF) for their phase shifts not to maximize at the same frequency and cause instability. The 47-pF drain capacitance of H1 suppresses A_{OL} at high frequencies and thereby prevents unwanted instability of the TA. The 100-kΩ resistor R_{FB} and the coupling capacitor $C_L = 100$ nF connected in series between the output and input give a negative feedback in the main part. Here, R_{FB} has a parallel parasitic capacitance of about 0.3 pF, which works as a phase-compensation capacitance C_{FB} [see Fig. 6.1]. The output buffer (blue dotted line), another source follower consisting of H5, interrupts the direct connection between the main part and C_{cx2} that induces an undesirable phase shift in the feedback circuit. Note that the above circuit parameters are selected to lower the input-referred noise of the TA in the measurement frequency band.

We place the TA at 4 K in a dilution refrigerator and apply a dc bias $V_{DD} = 0.968$ V. Because the input-referred current noise of the TA increases with frequency above f_c, it is essential to suppress C_{cx1}, which is proportional to the length of coax1 [see Fig. 6.1 (a) and 6.1 (b)], for a wide-band high-resolution measurement (see discussion in Sec. 6.1.4). To meet this requirement, we made an additional stage that was thermally equilibrated with the 4-K plate and located below the MC plate and placed the TAs on it. A radiation shield equilibrated with the still plate covers the additional stage. In this setup, the dis-

tance between the TAs and the sample located at the magnetic-field center is $\cong$ 20 cm, and $C_{\rm cx1}$ of coax 1 (GVL Cryoengineering GVLZ137, 61 pF/m) is $\cong$ 10 pF. This $C_{\rm cx1}$ value gives $f_{\rm c} \cong 1$ MHz for a typical mesoscopic sample of a few tens of kΩ, providing a low noise floor over a wide frequency band. The output capacitance $C_{\rm cx2}$ is about 100 pF. The TA has the input impedance $Z_{\rm in} \cong 100\ \Omega$, a value much smaller than that of conventional voltage-amplifier-based systems[49, 69, 70, 71], manifesting the suitability of our TA for cross-correlation measurements. The output impedance $Z_{\rm out}$ is about 30 Ω. The energy consumption of the TA is about 1.5 mW, which is sufficiently small compared to the cooling power of the 4-K stage of a standard dilution refrigerator. In the following experiments, a room-temperature amplifier (NF corporation SA-421F5: gain $A_{\rm RT} = 46$ dB; input impedance 1 MΩ) was used to amplify the signal ΔV to $\Delta V_{\rm meas}$, and a digitizer (National Instruments PXI-5922) provided high-speed voltmeters to record the time-domain $\Delta V_{\rm meas}$ data.

6.2.2 Frequency-response characteristics

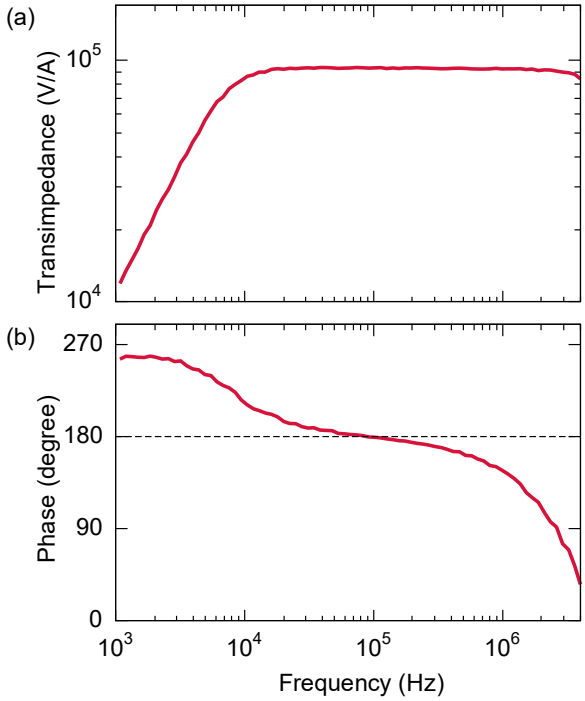

Figure 6.3: (a) Absolute transimpedance $|Z_{\rm FB}|$ and (b) phase $\arg(Z_{\rm FB})$ of the TA at 4 K as a function of frequency. Sample resistance is $R_{\rm sam} = 13.4$ kΩ, and the input capacitance is $C_{\rm cx1} \cong$ 10 pF.

We applied an ac input current of 14.9 $\rm nA_{rms}$ to the TA through a resistor $R_{\rm sam} =$ 13.4 kΩ at the mixing-chamber temperature ($T_{\rm MC} = 42$ mK). Figures 6.3 (a) and (b) present the measured $|Z_{\rm FB}|$ and the phase response $\arg(Z_{\rm FB})$, respectively. The TA shows $|Z_{\rm FB}| = 9.3 \times 10^4$ V/A $\pm$ 0.4 % in the measurement frequency band (from 200 kHz to 1 MHz, see Sec. 6.2.3). The phase response of $\arg(Z_{\rm FB}) \cong 180$ degrees in the measurement frequency band ensures the negative feedback in the TA circuit.

6.2.3 Noise characteristics

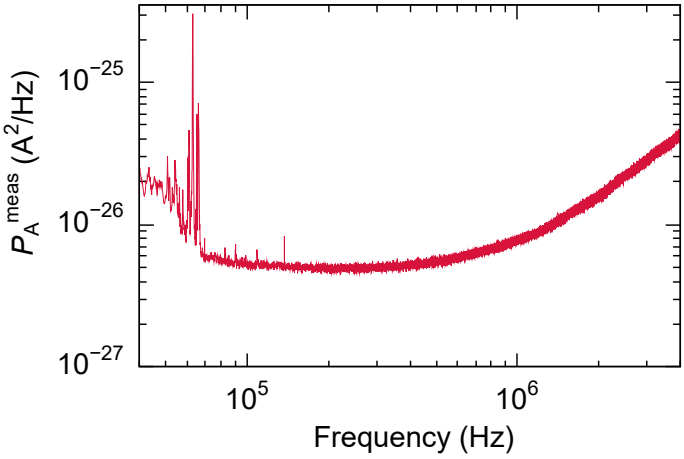

Figure 6.4: Current-noise spectral density $P_{\rm A}^{\rm meas}(f)$ measured with a sample ($R_{\rm sam} = 13.4\,{\rm k}\Omega$) at $T_{\rm MC} = 42\,{\rm mK}$. The input stray capacitance is $10\,{\rm pF}$. The $P_{\rm A}^{\rm meas}(f)$ data correspond approximately to the spectral density of the TA's input-referred current noise.

We evaluated the noise characteristics of the TA by measuring $S_{\rm A}^{\rm meas}$ with the same sample ($R_{\rm sam} = 13.4\ {\rm k}\Omega$, $T_{\rm MC} = 42\ {\rm mK}$). We grounded the source terminal of the sample to the mixing chamber plate not to generate non-equilibrium noise. In this case, $S_{\rm A} \cong 4k_{\rm B}T_{\rm e}/R_{\rm sam} \ll S_{\rm TA}^I$ ($T_{\rm e}$, electron temperature) so that we can directly evaluate $S_{\rm TA}^I$ as $S_{\rm A}^{\rm meas} \cong S_{\rm TA}^I$.

Figure 6.4 shows a current-noise spectral density $P_{\rm A}^{\rm meas}(f)$ obtained for the TA. The spectral density shows a broad minimum around $200\ {\rm kHz}$, and the minimum value (about $5 \times 10^{-27}\ {\rm A}^2/{\rm Hz}$) is close to the thermal noise $S_{\rm th}^V/|Z_{\rm FB}|^2 \cong 2.7 \times 10^{-27}\ {\rm A}^2/{\rm Hz}$ of the feedback resistance $R_{\rm FB} = 100\ {\rm k}\Omega$ at $4\ {\rm K}$ [see eq. (6.3)]. This observation indicates that $S_{\rm TA}^I$ mainly originates from the thermal noise, and therefore it can be lowered even more by cooling the TA further [e.g., by placing it on the still stage of the dilution refrigerator (typically 1 K)]. The noise intensity increases due to the $1/f$ noise or other extrinsic noise at low frequencies and the enhanced $|G_{\rm N}|$ at high frequencies. In this study, we set the measurement frequency band from $200\ {\rm kHz}$ to $1\ {\rm MHz}$. The bandwidth is about 2.7 times as broad as that of the previous TA, and the input-referred noise is about $6 \times 10^{-27}\ {\rm A}^2/{\rm Hz}$ on average, about 1/17 of the previous one[75].

6.3 Shot-noise measurement

6.3.1 Measurement setup and analysis

We measured the shot noise generated at a QPC placed at $T_{\rm MC} = 42\ {\rm mK}$ to demonstrate high resolution of the TA-based measurement system. We prepared two measurement lines containing TAs of similar characteristics [see Figs. 6.3 and 6.4]. Figure 6.5(a) shows a schematic of our device and the experimental setup with a scanning electron micrograph of

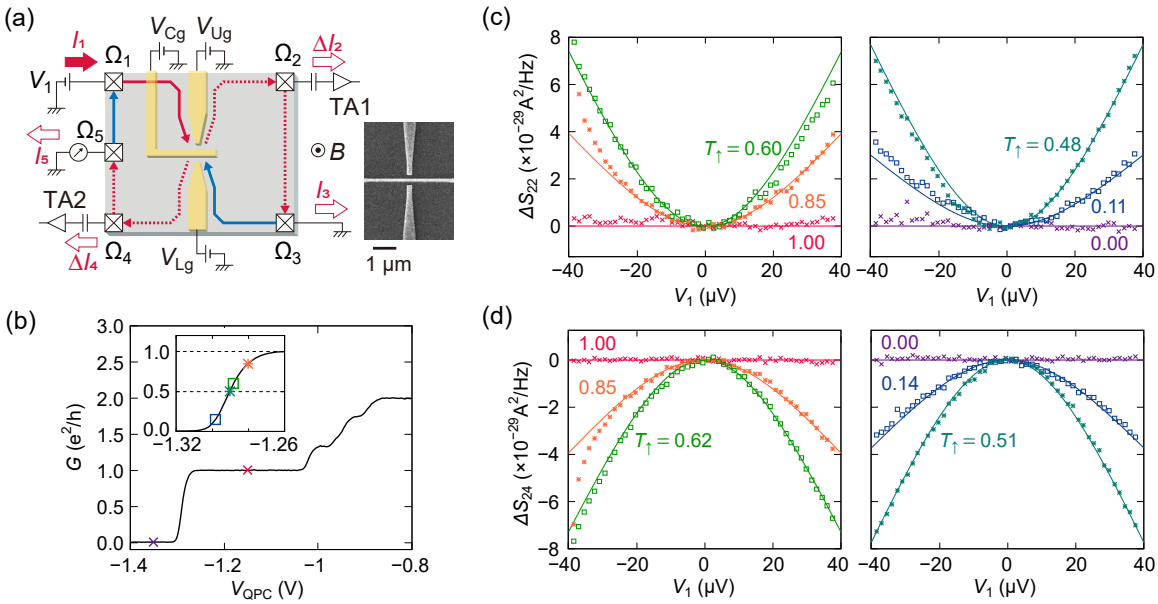

Figure 6.5: (a) Left (main panel): Schematic of the QH device and measurement setup. Right (inset): Scanning electron micrograph of the device. (b) Zero-bias QPC conductance G as a function of $V_{\rm QPC} = V_{\rm Ug} = V_{\rm Lg}$ with $V_{\rm Cg} = 0.2$ V. Inset: magnified view at -1.32 V $< V_{\rm QPC} < -1.26$ V. Contact resistance 520 Ω is subtracted. The colored symbols superimposed on the conductance traces indicate the $V_{\rm QPC}$ values, where the shot-noise measurements were performed. (c) V_1 dependence of auto-correlation ΔS_{22} measured at $T_\uparrow = 1.00$ (red), 0.85 (orange), 0.60 (green), 0.48 (blue green), 0.11 (blue), and 0.00 (purple). Solid curves are simulations using Eq. (6.6) at $T_{\rm e} = 91$ mK. (d) V_1 dependence of cross-correlation ΔS_{24} measured at $T_\uparrow = 1.00$ (red), 0.85 (orange), 0.62 (green), 0.51 (blue green), 0.14 (blue), and 0.00 (purple). Solid curves indicate simulation results using Eq. (6.7) at $T_{\rm e} = 91$ mK.

the device in the right inset. The QPC was fabricated in a two-dimensional electron system (2DES) with electron density $n_{\rm e} = 1.0 \times 10^{11}$ cm^{-2} and mobility $\mu = 3.4 \times 10^6$ cm^{2}V^{-1}s^{-1} in a GaAs quantum well. A perpendicular magnetic field of 2 T sets the 2DES at the filling factor $\nu = 2$ integer QH state, where the clockwise chiral edge transport allows us to perform auto- and cross-correlation shot-noise measurements analogous to quantum optics experiments[26]. The split-gate voltage $V_{\rm Ug} = V_{\rm Lg} = V_{\rm QPC}$ energizes the upper and lower Ti/Au Schottky gates to deplete the 2DES underneath and form the QPC. In addition, the center-gate voltage $V_{\rm Cg} = 0.2$ V facilitates the one-dimensional transport in the QPC[76].

We applied a bias voltage V_1 to the Ohmic contact Ω_1 to induce an electron current I_1 that impinges on the QPC. The transmitted (reflected) current flows along the edge channel to Ω_2 (Ω_4), where only its finite-frequency component ΔI_2 (ΔI_4) is fed to TA1 (TA2) through the coupling capacitor. The dc component I_3 (I_5) is collected at Ω_3 (Ω_5) located downstream. We measured the differential QPC conductance $g = dI_3/dV_1 = 2e^2/h - dI_5/dV_1$ using a standard lock-in technique with an ac modulation on V_1 (1 $\mu V_{\rm rms}$, 76.6 Hz), where e is the elementary charge and h is the Planck constant.

Figure 6.5 (b) presents the zero-bias QPC conductance $G = g(V_1 = 0$ V) measured

as a function of $V_{\rm QPC}$, in which G decreases with decreasing $V_{\rm QPC}$ from $2e^2/h$ to zero, showing a well-developed e^2/h plateau at $-1.25\ {\rm V} < V_{\rm QPC} < -1.05\ {\rm V}$. The stepwise variation of G, with the e^2/h plateau, reflects the spin-resolved transport through the QPC. We performed shot-noise measurements on and below the first conductance plateau ($0 \leq G \leq e^2/h$), where the QPC fully reflects spin-down electrons. In this regime, the transmission probability $T_\uparrow$ of spin-up electrons is evaluated as $T_\uparrow = (h/e^2)G$, while that of spin-down electrons ($T_\downarrow$) is zero.

Below, we present auto- ($S_{22} \equiv \langle \Delta I_2^2 \rangle$) and cross-correlation ($S_{24} \equiv \langle \Delta I_2 \Delta I_4 \rangle$) data at several values of $V_{\rm QPC}$ indicated by the symbols in Fig. 6.5 (b) and its inset. The procedure for the measurement and analysis was as follows: we continuously retrieved time-domain data at a $10\ {\rm MS/s}$ sampling rate and performed FFT analysis on each data set containing 10^5 data points acquired in sequence. We repeated this sequence $10\,000$ times, acquired a noise spectral density by averaging the FFT spectral densities, and then evaluated S_{22} or S_{24} as the mean value of the averaged spectral density in the measurement frequency band. This procedure requires $\tau_{\rm int} = 100\ {\rm s}$ and gives the effective number of data points $N_{\rm data} = f_{\rm BW}/\Delta f \times 10^4 = 8 \times 10^7$ ($f_{\rm BW} = 800\ {\rm kHz}$; $\Delta f = 100\ {\rm Hz}$).

6.3.2 Auto correlation measurement

Figure 6.5 (c) shows the results of auto-correlation measurements for the bias-induced excess noise $\Delta S_{22}(V_1) = S_{22}(V_1) - S_{22}(0)$ at several $T_\uparrow$ values. At intermediate values of $T_\uparrow$ ($0 < T_\uparrow < 1$), ΔS_{22} increases with $|V_1|$, signaling the shot-noise generation due to the electron partitioning at the QPC. In contrast, we observe $\Delta S_{22} \cong 0$ over the entire V_1 range at $T_\uparrow = 0$ or 1, where the QPC fully reflects or transmits electrons. Note that g, and hence $T_\uparrow$ is almost independent of V_1 in the measurement V_1 range, manifesting that the QPC is in the linear-response regime[1].

We compare the experimental results with theoretical shot-noise curves calculated as

$$S_{\rm A}^{\rm shot} = 2eV_1G_0F\left[\coth\left(\frac{eV_1}{2k_{\rm B}T_{\rm e}}\right) - \frac{2k_{\rm B}T_{\rm e}}{eV_1}\right], \tag{6.6}$$

where $G_0 = 2e^2/h$ and $F = \left[\Sigma_\sigma T_\sigma(1-T_\sigma)\right]/2$ ($\sigma = \uparrow, \downarrow$) is the shot-noise reduction factor[44, 26]. The solid lines in Fig. 6.5 (c) are the simulated theoretical curves assuming $T_{\rm e} = 91\ {\rm mK}$[2]. All the experimental data sets are close to the theoretical curves, justifying the current-noise measurements using our TA.[1]

6.3.3 Cross correlation measurement

We also performed cross-correlation measurements for the bias-induced excess noise and compared the result $\Delta S_{24}(V_1) = S_{24}(V_1) - S_{24}(0)$ with the theoretical cross-correlation

[1] We observed slight decrease in g at $V_{\rm QPC} = -1.28\ {\rm V}$ (green asterisk) at $V_1 < -25\ \mu{\rm V}$ (from $T_\uparrow = 0.85$ to 0.82), suggesting the presence of unintentional impurity scattering near the QPC. Tiny deviations of the noise data from the theoretical curves observed in Figs. 6 and 7 may be due to such unintentional scatterings, or a slight change in electron temperature during the measurements.

[2] We obtained the value $T_e = 91\ {\rm mK}$ from the fit to the cross-correlation data at $T_\uparrow = 0.51$.

shot noise[44],

$$S_{\mathrm{X}}^{\mathrm{shot}} = -2eV_1G_0F\left[\coth\left(\frac{eV_1}{2k_{\mathrm{B}}T_{\mathrm{e}}}\right) - \frac{2k_{\mathrm{B}}T_{\mathrm{e}}}{eV_1}\right]. \tag{6.7}$$

Figure 6.5 (d) presents the comparison between the experiment and the theory. As expected from the theory, cross correlation takes negative values, reflecting the one-by-one partitioning of electrons at the QPC; that is, an electron is either transmitted or reflected. The measured ΔS_{24} agrees well with the theoretical curves, again assuring the quantitative accuracy of the measurement.

6.3.4 Resolution

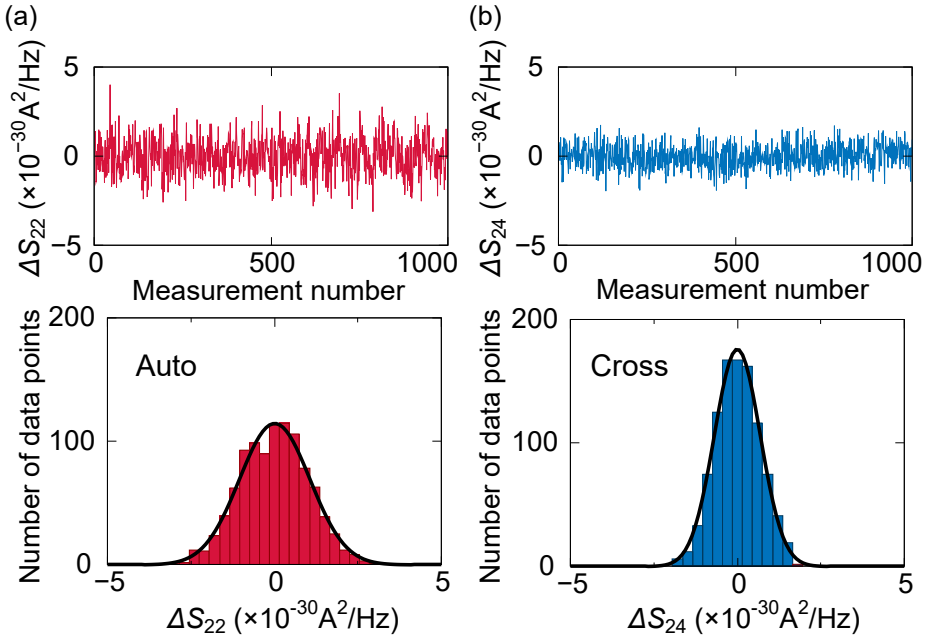

Figure 6.6: (a) ΔS_{22} and (b) ΔS_{24} data for measurements repeated 1 000 times ($V_{\mathrm{QPC}} = 0.2$ V, $V_1 = 0$ V, and $\tau_{\mathrm{int}} = 100$ s). (lower panels) Histogram analysis: 0.3×10^{-30} A^2/Hz for a bin. Solid lines show Gaussian fits. The resolutions of the auto- and cross-correlation measurements are evaluated from the fits as $\sigma_{\mathrm{A}} = 1.06 \pm 0.03 \times 10^{-30}$ A^2/Hz and $\sigma_{\mathrm{X}} = 0.69 \pm 0.01 \times 10^{-30}$ A^2/Hz, respectively.

To evaluate the resolution of our measurements, we repeated the auto- and cross-correlation measurements 1 000 times, at zero-bias with the QPC fully opened ($G = G_0$). Figures 6.6 (a) and (b) present the results of the measurements. The vertical axis shows the deviation from the mean value, $\Delta S_{22(24)} = S_{22(24)} - \langle S_{22(24)} \rangle$. A change in the S_{22} value induced by temperature drift ($\cong 1 \times 10^{-29}$ A^2/Hz, which corresponds to 3 mK) is subtracted from the auto-correlation results, whereas the subtraction is unnecessary for the cross-correlation results since the thermal noise does not directly contribute to S_{24}[75]. The bottom panels show the histogram analysis. One observes that the resolutions of the

auto-correlation measurement is $\sigma_{\rm A} = 1.06 \pm 0.03 \times 10^{-30}$ A^2/Hz, which is in reasonable agreement with the value $S^I_{\rm TA}/\sqrt{N_{\rm data}} \cong 0.67 \times 10^{-30}$ A^2/Hz expected from eq. (6.1) ($S^I_{\rm TA} = 6 \times 10^{-27}$ A^2/Hz; $N_{\rm data} = 8 \times 10^7$). The cross-correlation measurement gives $\sigma_{\rm X} = 0.69 \pm 0.01 \times 10^{-30}$ A^2/Hz, satisfying the relation of eq. (6.2). Due to the better resolution, the cross-correlation measurement shows less deviation between the experimental data and the theoretical curves than the auto-correlation measurement [see Figs. 6.5 (c) and (d)].

Let us compare the obtained resolutions with those of the previous measurement systems. The voltage-amplifier-based setup in Ref. [49], using a common-source circuit comprising a commercial HEMT (Agilent ATF-34143), showed a resolution of 28×10^{-30} A^2/Hz for a cross-correlation measurement with $\tau_{\rm int} = 10$ s, which corresponds to 8.9×10^{-30} A^2/Hz for $\tau_{\rm int} = 100$ s. The setup in Ref. [75], using TAs composed of commercial HEMTs (Agilent ATF-35143), has a resolution corresponding to 18×10^{-30} A^2/Hz for $\tau_{\rm int} = 100$ s. Compared to these setups, the present setup achieved a better resolution of more than one order of maginitude, thanks to the homemade HEMTs. Furthermore, the voltage-amplifier-based auto-correlation setup reported in Ref. [71], comprising a homemade HEMT similar to the one used in the present study, showed a resolution corresponding to 3.7×10^{-30} A^2/Hz for $\tau_{\rm int} = 100$ s. The present setup improves resolution by a factor of 3.5, thanks to the broader measurement bandwidth of the TA-based system (Ref. [71], $f_{\rm BW} = 30$ kHz; the present system, $f_{\rm BW} = 800$ kHz.

6.4 Conclusion

We have presented the cryogenic homemade-HEMT-based TA capable of mesoscopic current-noise measurements. The low input-referred noise and the broad frequency band of the TA enables us to perform high-resolution current-noise measurements. The low input impedance of the TA makes it particularly suitable for cross-correlation measurements. Our noise-measurement setup will be helpful for evaluating tiny noise cross-correlations in mesoscopic devices.

Chapter 7

Coherency of inter-channel transmission probed by shot noise

本章については、５年以内に雑誌等で刊行予定のため、非公開。

Chapter 8

Conclusion

This thesis aimed to identify what sort of quantum operations on electron spin is possible via the control of electron orbitals in the SOMCS. To answer the above question experimentally, we focused on the spin-resolved quantum Hall edge states as an ideal platform of the SOMCS for quantum operations.

In Ch. 4, we showed a concrete method for independent control of the zenith and azimuth angles of spin in the spin-resolved QHECs by utilizing three independent gate electrodes. The transmission probability is affected by the curvature at the position of QHECs' corner and can be controlled via gate voltages. The origin of the change in the transmission probability by the gate voltage is well explained by the Landau-Zener-type tunneling. The maximum controllable value of θ, estimated as a lower bound from the oscillation data, was only $\theta \approx 17^\circ$ in this experiment. Thus, the question of whether it is possible to create SOMeS ($\theta = \pi/2$) was left unanswered.

In Ch. 5, we demonstrated the way to realize a half-mirror ($\pi/2$ rotation in θ) on the spin-resolved QHECs, using a metal gate with an acute angle corner. We were able to control the transmission probability of the BS from approximately 0 % to over 50 % by modulating the distance between the copropagating QHECs via gate voltage. We fabricated an MZI with the BSs, which showed high visibility up to 60 %, reflecting the coherent partition at the BS. Our numerical calculation revealed that the transmission probability of the BS is affected by the gradient of confining potential at the position of QHECs, the angle of the gate corner, and the SOI strength. The SOMeS was probably created in this experiment, but limited visibility raised the possibility of decoherence at the BS. Thus, a different approach, namely the shot-noise measurement, is required to evaluate the coherence of the single BS.

In Ch. 6, we presented the cryogenic homemade-HEMT-based transimpedance amplifier (TA) capable of mesoscopic current-noise measurements. The low input-referred noise and the broad frequency band of the TA enabled us to perform high-resolution current-noise measurements. The low input impedance of the TA makes it particularly suitable for cross-correlation measurements. We examined the resolution of the TA-based system by measuring the shot noise generated at a quantum point contact (QPC) in a quantum Hall (QH) system. The resolution is $0.69 \times 10^{-30}\ \mathrm{A}^2/\mathrm{Hz}$ for a cross-correlation measurement with a data-integration time τ_{int} of $100\ \mathrm{s}$, which is better than the typical resolution of conventional voltage-amplifier-based setups.

In Ch. 7, we measured the shot noise generated by the transmission between the spin-resolved QHECs. The shot-noise amplitude, which reflects the rate of inelastic processes in the transmission, has shown asymmetric behavior for the bias voltage originating from the edge-channel reconstruction. The transmission between the spin-resolved QHECs is elastic at the low-bias condition, which is consistent with our assumption that the SOMeS was created at the BS presented in Ch. 5. However, the possibility of the existence of decoherence caused by, e.g., the e-e interaction was not denied.

Finally, let us consider the prospects of this study. We believe that our work has made an important contribution to the field of electron quantum optics[77, 78]. In particular, our electronic MZI presented in Ch. 5 has both high visibility (60%) and scalability, which is an advantage over other methods. For example, as far as we know, the highest visibility (80%) has been reported in the QHEC-based MZI utilizing QPCs as BSs[18], each of which partially transmits electrons from one QHEC to another *counterpropagating* QHEC. However, the freedom in designing electronic interferometers with QPC-BSs is limited mainly due to the topological constraints, e.g., series concatenation of MZIs is difficult[79]. On the other hand, MZIs using *copropagating* QHECs, like our method, can solve the problem, but the previously reported visibility was only around 10%[80, 81] probably due to the small transmission probability and decoherence at the BSs. Therefore, our BS and MZI are more promising building blocks than ever for more complex interferometers, enabling us to conduct multiple qubit operations. One of the candidates is the Hanbury Brown and Twiss interferometer[82] [see Fig. 8.1 (left)], which is capable of testing Bell inequalities[83, 84] by making the entangled electron-hole pare as two qubits. Although the interferometer can be realized using the QPC-BSs[65], violation of the Bell inequality has not been observed yet due to the small visibility, which is partially caused by the large interference area of annular geometry. On the other hand, our BS does not require such annular geometry [see Fig. 8.1 (right)] [79], leading to the much smaller interference area. The ultimate application is quantum information processing[85], combined with single-electron sources [86, 87, 40, 88], detectors [89], and conditional phase shifters [90].

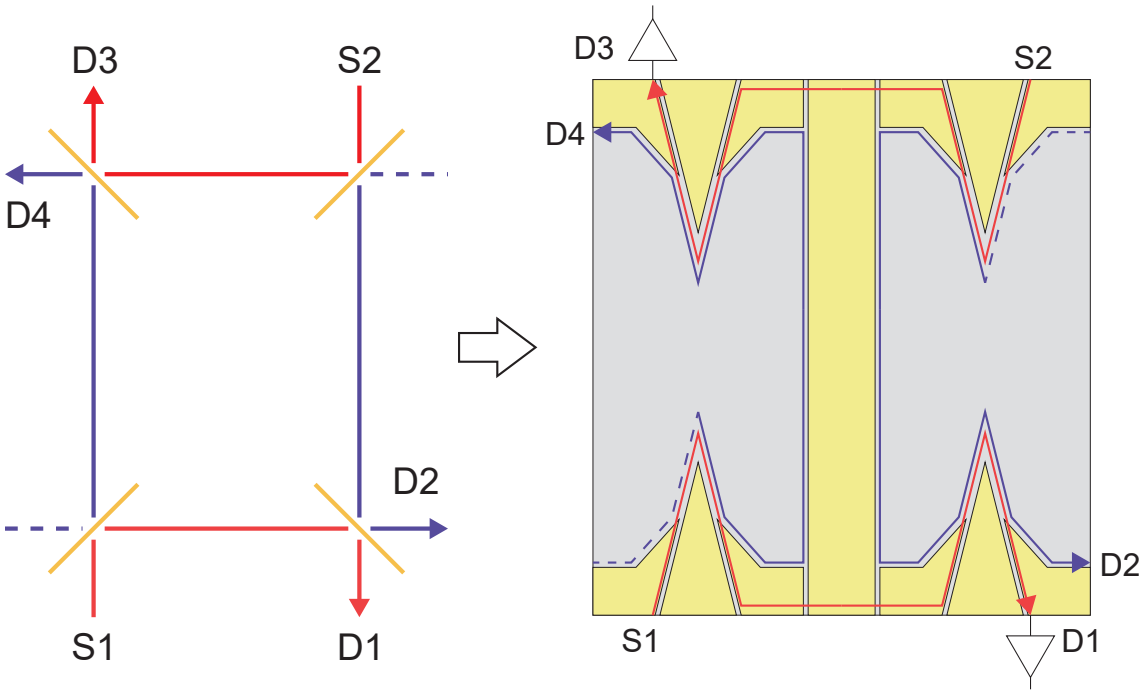

Figure 8.1: (Left) Schematics of electronic Hanbury Brown and Twiss interferometer and (right) corresponding proposal of gate design utilizing our BSs.

Appendix A

Numerical Calculations

A.1 Schrödinger-Poisson equations

The 2DES electron density and conduction band energy level in the vertical direction shown in Fig. 3.1 is given by the self-consistent one-dimensional Schrödinger-Poisson equations,

$$\nabla \cdot (-\epsilon \nabla V(x)) = \rho, \tag{A.1}$$

$$\rho = e(p - n + N_D), \tag{A.2}$$

$$n(x) = \sum_j \sum_k f_{\mathrm{FD}} \left(\frac{E_{jk} - E_{\mathrm{F}}}{k_{\mathrm{B}} T} \right) |\Psi_{jk}(x)|^2, \; p(x) = 0, \tag{A.3}$$

$$\left[-\frac{d}{dx} \frac{\hbar^2}{2m^*(x)} \frac{d}{dx} + E_c(x) - eV(x) \right] \Psi_{jk}(x) = E_{jk} \Psi_{jk}(x), \tag{A.4}$$

where ϵ is permittivity; ρ charge density; V electric potential; N_{D} donor doping concentration; f_{FD} the Fermi-Dirac distribution function; E_{F} Fermi energy; E_{c} conduction band energy level; k_{B} the Boltzmann constant; T temperature; m^* effective-mass of electron; e elementary charge; n electron density; p hole density (ignored);

We calculate electron density and conduction band energy level only for $k = 0$ point and thus eq.(A.3) becomes

$$n(x) \approx \sum_j f_{\mathrm{FD}} \left[\frac{1}{k_{\mathrm{B}} T} \left(E_{j0} + \frac{\hbar^2 k^2}{2m^*} - E_{\mathrm{F}} \right) \right] |\Psi_{j0}(x)|^2. \tag{A.5}$$

We set the doping density $N_{\mathrm{D}} = 7.95 \times 10^{17}\ \mathrm{cm}^{-3}$ so that the calculated 2DES sheet density can be $4.4 \times 10^{11}\ \mathrm{cm}^2$, which is the same value as the sample that we used.

A.2 Simulation of electrostatic potential using the density-gradient theory

For qualitative discussions on the change of the edge channel shape for the side gate voltages, we carried out a numerical calculation using the semiconductor module of commer-

cial program COMSOL Multiphysics [64]. Here, to include the effect of quantum confinement into the classical drift-diffusion method, we adopt the density-gradient theory [91], which requires lighter computational resources than the Poisson-Schrödinger scheme shown in Sec. A.1. A comprehensive review of the density-gradient theory is found in Ref. [92].

Below we briefly summarize the equations and the calculation scheme of the density-gradient theory. For simplicity, only the equations for electrons are shown here, because contributions of holes are ignorable in the present problem. We also omit terms for recombination and generation of carriers. The common symbols with those in Sec. A.1 have the same meanings. The first is the Poisson equation

$$\nabla \cdot (-\epsilon \nabla V) = \rho. \tag{A.6}$$

The charge density ρ is written as

$$\rho = e(-n + N_{\mathrm{D}}^{+}), \tag{A.7}$$

where N_{D}^{+} is the charged donor concentration. The electron density n obeys the charge-conservation law

$$\frac{\partial n}{\partial t} + \frac{\nabla \cdot \boldsymbol{J}_n}{-e} = 0, \tag{A.8}$$

where t is time and, $\boldsymbol{J}_n$ is the electron current density, which can be expressed in terms of the quasi-Fermi level $E_{\mathrm{F}n}$ as in

$$\boldsymbol{J}_n = en\mu_n \nabla E_{\mathrm{F}n} + en((E_{\mathrm{c}} - E_{\mathrm{F}n})\mu_n + Q_n)\nabla T/T, \tag{A.9}$$

where μ_n is the electron mobility, Q_n is nonequilibrium contribution to the diffusion coefficient, and T is the temperature. The conduction band energy level E_{c} is related to V and the electron affinity χ as

$$E_{\mathrm{c}} = -V - \chi. \tag{A.10}$$

In the drift-diffusion theory, the spatial distribution of n is described by the quasi-Fermi levels $E_{\mathrm{F}n}$. In the density-gradient theory, the contribution from the gradient of the carrier concentration is taken into account in the form of the quantum potential V_n^{DG} as

$$n = N_{\mathrm{c}} F_{\mathrm{FD}}\left(\frac{E_{\mathrm{F}n} - E_{\mathrm{c}} + eV_n^{\mathrm{DG}}}{k_{\mathrm{B}}T}\right), \tag{A.11}$$

where N_{c} is the effective density of states in the conduction band, F_{FD} is the Fermi-Dirac integral, and V_n^{DG} is defined as

$$V_n^{\mathrm{DG}} \equiv \frac{2}{\sqrt{n}} \Delta \cdot (\boldsymbol{b}_n \nabla \sqrt{n}). \tag{A.12}$$

The density-gradient coefficient $\boldsymbol{b}_n$ is a constant-multiplied inverse of the effective mass tensor $\boldsymbol{m}_n$:

$$\boldsymbol{b}_n = \frac{\hbar^2}{12e} [\boldsymbol{m}_n]^{-1}, \tag{A.13}$$

where $\hbar$ is the Planck constant multiplied $(2\pi)^{-1}$. We finally introduce a Slotboom variable ϕ_n as

$$n = \exp\left(\frac{e\phi_n}{k_{\mathrm{B}}T}\right), \tag{A.14}$$

and solve the implicit equations Eq.(A.11) and Eq.(A.12).

Henceforth we show the results of calculations of electrostatic quantities for a metallic gate configuration (the blue regions in Fig.A.1) on two-dimensional electrons. We use finite element density-gradient (linear shape function) formulation. The reference temperature is 273 K, at which the equilibrium Fermi level is defined. Here "equilibrium" is defined as the state in which no applied voltages or currents exist, and the temperature is uniform throughout the model. The density-gradient effective mass tensor $\boldsymbol{m}_n$ is set to $\boldsymbol{m}_n = 0.067m_0\boldsymbol{I}$, where $0.067m_0$ is the effective mass of GaAs and $\boldsymbol{I}$ is the identity matrix. The doping density is set to $6.2\times10^{17}\ \mathrm{cm}^{-3}$, which gives the electron sheet density of the 2DES used in the experiment.

As an example, Fig. A.1 shows the finite-element mesh used for calculation which we used in Ch. 4. Gate SR and Gate R are defined on the top surface of the mesh. An ideal Schottky-type metal contact option with a 4.5 V metal work function was used for Gate SR and Gate R. The Fermi-level pinning on the exposed top GaAs/AlGaAs surfaces is also included by the same metal contact option without applying gate voltage. Figure A.2 shows the electron density and conduction band energy level in the non-gated region given by the density-gradient theory, obtained with the doping density of $6.2\times10^{17}\ \mathrm{cm}^{-3}$. When the electron density is integrated from $50\ \mathrm{nm}$ to $160\ \mathrm{nm}$, 2DES electron sheet density is estimated as $4.5\times10^{11}\ \mathrm{cm}^{-2}$, which is nearly the same as the electron sheet density of the sample used in Ch. 4. In this result, the electron density peak is located at the depth of $64\ \mathrm{nm}$ from the surface. The remarkable resemblance between Fig. 3.1 (b) and Fig. A.2 supports the legitimacy of adopting the density-gradient theory for electrostatic problems.

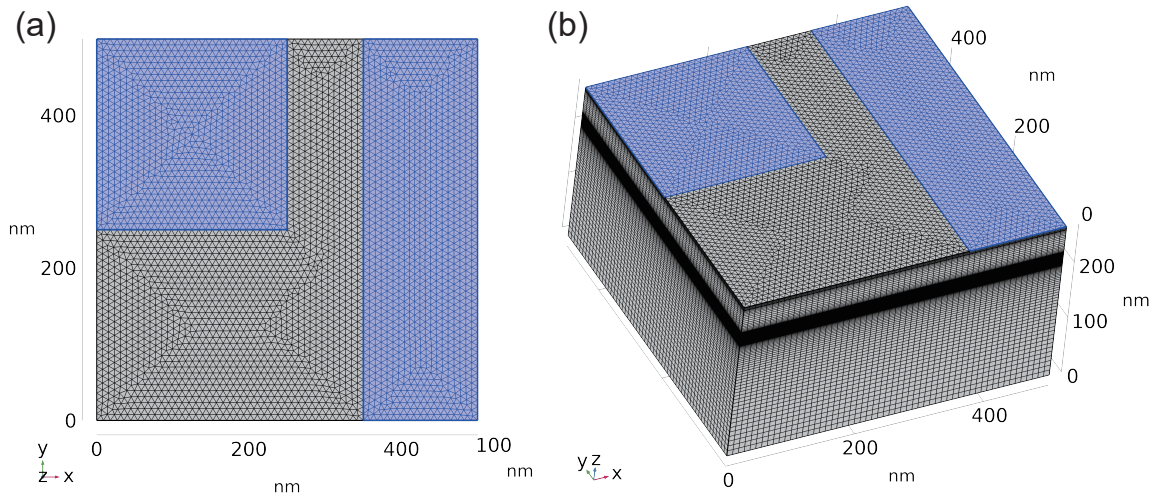

Figure A.1: Finite-element mesh which we used for calculation in Ch. 4. We used the prism shaped elements. The mesh contains 339535 points at which the electrostatic potential is solved. Gate geometry is highlighted as blue. The left is Gate SR and the right is Gate R.

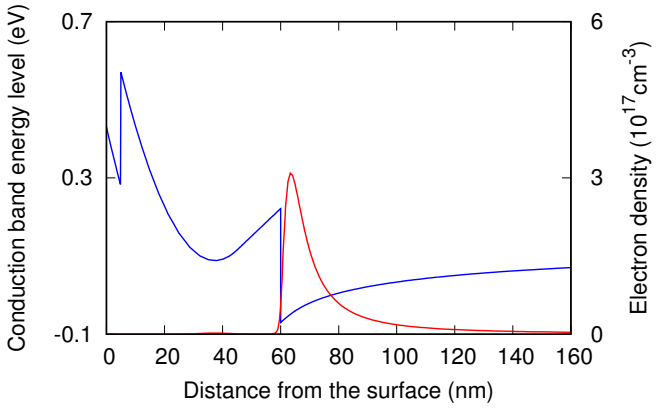

Figure A.2: Electron density (red line) and the energy level of the conduction band (blue line) in the non-gated region given by the density-gradient theory calculated by the commercial software COMSOL Multiphysics.

Appendix B

Quantum Hall effect

B.1 Landau quantization

The Hamiltonian describing the system in which a perpendicular magnetic field is applied to 2DES can be written as follows:

$$\mathscr{H} = \frac{m}{2}\boldsymbol{v}^2 = \frac{(\boldsymbol{p}_c + e\boldsymbol{A})^2}{2m} \equiv \frac{\boldsymbol{\pi}^2}{2m} = \frac{\pi_x^2 + \pi_y^2}{2m}. \tag{B.1}$$

The commutation relations between the components of $\boldsymbol{\pi}$ and the coordinates are

$$[\pi_\alpha, \beta] = -i\hbar\delta_{\alpha\beta}, \ \ (\alpha, \beta = x, y), [\pi_x, \pi_y] = -i\frac{\hbar^2}{l_B^2}, \tag{B.2}$$

and thus x and y components are not commutable. This corresponds to the fact that the orbits are bent by the magnetic field in the classical case, and hence the x and y components are not independent of each other. The magnetic length l_B is given by

$$l_B \equiv \sqrt{\frac{\hbar}{eB}} = \sqrt{\frac{1}{2}}\sqrt{\frac{\phi_0}{\pi B}}. \tag{B.3}$$

This is $1/\sqrt{2}$ of the radius of the circle penetrated by the magnetic flux quantum, and is also called the minimum Landau radius. The coefficient $1/\sqrt{2}$ corresponds to the zero-point energy $\hbar\omega_c/2$. Let us define the guiding center (X, Y) operator $\hat{\boldsymbol{R}}$ and the real space coordinate operator $\hat{\boldsymbol{r}}$ as

$$\hat{\boldsymbol{r}} = \hat{\boldsymbol{R}} + \frac{l_B^2}{\hbar}(\pi_y, -\pi_x). \tag{B.4}$$

From the commutation relation between π_x and π_y, we obtain

$$[X, Y] = il_B^2. \tag{B.5}$$

Since $\mathscr{H}$ in Eq. (B.1) is quadratic and harmonic for $\boldsymbol{\pi}$, by introducing following operators

$$a = \frac{l_B}{\sqrt{2}\hbar}(\pi_x - i\pi_y), \ \ a^\dagger = \frac{l_B}{\sqrt{2}\hbar}(\pi_x + i\pi_y), \tag{B.6}$$

we can rewrite eq. (B.1) as

$$\mathscr{H} = \hbar\omega_c \left(a^\dagger a + \frac{1}{2} \right) \tag{B.7}$$

with $[a, a^\dagger] = 1$. This is the same form as the harmonic oscillator, and results in the discrete energy levels

$$E_n = \hbar\omega_c \left(n + \frac{1}{2} \right) \quad (n = 0, 1, 2, \cdots). \tag{B.8}$$

This can be considered as the discretization of the (angular) momentum and the energy levels due to the quantum confinement by the magnetic field. This type of quantization by the magnetic field is called the Landau quantization.

To find the specific form of the eigenstates belonging to the Landau level, we take the Landau gauge $\boldsymbol{A} = (0, Bx, 0)$. The Schrödinger equation is written as

$$\begin{aligned} \mathscr{H}\psi = \frac{(\boldsymbol{p}_c + e\boldsymbol{A})^2}{2m}\psi &= \frac{-1}{2m}\left[\hbar^2 \frac{\partial^2}{\partial x^2} - \left(-i\hbar\frac{\partial}{\partial y} + eBx \right)^2 \right] \psi(\boldsymbol{r}) \\ &= \frac{1}{2m}\left[-\hbar^2\nabla^2 - 2i\hbar eBx\frac{\partial}{\partial y} + e^2B^2x^2 \right] \psi(\boldsymbol{r}) = E\psi(\boldsymbol{r}). \end{aligned} \tag{B.9}$$

The operator $\hbar\partial/i\partial\boldsymbol{r}$, which is in canonical commutation relation with $\boldsymbol{r}$, corresponds to $\boldsymbol{p}_c$. Since the operator y is not included in the Hamiltonian, the y component becomes a plane wave. Thus, we substitute the form $\psi(\boldsymbol{r}) = u(x)\exp(iky)$ into the above equation and obtain

$$\begin{aligned} \left[-\frac{\hbar^2}{2m}\frac{d^2}{dx^2} + \frac{(eB)^2}{2m}\left(x + \frac{\hbar}{eB}k \right)^2 \right] u(x) &= \left[-\frac{\hbar^2}{2m}\frac{d^2}{dx^2} + \frac{m\omega_c^2}{2}(x + l_B^2 k)^2 \right] u(x) \\ &= Eu(x). \end{aligned} \tag{B.10}$$

This is an equation of one-dimensional harmonic oscillator centered at $x = -l_B^2 k$, yielding the eigenvalue of Eq. (B.8) and the eigenfunction of

$$\psi_{nk}(\boldsymbol{r}) \propto H_n\left(\frac{x - x_k}{l_B} \right) \exp\left(-\frac{(x - x_k)^2}{2l_B^2} \right) \exp(iky) \;\; (x_k \equiv -l_B^2 k), \tag{B.11}$$

where H_n is the nth-order Hermite polynomial and X is fixed as $X = x_k = -l_B^2 k = -l_B^2 p_y/\hbar$. As for y component, it is a plane wave, spreading over the whole space. Thus, the state of Eq. (B.11) has uncertainty in Y. Because the group velocity in the y direction is $v_y = \partial E/\partial k = 0$, Eq. (B.11) is not a traveling wave. As we will see in the following section, when the energy is X dependent, motion in the y direction occurs.

B.2 Edge states

Let us consider a 2DES, which is confined by a potential well $V(x)$ of width W in the x direction, is infinitely long in the y direction. A strong magnetic field is applied in the z direction, and a current flows in the y direction.

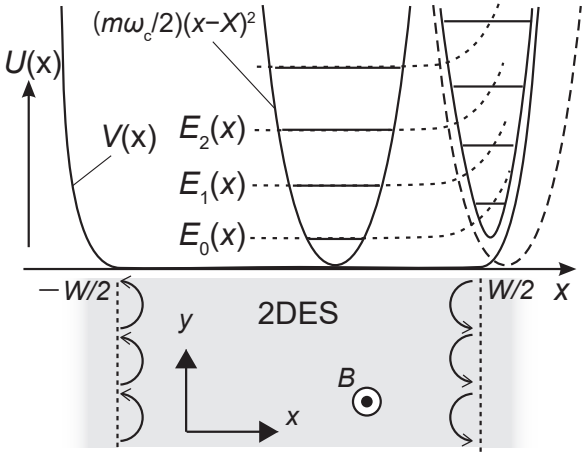

Figure B.1: The potential $U(x)$ of a two-dimensional electron system under a strong magnetic field in the presence of a confining potential $V(x)$. The formation of the edge state is shown by the dashed line. The potential $U(x)$ is a sum of the harmonic-oscillator potential and $V(x)$. Bottom shows a schematic diagram of the classical skipping orbits.

Taking the Landau gauge, the wave equation becomes Eq. (B.9) with the addition of $V(x)$. Figure B.1 shows the potential well with the presence of a magnetic field confinement. Well inside the sample, $V(x) = 0$, and the normal Landau quantization occurs. Near the edge, on the other hand, $V(x)$ make the harmonic-oscillator potential narrower, the effective value of ω larger, and hence the energy eigenvalue increase. As the guiding center X is moved closer to the edge and the distance between the edge and X approaches about the width of the wave function $\sqrt{2n+1}l_B/2$, the nth Landau level begins to rise. At the position where this rise occurs,

$$\langle v_y \rangle = dE/\hbar dk = -(l_B^2/\hbar)dE/dX \tag{B.12}$$

becomes finite and motion along the edge is possible. This corresponds to a skipping trajectory that classically runs along the edge, as shown schematically in the bottom panel of Fig. B.1. Such a state is called an edge state. In the edge state, the direction of electron motion is determined by the direction of the magnetic field.

If the edge state wavefunction is normalized to the length L_y in the y direction, the current carried by this state is $j = (e/L_y)\langle v_y \rangle$. Let us focus on the edge states belonging to a single Landau level that occurs at one of the two 2DES edges. In these edge states, the states up to the electrochemical potential μ are occupied by electrons. Thus, the current carried by the edge states with the energies higher than the reference energy E_0 (higher than the bulk Landau level) is

$$J = \int_{X_0}^{X_\mu} \frac{L_y dX}{2\pi l_B^2} \frac{e}{L_y} \langle v_y \rangle = \frac{e}{h} \int dX \frac{dE}{dX} = \frac{e}{h}(\mu - E_0). \tag{B.13}$$

This shows that there is a universal relationship between the difference of the currents flowing in the opposite directions at both edges of the sample, i.e, the Hall voltage and the net current flowing through the sample, resulting in a quantized Hall resistance of h/e^2 per one edge state.

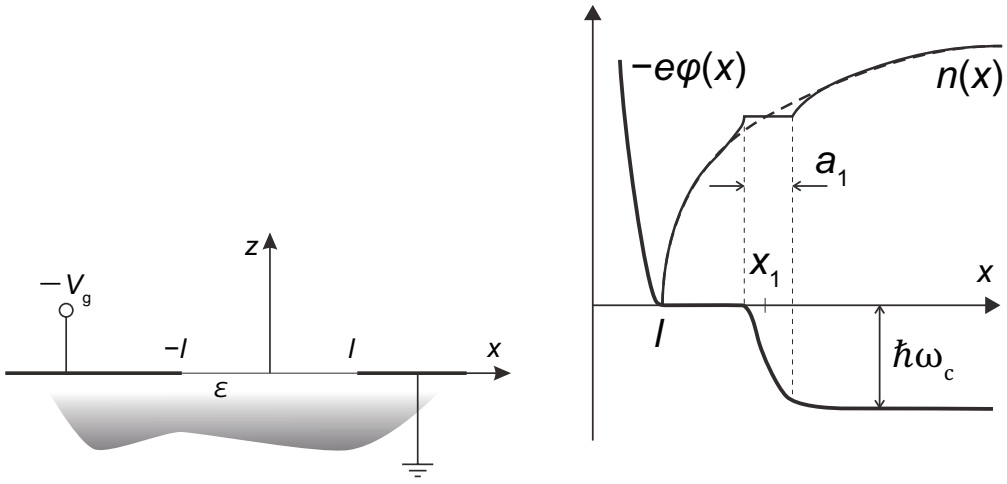

(a) (b)

Figure B.2: (a) Schematic of the simple boundary condition used in the calculation of the electrostatic state at the edge of Chklovskii *et al.* [30]. No magnetic field is applied. (b) The electrostatic potential $\phi(x)$ and the electron density $n(x)$ of the quantum hole edge calculated by adding the dipole field due to the incompressible stripe to the simple model in (a). The dashed line shows $n(x)$ in the absence of the dipole field.

B.3 Electrostatics of edge channels

B.3.1 Electrostatic model of Chklovskii *et al.*

Let us briefly describe the electrostatic model (equivalent to the Hartree approximation) of edge states presented in Ref. [30].

First, we consider the electrostatic potential at the edge without a magnetic field. As shown in Fig. B.2 (a), we suppose that a dielectric with relative permittivity ϵ fills $z < 0$, and a metal gate electrode infinitely long in the y direction is placed in the $x < -l$ region in the xy plane at $z = 0$. The actual gate electrode is located slightly above the 2DES, but its effect will be treated later. In solving the Laplace equation in the $z < 0$ part to obtain the potential, we use the approximation $\epsilon \gg 1$, simplifing the boundary condition as

$$\varphi(x, z = 0) = \begin{cases} -V_{\rm g}, & x < -l\ , \\ 0, & x > l\ , \end{cases} \tag{B.14}$$

$$\left.\frac{d\varphi(x,z)}{dz}\right|_{z\to -0} = \frac{4\pi e n_0}{\epsilon}, \quad |x| < l. \tag{B.15}$$

The solution is

$$\varphi(x, z = 0) = -\frac{V_{\rm g}}{2} + \frac{V_{\rm g}}{\pi}\arcsin(x/l) + \frac{4\pi e n_0}{\epsilon}(l^2 - x^2)^{1/2}, \quad |x| < l. \tag{B.16}$$

Avoiding the anomaly at $x = l$, we obtain

$$l = \frac{V_{\rm g}\epsilon}{4\pi^2 n_0 e}. \tag{B.17}$$

This gives the thickness of the depletion layer. We thereby obtain the two-dimensional electron density

$$n(x) = \left[\frac{x-l}{x+l}\right]^{1/2} n_0, \quad x > l. \tag{B.18}$$

When a magnetic field is applied, the incompressible strip comprising constant $n(x)$ emerges, adding a dipole field in the above condition. Due to the smallness of the parameter $\hbar\omega_{\rm c}/eV_{\rm g}$, we expect that the width of the depletion region given by Eq. (B.18) remains practically unchanged. We write the filling factor and the electron density in the region sufficiently inside the 2DES from the edge by ν_0 and $n_0 = \nu_0/2\pi l_B^2$, respectively, and the filling factor and the electron density at the incompressible strip by ν and $n(x) = \nu/2\pi l_B^2$, respectively. By substituting these into Eq. (B.18), we get

$$x_\nu = l_B \frac{\nu_0^2 + \nu^2}{\nu_0^2 - \nu^2}. \tag{B.19}$$

We obtain the width of this stripe as a_1 as in Fig. B.2(b) by solving the Laplace equation with the following condition

$$\varphi(x, z=0) = \begin{cases} -V_{\rm g}, & x < -l, \\ 0, & l < x < x_1 - a_1/2, \\ \hbar\omega_{\rm c}, & x > x_1 + a_1/2 \end{cases}. \tag{B.20}$$

The electrostatic structure around this incompressible stripe is obtained by replacing $2l$ with a_1 and $eV_{\rm g}$ with $\hbar\omega_c$ in (B.16), and we obtain

$$a_1^2 = \frac{2\epsilon\hbar\omega_{\rm c}}{\pi^2 e^2 dn/dx|_{x=x_1}}. \tag{B.21}$$

It should be noted that, in this approximation, the band returns to a flat state near the edge state due to the screening effect. This means that the group velocity obtained by the band slope due to the edge potential is lost again. The existence of edge conduction indicates that the approximation of a completely flat band is not sufficient. The actual effective mass depends on the edge potential and should be investigated experimentally.

B.3.2 Electrostatic model of Larkin-Davis

In the actual condition, the gate electrode is located above the 2DES, and the surface states of the substrate causes Fermi level pinning and/or the localization of carriers at the surface. Thus, electrostatic properties should be modified from the model of Chklovskii *et al*. To take the above effects into account, Larkin and Davis proposed the setting as shown in Fig. B.3 [57]. In the self-consistent Thomas-Fermi approximation, the density $n(x)$ of the 2DES obeys

$$\frac{\pi\hbar^2}{m} n(x) = \mu + e\Phi(x, d), \tag{B.22}$$

where μ is the Fermi level of the 2DES and $\Phi(x, d)$ is the electrostatic potential in the plane of the 2DES.

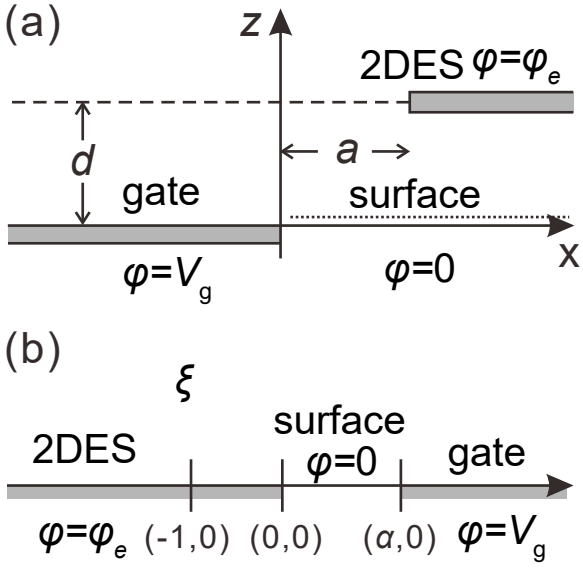

Figure B.3: (a) The setup with the gate electrode placed d above the plane of the 2DES. We have reversed the vertical orientation for convenience. (b) The setup in (a) mapped to ξ space by conformal transformation.

Pinned surface model

Boundary conditions of the pinned surface model are $\Phi = 0$ on the exposed surface, $\Phi = eV_{\rm g}$ on the gate, with $\partial\Phi/\partial z = 0$ in the limit $z \to \infty$. We assume that the charge in the doping layer is uniformly distributed normal to z and does not move during the experiment. Then, with a potential $\varphi_{\rm D}(z)$ caused by the donors, the potential $\varphi = \Phi - \varphi_{\rm D}$ satisfies the Poisson equation in $z > 0$ with the charge density only from the 2DES,

$$\epsilon\epsilon_0\nabla^2\varphi = en(x)\delta(z-d). \tag{B.23}$$

Integrating Eq. (B.23), we find the potential $\varphi_{\rm e}$ of the 2DES far from the gates ($x \gg a$) to be $\varphi_{\rm e} = -en_0 d/\epsilon\epsilon_0$. The Fermi energy is much smaller than the potential of the 2DES, so that we may disregard the Thomas-Fermi correction and set $\varphi = \varphi_{\rm e}$ in the 2DES. This in turn allows us to replace the Poisson equation (B.23) for the potential φ with the Laplace equation and the additional boundary conditions $\varphi(x > a, z = d) = \varphi_e$ on the 2DES.

We solve the electrostatic problem by conformal mapping. The function $w = \xi + \ln\xi$ transforms the upper half-plane in ξ to the upper half-plane in w with the cut $(-\infty + i\pi, -1 + i\pi)$. Thus $w = \pi(iz + a - x)/d - 1$ gives the mapping to ξ illustrated in Fig. B.3, where the geometry is simple. The edge of the gate ($x = 0,\ z = 0$) maps to $\xi = \alpha$, where

$$\alpha + \ln\alpha + 1 = \frac{\pi a}{d}. \tag{B.24}$$

Then, we get the potential for all ξ as

$$\varphi = \frac{1}{\pi}{\rm Im}[V_{\rm g}\ln(\alpha - \xi) + \varphi_{\rm e}\ln\xi]. \tag{B.25}$$

This potential generally gives an infinite charge density at the edge of 2DES, whereas a physically acceptable solution must have $n(x) = 0$ at the edge of the 2DES. Thus, we enforce $d\varphi/d\xi = 0$ at $\xi = -1$ to suppress the electric field. This in turn fixes α, and we

find

$$\alpha_{\rm p} = \frac{V_{\rm g}}{\varphi_{\rm e}} - 1. \tag{B.26}$$

Combined with Eq. (B.24), this gives the dependence of the depletion length a on the gate voltage.

The electron density $n(x)$ is given by Gauss theorem as

$$\frac{n(x)}{n_0} = \frac{\alpha_{\rm p}}{\alpha_{\rm p} + \xi_1} - \frac{\alpha_{\rm p}}{\alpha_{\rm p} + \xi_2}, \tag{B.27}$$

where $\xi_1 < \xi_2$ are roots of $\xi - 1 - \ln\xi = \pi(x-a)/d$. This is plotted in Fig. B.4.

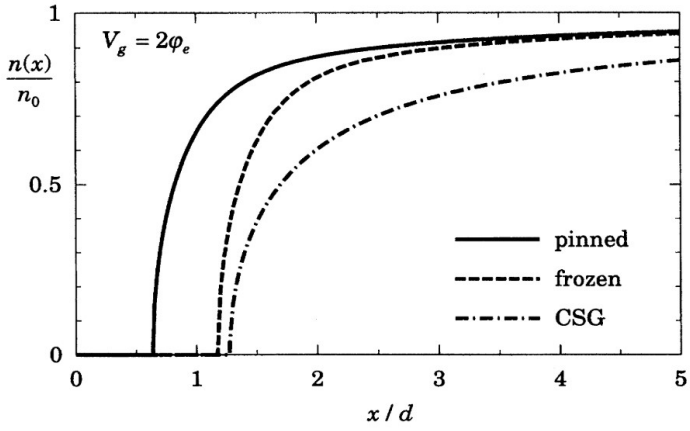

Figure B.4: $n(x)$ at $V_{\rm g} = 2\varphi_{\rm e}$ obtained by the pinned surface, frozen surface, and Chklovskii model (extracted from Ref. [57]).

Frozen surface model

Next, we consider the condition in which the surface charge does not move. This changes the boundary condition to $\partial\varphi/\partial z = \varphi_e/d$ on the exposed surface. The method of solving the problem is the same, and the potential is

$$\varphi = V_{\rm g} + \frac{1}{\pi}{\rm Im}\left\{\varphi_e\{\xi + \ln\xi - [\xi(\xi-\alpha)]^{1/2}\} - V_{\rm g}\ln\left[\frac{\xi}{\alpha} - \left(\frac{\xi^2}{\alpha^2} - \frac{\xi}{\alpha}\right)^{1/2} - \frac{1}{2}\right]\right\}. \tag{B.28}$$

As in the pinned surface, the edge of the 2DES $\alpha_{\rm f}$ is

$$\alpha_{\rm f} = 2\left(\frac{V_{\rm g}}{\varphi_{\rm e}} - 1\right). \tag{B.29}$$

With Eq. (B.24), we obtain a for the frozen surface model. The electron density $n(x)$ is obtained as

$$\frac{n(x)}{n_0} = \left(\frac{\xi_2}{\alpha_f + \xi_2}\right)^{1/2} - \left(\frac{\xi_1}{\alpha_{\rm f} + \xi_1}\right)^{1/2}. \tag{B.30}$$

This is also plotted in Fig. B.4.

Acknowledgments

I want to express my gratitude to many people who have supported me and cooperated with me in conducting this research and writing this thesis.

Firstly, I would like to express my gratitude to all the members of Katsumoto Laboratory. I want to express my best gratitude to Prof. Shingo Katsumoto for providing me with interesting subjects and an excellent research environment and for his guidance and advice in all aspects, from sample preparation to writing the paper. I want to thank Dr. Taketomo Nakamura for his support in sample fabrications, measurements, data analysis, presentation, and writings. I want to thank Dr. Akira Endo for his support in preparing and handling the experimental instruments, data analysis, and writings. I want to thank Mr. Yoshiaki Hashimoto for his assistance in handling experimental instruments and sample fabrications. I want to thank Mr. Makoto Onizaki for his assistance in handling experimental instruments and sample fabrications. I want to thank Ms. Junko Nagayama for her cooperation in various aspects of my research life, such as application for conferences.

Secondly, I would like to express my gratitude to all the Quantum Solid State Physics Research Group members, NTT Basic Research Laboratories. I would like to express my sincere gratitude to Dr. Masayuki Hashisaka for giving me the opportunity to study shot-noise measurements and for supporting me with measurements, data analysis, presentation, and writing.

Finally, I would like to dedicate this thesis to my family to express the deepest gratitude for their support and encouragement throughout my long student life.

Bibliography

[1] Ryszard Horodecki, Paweł Horodecki, Michał Horodecki, and Karol Horodecki. Quantum entanglement. *Rev. Mod. Phys.*, 81:865–942, Jun 2009.

[2] David P. DiVincenzo. Quantum Computation. *Science*, 270(5234):255–261, 1995.

[3] T. D. Ladd, F. Jelezko, R. Laflamme, Y. Nakamura, C. Monroe, and J. L. O'Brien. Quantum computers. *Nature*, 464(7285):45–53, Mar 2010.

[4] U. Fano. Pairs of two-level systems. *Rev. Mod. Phys.*, 55:855–874, Oct 1983.

[5] M. Veldhorst, C. H. Yang, J. C. C. Hwang, W. Huang, J. P. Dehollain, J. T. Muhonen, S. Simmons, A. Laucht, F. E. Hudson, K. M. Itoh, A. Morello, and A. S. Dzurak. A two-qubit logic gate in silicon. *Nature*, 526(7573):410–414, Oct 2015.

[6] Walther Gerlach and Otto Stern. Der experimentelle Nachweis der Richtungsquantelung im Magnetfeld. *Zeitschrift für Physik*, 9(1):349–352, Dec 1922.

[7] Walther Gerlach and Otto Stern. Das magnetische Moment des Silberatoms. *Zeitschrift für Physik*, 9(1):353–355, Dec 1922.

[8] W. Gerlach and O. Stern. Der experimentelle Nachweis des magnetischen Moments des Silberatoms. *Zeitschrift für Physik*, 8(1):110–111, Dec 1922.

[9] Eugene P. Wigner. The Problem of Measurement. *American Journal of Physics*, 31(1):6–15, 1963.

[10] Marlan O. Scully, Berthold-Georg Englert, and Julian Schwinger. Spin coherence and Humpty-Dumpty. III. The effects of observation. *Phys. Rev. A*, 40:1775–1784, Aug 1989.

[11] G B Roston, M Casas, A Plastino, and A R Plastino. Quantum entanglement, spin-1/2 and the Stern–Gerlach experiment. *European Journal of Physics*, 26(4):657–672, may 2005.

[12] P. Simon and D. Feinberg. Electronic spin precession and interferometry from spin-orbital entanglement in a double quantum dot. *Phys. Rev. Lett.*, 97:247207, Dec 2006.

[13] J. Summhammer, G. Badurek, H. Rauch, U. Kischko, and A. Zeilinger. Direct observation of fermion spin superposition by neutron interferometry. *Phys. Rev. A*, 27:2523–2532, May 1983.

[14] Tobias Denkmayr, Hermann Geppert, Stephan Sponar, Hartmut Lemmel, Alexandre Matzkin, Jeff Tollaksen, and Yuji Hasegawa. Observation of a quantum Cheshire Cat in a matter-wave interferometer experiment. *Nature Communications*, 5(1):4492, Jul 2014.

[15] Akio Hosoya. *Basics of quantum computers : lectures on quantum computation*. Number SGC Library; 69 in Suricagaku. Science corporation, 2nd edition edition, 2009.

[16] Masahiro Hotta. *Quantum Mechanics: A Modern Introduction*. Kodansha scientific, 2021.

[17] Alexia Auffeves, Dario Gerace, Maxime Richard, Stefano Portolan, and Marcelo Franca Santos, editors. *Strong Light-Matter Coupling: From Atoms to Solid-State Systems*. World Scientific Pub Co Inc, 2 2014.

[18] H. Duprez, E. Sivre, A. Anthore, A. Aassime, A. Cavanna, A. Ouerghi, U. Gennser, and F. Pierre. Macroscopic electron quantum coherence in a solid-state circuit. *Phys. Rev. X*, 9:021030, May 2019.

[19] Preden Roulleau, F. Portier, D. C. Glattli, P. Roche, A. Cavanna, G. Faini, U. Gennser, and D. Mailly. Finite bias visibility of the electronic Mach-Zehnder interferometer. *Phys. Rev. B*, 76:161309, Oct 2007.

[20] Preden Roulleau, F. Portier, P. Roche, A. Cavanna, G. Faini, U. Gennser, and D. Mailly. Direct Measurement of the Coherence Length of Edge States in the Integer Quantum Hall Regime. *Phys. Rev. Lett.*, 100:126802, Mar 2008.

[21] P. Roulleau, F. Portier, P. Roche, A. Cavanna, G. Faini, U. Gennser, and D. Mailly. Noise Dephasing in Edge States of the Integer Quantum Hall Regime. *Phys. Rev. Lett.*, 101:186803, Oct 2008.

[22] P. Roulleau, F. Portier, P. Roche, A. Cavanna, G. Faini, U. Gennser, and D. Mailly. Tuning Decoherence with a Voltage Probe. *Phys. Rev. Lett.*, 102:236802, Jun 2009.

[23] David C. Dixon, Keith R. Wald, Paul L. McEuen, and M. R. Melloch. Dynamic nuclear polarization at the edge of a two-dimensional electron gas. *Phys. Rev. B*, 56:4743–4750, Aug 1997.

[24] T. Nakajima, Y. Kobayashi, S. Komiyama, M. Tsuboi, and T. Machida. Scanning microscopy of nuclear spin polarization via quantum Hall edge channels. *Phys. Rev. B*, 81:085322, Feb 2010.

[25] A. Würtz, R. Wildfeuer, A. Lorke, E. V. Deviatov, and V. T. Dolgopolov. Separately contacted edge states: A spectroscopic tool for the investigation of the quantum Hall effect. *Phys. Rev. B*, 65:075303, Jan 2002.

[26] Kensuke Kobayashi and Masayuki Hashisaka. Shot Noise in Mesoscopic Systems: From Single Particles to Quantum Liquids. *Journal of the Physical Society of Japan*, 90(10):102001, 2021.

[27] K. v. Klitzing, G. Dorda, and M. Pepper. New Method for High-Accuracy Determination of the Fine-Structure Constant Based on Quantized Hall Resistance. *Phys. Rev. Lett.*, 45:494–497, Aug 1980.

[28] R. Landauer. Spatial variation of currents and fields due to localized scatterers in metallic conduction. *IBM Journal of Research and Development*, 1(3):223–231, July 1957.

[29] M. Büttiker. Four-Terminal Phase-Coherent Conductance. *Phys. Rev. Lett.*, 57:1761–1764, Oct 1986.

[30] D. B. Chklovskii, B. I. Shklovskii, and L. I. Glazman. Electrostatics of edge channels. *Phys. Rev. B*, 46:4026–4034, Aug 1992.

[31] Yang Ji, Yunchul Chung, D. Sprinzak, M. Heiblum, D. Mahalu, and Hadas Shtrikman. An electronic Mach-Zehnder interferometer. *Nature*, 422(6930):415–418, Mar 2003.

[32] T. Machida, H. Hirai, S. Komiyama, and Y. Shiraki. Phase coherence of edge states over macroscopic length scales. *Physica B: Condensed Matter*, 249-251:128–131, June 1998.

[33] Z F Ezawa and G Tsitsishvili. Quantum Hall ferromagnets. *Reports on Progress in Physics*, 72(8):086502, July 2009.

[34] Tsuneya Ando and Yasutada Uemura. Theory of Oscillatory g Factor in an MOS Inversion Layer Under Strong Magnetic Fields. *J. Phys. Soc. Japan*, 37(4):1044–1052, 1974.

[35] R. J. Nicholas, R. J. Haug, K. v. Klitzing, and G. Weimann. Exchange enhancement of the spin splitting in a GaAs-$\mathrm{Ga_xAl_{1-x}As}$ heterojunction. *Phys. Rev. B*, 37:1294–1302, Jan 1988.

[36] G. Müller, D. Weiss, A. V. Khaetskii, K. von Klitzing, S. Koch, H. Nickel, W. Schlapp, and R. Lösch. Equilibration length of electrons in spin-polarized edge channels. *Phys. Rev. B*, 45:3932–3935, Feb 1992.

[37] A. V. Khaetskii. Transitions between spin-split edge channels in the quantum-Hall-effect regime. *Phys. Rev. B*, 45:13777–13780, Jun 1992.

[38] D. G. Polyakov. Spin-flip scattering in the quantum Hall regime. *Phys. Rev. B*, 53:15777–15788, Jun 1996.

[39] R. Winkler. *Spin-orbit Coupling Effects in Two-Dimensional Electron and Hole Systems*. Springer, 2003.

[40] M. Kataoka, N. Johnson, C. Emary, P. See, J. P. Griffiths, G. A. C. Jones, I. Farrer, D. A. Ritchie, M. Pepper, and T. J. B. M. Janssen. Time-of-Flight Measurements of Single-Electron Wave Packets in Quantum Hall Edge States. *Phys. Rev. Lett.*, 116:126803, Mar 2016.

[41] T Nakajima, Kuan-Ting Lin, and S Komiyama. Gate-Control of Spin Precession in Quantum Hall Edge States. *arXiv preprint arXiv:1207.7243*, 2012.

[42] Takashi Nakajima, Kuan Ting Lin, and Susumu Komiyama. Electrical control of flying spin precession in chiral 1D edge states. *AIP Conf. Proc.*, 1566:301–302, 2013.

[43] Michihisa Yamamoto, Shintaro Takada, Christopher Bäuerle, Kenta Watanabe, Andreas D. Wieck, and Seigo Tarucha. Electrical control of a solid-state flying qubit. *Nature Nanotechnology*, 7(4):247–251, March 2012.

[44] Ya.M. Blanter and M. Buttiker. Shot noise in mesoscopic conductors. *Physics Reports*, 336(1):1–166, 2000.

[45] Takeo Kato. *Bussei Kenkyu*, 3(1):031201, 2014.

[46] W. Schottky. Uber spontane Stromschwankungen in verschiedenen Elektrizitatsleitern. *Annalen der Physik*, 362(23):541–567, 1918.

[47] Christophe Texier and Markus Büttiker. Effect of incoherent scattering on shot noise correlations in the quantum Hall regime. *Phys. Rev. B*, 62:7454–7458, Sep 2000.

[48] S. Oberholzer, E. Bieri, C. Schönenberger, M. Giovannini, and J. Faist. Positive Cross Correlations in a Normal-Conducting Fermionic Beam Splitter. *Phys. Rev. Lett.*, 96:046804, Feb 2006.

[49] L. DiCarlo, Y. Zhang, D. T. McClure, C. M. Marcus, L. N. Pfeiffer, and K. W. West. System for measuring auto- and cross correlation of current noise at low temperatures. *Review of Scientific Instruments*, 77(7):073906, 2006.

[50] S. Komiyama, H. Hirai, S. Sasa, and S. Hiyamizu. Violation of the integral quantum Hall effect: Influence of backscattering and the role of voltage contacts. *Phys. Rev. B*, 40:12566–12569, Dec 1989.

[51] B. J. van Wees, E. M. M. Willems, C. J. P. M. Harmans, C. W. J. Beenakker, H. van Houten, J. G. Williamson, C. T. Foxon, and J. J. Harris. Anomalous integer quantum Hall effect in the ballistic regime with quantum point contacts. *Phys. Rev. Lett.*, 62:1181–1184, Mar 1989.

[52] M. Hashisaka, N. Hiyama, T. Akiho, K. Muraki, and T. Fujisawa. Waveform measurement of charge- and spin-density wavepackets in a chiral Tomonaga-Luttinger liquid. *Nature Physics*, 13(6):559–562, Jun 2017.

[53] Masayuki Hashisaka and Toshimasa Fujisawa. Tomonaga–Luttinger-liquid nature of edge excitations in integer quantum Hall edge channels. *Reviews in Physics*, 3:32–43, November 2018.

[54] Daijiro Yoshioka. *The Quantum Hall Effect*, volume 133 of *Springer Series in Solid-State Sciences*. Springer-Verlag Berlin Heidelberg, 2002.

[55] A. Aharony, O. Entin-Wohlman, B. I. Halperin, and Y. Imry. Phase measurement in the mesoscopic Aharonov-Bohm interferometer. *Phys. Rev. B*, 66:115311, Sep 2002.

[56] Ireneusz Strzalkowski, Sharad Joshi, and C. R. Crowell. Dielectric constant and its temperature dependence for GaAs, CdTe, and ZnSe. *Applied Physics Letters*, 28(6):350–352, 1976.

[57] Ivan A. Larkin and John H. Davies. Edge of the two-dimensional electron gas in a gated heterostructure. *Phys. Rev. B*, 52:R5535–R5538, Aug 1995.

[58] K. Oto, S. Takaoka, and K. Murase. Width of compressible strips in quantum Hall regime. *Physica B: Condensed Matter*, 298(1-4):18–23, April 2001.

[59] S. Masubuchi, K. Hamaya, and T. Machida. Gate-controlled nuclear magnetic resonance in an AlGaAs/GaAs quantum Hall device. *Applied Physics Letters*, 89(20):202111, November 2006.

[60] H. Kamata, T. Ota, K. Muraki, and T. Fujisawa. Voltage-controlled group velocity of edge magnetoplasmon in the quantum Hall regime. *Phys. Rev. B*, 81:085329, Feb 2010.

[61] S. Komiyama, H. Hirai, M. Ohsawa, Y. Matsuda, S. Sasa, and T. Fujii. Inter-edge-state scattering and nonlinear effects in a two-dimensional electron gas at high magnetic fields. *Phys. Rev. B*, 45:11085–11107, May 1992.

[62] K. Y. Chen, C. S. Chu, and A. G. Mal'shukov. Resonant spin dipole induced by an in-plane potential gradient spin-orbit interaction. *Phys. Rev. B*, 76:153304, Oct 2007.

[63] Jan R. Rubbmark, Michael M. Kash, Michael G. Littman, and Daniel Kleppner. Dynamical effects at avoided level crossings: A study of the Landau-Zener effect using Rydberg atoms. *Phys. Rev. A*, 23:3107–3117, Jun 1981.

[64] COMSOL, inc. https://www.comsol.com.

[65] I. Neder, N. Ofek, Y. Chung, M. Heiblum, D. Mahalu, and V. Umansky. Interference between two indistinguishable electrons from independent sources. *Nature*, 448(7151):333–337, Jul 2007.

[66] E. Bocquillon, V. Freulon, J.-M Berroir, P. Degiovanni, B. Plaçais, A. Cavanna, Y. Jin, and G. Fève. Coherence and Indistinguishability of Single Electrons Emitted by Independent Sources. *Science*, 339(6123):1054–1057, 2013.

[67] J. Dubois, T. Jullien, F. Portier, P. Roche, A. Cavanna, Y. Jin, W. Wegscheider, P. Roulleau, and D. C. Glattli. Minimal-excitation states for electron quantum optics using levitons. *Nature*, 502(7473):659–663, Oct 2013.

[68] H. Bartolomei, M. Kumar, R. Bisognin, A. Marguerite, J.-M. Berroir, E. Bocquillon, B. Plaçais, A. Cavanna, Q. Dong, U. Gennser, Y. Jin, and G. Fève. Fractional statistics in anyon collisions. *Science*, 368(6487):173–177, 2020.

[69] Masayuki Hashisaka, Yoshiaki Yamauchi, Kensaku Chida, Shuji Nakamura, Kensuke Kobayashi, and Teruo Ono. Noise measurement system at electron temperature down to 20 mk with combinations of the low pass filters. *Review of Scientific Instruments*, 80(9):096105, 2009.

[70] Tomonori Arakawa, Yoshitaka Nishihara, Masahiro Maeda, Shota Norimoto, and Kensuke Kobayashi. Cryogenic amplifier for shot noise measurement at 20 mk. *Applied Physics Letters*, 103(17):172104, 2013.

[71] Sanghyun Lee, Masayuki Hashisaka, Takafumi Akiho, Kensuke Kobayashi, and Koji Muraki. Cryogenic GaAs high-electron-mobility-transistor amplifier for current noise measurements. *Review of Scientific Instruments*, 92(2):023910, 2021.

[72] Masayuki Hashisaka, Tomoaki Ota, Koji Muraki, and Toshimasa Fujisawa. Shot-Noise Evidence of Fractional Quasiparticle Creation in a Local Fractional Quantum Hall State. *Phys. Rev. Lett.*, 114:056802, Feb 2015.

[73] T Ota, M Hashisaka, K Muraki, and T Fujisawa. Negative and positive cross-correlations of current noises in quantum Hall edge channels at bulk filling factor $\nu = 1$. *Journal of Physics: Condensed Matter*, 29(22):225302, apr 2017.

[74] T. Martin. "Noise in mesoscopic physics" in *Nanophysics: Coherence and Transport*, edited by H. Bouchiat, Y. Gefen, S. Guéron, G. Montambaux, and J. Dalibard. ISSN. Elsevier, 2005.

[75] Masayuki Hashisaka, Tomoaki Ota, Masakazu Yamagishi, Toshimasa Fujisawa, and Koji Muraki. Cross-correlation measurement of quantum shot noise using homemade transimpedance amplifiers. *Review of Scientific Instruments*, 85(5):054704, 2014.

[76] Huang-Ming Lee, Koji Muraki, Edward Yi Chang, and Yoshiro Hirayama. Electronic transport characteristics in a one-dimensional constriction defined by a triple-gate structure. *Journal of Applied Physics*, 100(4):043701, 2006.

[77] Erwann Bocquillon, Vincent Freulon, Francois D. Parmentier, Jean-Marc Berroir, Bernard Placais, Claire Wahl, Jerome Rech, Thibaut Jonckheere, Thierry Martin, Charles Grenier, Dario Ferraro, Pascal Degiovanni, and Gwendal Feve. Electron quantum optics in ballistic chiral conductors. *Annalen der Physik*, 526(1-2):1–30, 2014.

[78] Christopher Bäuerle, D Christian Glattli, Tristan Meunier, Fabien Portier, Patrice Roche, Preden Roulleau, Shintaro Takada, and Xavier Waintal. Coherent control of single electrons: a review of current progress. *Reports on Progress in Physics*, 81(5):056503, apr 2018.

[79] Vittorio Giovannetti, Fabio Taddei, Diego Frustaglia, and Rosario Fazio. Multichannel architecture for electronic quantum Hall interferometry. *Phys. Rev. B*, 77:155320, Apr 2008.

[80] E. V. Deviatov, A. Ganczarczyk, A. Lorke, G. Biasiol, and L. Sorba. Quantum Hall Mach-Zehnder interferometer far beyond equilibrium. *Phys. Rev. B*, 84:235313, Dec 2011.

[81] Biswajit Karmakar, Davide Venturelli, Luca Chirolli, Vittorio Giovannetti, Rosario Fazio, Stefano Roddaro, Loren N. Pfeiffer, Ken W. West, Fabio Taddei, and Vittorio Pellegrini. Nanoscale Mach-Zehnder interferometer with spin-resolved quantum Hall edge states. *Phys. Rev. B*, 92:195303, Nov 2015.

[82] P. Samuelsson, E. V. Sukhorukov, and M. Büttiker. Two-Particle Aharonov-Bohm Effect and Entanglement in the Electronic Hanbury Brown–Twiss Setup. *Phys. Rev. Lett.*, 92:026805, Jan 2004.

[83] J. S. Bell. On the Einstein Podolsky Rosen paradox. *Physics Physique Fizika*, 1:195–200, Nov 1964.

[84] Alain Aspect, Jean Dalibard, and Gérard Roger. Experimental Test of Bell's Inequalities Using Time-Varying Analyzers. *Phys. Rev. Lett.*, 49:1804–1807, Dec 1982.

[85] Radu Ionicioiu, Gehan Amaratunga, and Florin Udrea. QUANTUM COMPUTATION WITH BALLISTIC ELECTRONS. *International Journal of Modern Physics B*, 15(02):125–133, 2001.

[86] G. Fève, A. Mahé, J.-M. Berroir, T. Kontos, B. Plaçais, D. C. Glattli, A. Cavanna, B. Etienne, and Y. Jin. An On-Demand Coherent Single-Electron Source. *Science*, 316(5828):1169–1172, 2007.

[87] S. P. Giblin, M. Kataoka, J. D. Fletcher, P. See, T. J. B. M. Janssen, J. P. Griffiths, G. A. C. Jones, I. Farrer, and D. A. Ritchie. Towards a quantum representation of the ampere using single electron pumps. *Nature Communications*, 3(1):930, Jul 2012.

[88] Niels Ubbelohde, Frank Hohls, Vyacheslavs Kashcheyevs, Timo Wagner, Lukas Fricke, Bernd Kaestner, Klaus Pierz, Hans W. Schumacher, and Rolf J. Haug. Partitioning of on-demand electron pairs. *Nature Nanotechnology*, 10(1):46–49, Jan 2015.

[89] Romain Thalineau, Andreas D Wieck, Christopher Bäuerle, and Tristan Meunier. Using a two-electron spin qubit to detect electrons flying above the Fermi sea. *arXiv preprint arXiv:1403.7770*, 2014.

[90] Laura Bellentani, Gaia Forghieri, Paolo Bordone, and Andrea Bertoni. Two-electron selective coupling in an edge-state based conditional phase shifter. *Phys. Rev. B*, 102:035417, Jul 2020.

[91] M. G. Ancona and H. F. Tiersten. Macroscopic physics of the silicon inversion layer. *Phys. Rev. B*, 35:7959–7965, May 1987.

[92] M. G. Ancona. Density-gradient theory: a macroscopic approach to quantum confinement and tunneling in semiconductor devices. *Journal of Computational Electronics*, 10(1):65–97, Jun 2011.